ABSTRACT

VAN VICKLE, PATRICK STEPHEN. Photonic Band Gap Fibers for Transverse Strain Sensing. (Under the direction of Dr. Kara J. Peters.)

This research examines the change in bandgap characteristics of Photonic Bandgap (PBG) fibers under transverse loading for applications such as fabrication and service life monitoring of composite structures. Photonic Bandgap (PBG) fibers rely on Bragg reflection conditions in the plane of optical fiber cross-section and therefore offer great potential as transverse strain sensors which are insensitive to axial loading and temperature variations.

A numerical study of the effect on the bandgap in PBG fibers under transverse loads is thus performed in this dissertation. First the fundamental equations for lightwave propagation in classical step-index fibers, microstrucured holey-fibers and PBG fibers are reviewed. The behavior of each for sensing purposes is also discussed. The structural deformation and electromagnetics modeling of a PBG fiber is then performed using the Finite Element Method (FEM) because this method offers the ability to examine arbitrary fiber configurations, specifically through deformation where the fiber is no longer circularly symmetric.

The FEM models were run for both uniaxial crush loads and uniform pressure loads for both silica and a doped PMMA material targeting strains up to approximately 6% at the boundary of the fiber. The results showed that degradation of the bandgap occurs with loading and that axis specific loading information may be obtained in fibers whose material normal and shear Pockel's constants differ by approximately 50% or more, although the exact difference required is not known. In the case of the PMMA uniform pressure load it was determined that the combination of loading and fiber characteristics may cause the bandgap to switch modes which may interfere with actual sensor implementation and should be avoided. The cross-section of the fiber studied was not rotationally symmetric which resulted in non-symmetric optical output from the uniform pressure case. While fibers of this construction

are likely to not be rotationally symmetric by design, the actual manufacture of the fibers results in a cross section that more closely approximates this condition.

Photonic Bandgap Fibers For Transverse Strain Sensing

by

Patrick Stephen Van Vickle

A dissertation submitted to the Graduate Faculty of
North Carolina State University
In partial fulfillment of the
Requirements for the Degree of
Doctor of Philosophy

Mechanical Engineering

Raleigh, North Carolina

2008

APPROVED BY:

Dr. Jeffery Eischen	Dr. Larry Silverberg
Dr. Kara Peters Chair of Advisory Committee	Dr. Tasnim Hassan

DEDICATION

Dedicated to my loving wife Sarah, and my wonderful children Sophia and Liam

I am thankful for every minute we are together. You are my first thought each morning and my last each night.

BIOGRAPHY

Patrick Van Vickle was born in Rapid City, South Dakota. At the age of two Patrick's United States Air Force family moved several times before settling in Sedalia, Missouri.

At the age of seventeen Patrick moved to North Carolina, where in 1996 he received his Bachelors of Science in Mechanical Engineering from North Carolina State University. In 1999, Patrick received a Masters of Science in Mechanical Engineering from North Carolina State University with a thesis titled "A Spherical Photometer," which developed a neural network based solar sensing array. In 1998 he began work as a Product Design Engineer for Sumitomo Electric Lightwave , an International Telecommunications Company located in Research Triangle Park North Carolina.

He returned to NC State in 2004 and under the direction of Dr. Kara Peters pursued a Doctorate of Philosophy in Mechanical Engineering.

ACKNOWLEDGEMENTS

First and foremost I would like to thank my wife Sarah. As I continue to work through my life's list she continues to support me in all I do and reminds me of all that is important. I can never thank her enough for the wonderful gift of our two amazing children who bring me a level of joy that I cannot describe. They are truly the greatest gift I could or will ever receive, I am so thankful to be a part of their lives.

Next, I would like to thank Dr. Kara Peters, the chairperson of my committee. She has supported my desire to undertake this research while I continued to work to support my family. Her understanding and patience were greatly appreciated. I would also like to thank the members of her research group who were very supportive throughout the completion of this research, Sharon Kiesel, Mohan Prabhugoud,, Guoliang Jiang, and Aliesha Anders. I would also like to thank Lance Mangnum for his assistance with the implementation of the software to make this research possible. In addition to Dr. Peters I would like to thank the committee members, Dr. Larry Silverberg, Dr. Jeffery Eischen, and Dr. Tasnim Hassan for their assistance.

The understanding and patience of Dr. Peters was equaled by my supervisor Steve Stokes, Director of Product Design Engineering at Sumitomo Electric Lightwave. His support and that of my coworkers was key to completing this research.

Finally, I would like to thank my father, William Stephen Van Vickle. He instilled in me a wonder of the physical world and a philosophical questioning nature. These traits are the driving force behind always trying to understand new things and pushing the limits of what I can accomplish.

TABLE OF CONTENTS

LIST OF TABLES

LIST OF FIGURES

CHAPTER I

Introduction

1.1 Motivation

Laminated, fiber-reinforced composites are typically constructed from pre-impregnated layers of reinforcement and resin. For most resin choices the layers are subjected to high temperatures and pressures to cure the laminate. For large structural components this temperature and pressure can vary significantly throughout the laminate during cure. Therefore, it is important to inspect the quality of fabrication. As the materials of construction are typically not transparent for visual inspection, embedded sensors must be placed in the component during cure. The best location for sensor placement is between the layers of laminate. Also, these sensors can give not only give information about the fabrication process, but also detect delamination and damage throughout the service life of the structure.

Typical parameters to be measured include the temperature and pressure distribution in the laminate during the cure cycle, followed by any residual stresses in individual lamina once the component has cured and cooled. The residual transverse strain between layers may be significant and affect the sensor readings (Tao, et. al., 2000, Okabe, et al., 2000). The change or sudden absence of this transverse strain can also be a good indicator of delamination leading to premature failure of the component. To detect these parameters a number of strain sensors have been recently developed.

One type of sensor system, the Smart Layer™, consist of optical and electrical gauges mounted on a thin polyimide film which can be embedded easily between laminae (Lin and Chang, 2002). However, this sensor network can only measure the components of strain in the plane of the film. Photoelastic films can measure pressure applied between layers, but the laminates would need to be transparent, which typically is not the case (Liggins, et al., 2002). Fiber optic Bragg grating (FBG) sensors provide a solution that can measure both in

plane and out of plane components of strain and can measure temperature as well. The multiple strain components are typically separated through birefringence in the optical fiber, which is created by the out of plane loading on the fiber (Tao, et al., 2000; Okabe, et al., 2000; Chehura, et al., 2005; Legge, et al., 2006). The axial Bragg grating has also been specifically adapted to separate the transverse strain component from the in-plane components (Lawrence et. al, 1999). Figure 1-1 shows one example from the literature in which FBG sensors were embedded between layers of a cross-ply laminate to detect the presence of transverse cracking in the layer weakest in the direction of the applied loading.

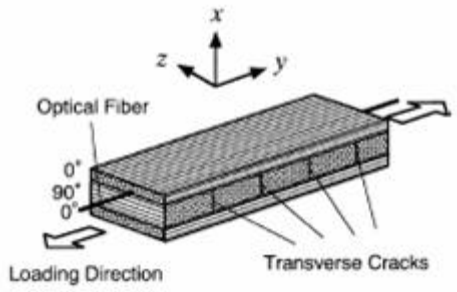

Figure 1-1: Optical Fiber Embedded in Composite Structure (Okabe, et al., 2000)

A fiber optic Bragg grating consists of a traditional step index single mode fiber which has a periodic modulation in index of refraction over a short length of the core (see Figure 1-2). The period of this modulation is written such that the phase matching condition matches a desired optical wavelength. Lightwaves at this wavelength are reflected back while lightwaves at other wavelengths are transmitted forward. When the fiber is strained in the axial direction, the period of the modulation changes, changing the reflected wavelength. By monitoring this change in reflected wavelength an accurate measurement of the axial strain can be obtained.

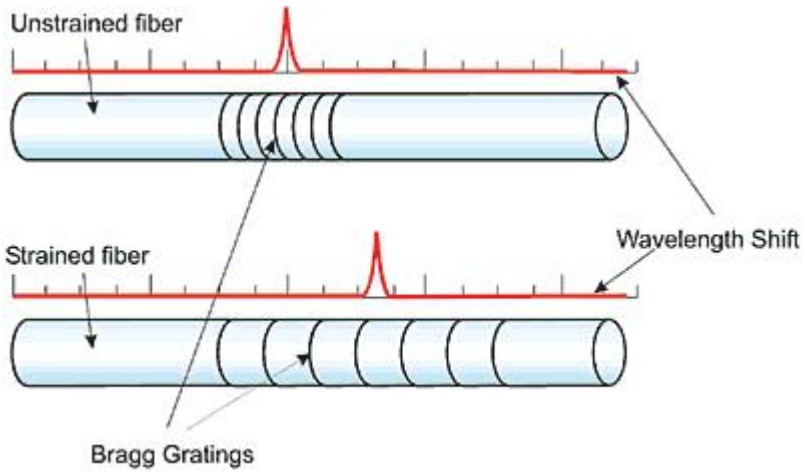

Figure 1-2: Conceptual Sketch of Axial Strain Bragg Grating Sensor (Brigham Young University, 2004)

Transverse strain sensing using axial Bragg gratings have been demonstrated experimentally and show promise for sensing (Lawrence, et al., 1999). However, these fibers have a number of drawbacks as the Bragg grating must be manufactured in a special class of optical fiber. Also, since the Bragg grating is written in the axial direction, it is most well suited for measurement of strain in this direction, and therefore is not optimal for transverse strain sensing.

Traditional optical fiber and hole assisted fiber guides light by total internal reflection. A new class of fiber that has recently become commercially available guides light by a Bragg reflection in the transverse direction. As in axial Bragg gratings these fibers reflect back a limited spectrum of wavelengths that match the period of index of refraction perturbations. In the case of the Photonic Bandgap (PBG) fiber the graduations are not along the core of the fiber, but instead are in the cladding of the fiber surrounding a lower index of refraction core. The light is reflected back into the core by the Bragg reflection and is confined and guided along the core of the fiber. PBG fibers rely on precise geometric alignment of the holes around the core and the index of refraction of the cladding material. The sensitivity of these fibers to transverse strain due to the change in geometry and the strain-optic effect has not been studied, but offers a new possible transverse sensing technology which will be explored in this direction.

1.2 Objectives

The goal of this study is to analyze the bandgap changes in PBG fiber under transverse load. Analytical methods used to investigate the guiding properties of these fibers will be discussed and an optimal technique will be chosen. The method will be compared to benchmark examples of conventional step index single mode fiber and PBG fiber.

The bandgap will be calculated for a benchmark fiber design under strain up to approximately 6%. The models will be run using both a planar load and a uniform pressure load. To examine the impact of mechanical and optical properties on the results the models will be run for both silica and polymethyl methacrylate (PMMA). The relationship between the geometric change and strain-optic effect for each principal optical axis will be studied. The mechanical and optical properties critical to sensor performance will be detailed.

1.3 Structure of the Thesis

The first chapter gives the motivation for the research and describes the basic state of the art for strain sensing using existing techniques. The objectives and scope of the research are also discussed. The second chapter discusses the fundamental equations, guided mode solution techniques and a literature review covering sensing applications for three classes of fibers. First traditional total internal reflection (TIR) fibers are covered, followed by hole assisted (HA) fibers and finally, Photonic Bandgap (PBG) fibers. Also presented are two effects, material dispersion and the strain-optic effect, which apply to all three fiber types.

Chapter three presents the finite element method (FEM) solution technique for electromagnetic models. Verification for a TIR FEM solution will be presented for guided mode solutions and core confinement against an analytical solution. Also presented will be verification of the FEM method for guided mode solutions for an undeformed PBG fiber against published analytical results. A method to define guided modes for PBG fibers will presented and verified.

Chapter four presents the results of applying the FEM for a published fiber design for silica and PMMA. Two loading conditions will be applied, first a planar load and second, a uniform pressure load. For each material and loading case the effect on the bandgap due to material, optical, and loading will be discussed.

Chapter five discusses the conclusions drawn from the research and presents opportunities for future research.

CHAPTER II

Fundamental Equations

2.1 Introduction

Traditional optical fibers rely on total internal reflection (TIR) to propagate lightwaves without loss over large distances. The mathematical equations describing lightwave propagation through these fibers are well known and can be simplified to allow for analytical or semi-analytical solutions of the equations. On the other hand, the complex geometry of the three-dimensional wave propagation that governs lightwave confinement in and propagation through Photonic Bandgap (PBG) fibers means that we may not take advantage of these same assumptions. Therefore, while the fundamental electromagnetic equations are still valid the simplifying assumptions do not hold. This requires the calculation of the lightwave propagation properties through numerical solution techniques.

In this chapter the basic TIR fiber is first introduced to familiarize the reader with the concept of lightwave propagation in an optical fiber waveguide and the properties of guided modes. The hole assisted (HA) fiber is then discussed as a intermediate fiber type to introduce the concept of complex valued propagation constants while still maintaining lightwave guiding through TIR. Finally, propagation through a PBG is introduced which requires the concepts of both complex valued propagation constants and full three-dimensional wave propagation.

2.2 Index Guided Fibers

A traditional step index optical fiber consists of a core of material with one index of refraction (n_2) and a cladding of a second index of refraction (n_1) lower than that of the core. Common fibers used in telecommunications use a core consisting of silica doped with germanium to increase the index and a cladding of pure silica. The geometry and coordinate system of the step-index fiber to be analyzed in this section are shown in Figure 2-1. The region surrounding the fiber can range from air to a non-transparent coating, however the

details of this region do not affect the properties of the guided modes. We can assume an infinite cladding radius for modes that are well confined in the cross-section. As will be seen later, the condition that $n_1 > n_2$ must exist for propagation using total internal reflection.

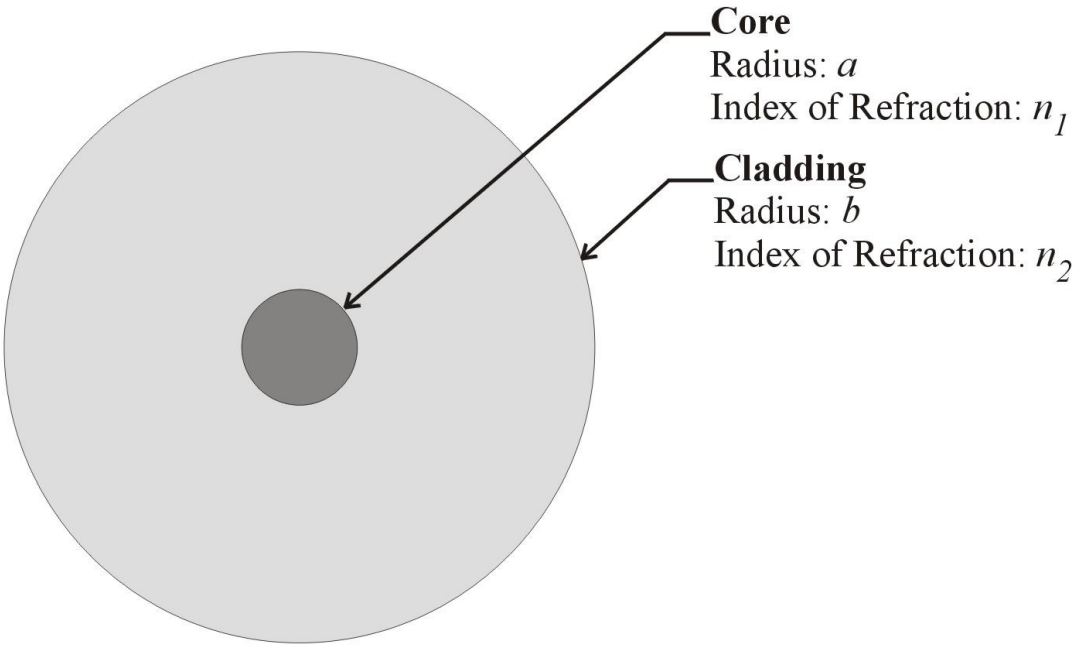

Figure 2-1: Conventional Step Index Fiber

2.2.1 TIR Guided Mode Solutions

The propagation of electromagnetic waves through a transparent medium can be described by Maxwell's equations assuming no electromagnetic source or sink. The medium can be homogenous or heterogenous, for which the index of refraction varies between the constituents. We write the equations in terms of cylindrical coordinates: r, ϕ, and z where z is the direction of propagation,

$$\nabla \times E = -\frac{\partial B}{\partial t} = -\mu_0 \frac{\partial H}{\partial t} \tag{2.1}$$

$$\nabla \times H = \frac{\partial D}{\partial t} = \varepsilon_0 n^2 \frac{\partial E}{\partial t} \tag{2.2}$$

$$\nabla \cdot D = 0 \tag{2.3}$$

$$\nabla \cdot B = 0 \tag{2.4}$$

where E represents the electric field, B is the magnetic induction, H is the magnetic field intensity, D is the electric displacement, μ_0 is the free space magnetic permeability ($4\pi \times 10^{-7}$ N/A^2), and ε_0 is the free space dielectric permittivity ($8.8541878176 \times 10^{-12}$ F/m). n is the refractive index distribution within the material which may be a function of the spatial variables r and θ.

Furthermore, we have the constitutive relationships for the electric displacement B, and magnetic induction, D,

$$B = \mu_0 H \tag{2.5}$$

$$D = \varepsilon E = \varepsilon_0 n^2 E\,. \tag{2.6}$$

The electric and magnetic fields remain orthogonal to one another during propagation. To simply Maxwell's equations, we take the curl of equation (2.1),

$$\nabla \times (\nabla \times E) = -\mu_0 \frac{\partial}{\partial t}(\nabla \times H)\,. \tag{2.7}$$

Now substituting equation (2.2) into (2.7),

$$\nabla \times (\nabla \times E) = -\mu_0 \frac{\partial}{\partial t}(\varepsilon_0 n^2 \frac{\partial E}{\partial t}) = -\varepsilon_0 \mu_0 n^2 \frac{\partial^2 E}{\partial^2 t} \tag{2.8}$$

and using the vector identity,

$$\nabla \times (\nabla \times E) = \nabla(\nabla \cdot E) - \nabla^2 E \tag{2.9}$$

gives,

$$\nabla(\nabla \cdot E) - \nabla^2 E = -\varepsilon_0 \mu_0 n^2 \frac{\partial^2 E}{\partial^2 t}\,. \tag{2.10}$$

Combining equations (2.3) and (2.5)

$$\nabla \cdot D = \varepsilon_0 \nabla \cdot (n^2 E) = \varepsilon_0 \left[\nabla n^2 \cdot E + n^2 \nabla \cdot E \right] = 0\,, \tag{2.11}$$

we can solve for $\nabla \cdot E$,

$$\nabla \cdot E = -\frac{1}{n^2} \nabla n^2 \cdot E\,. \tag{2.12}$$

Substituting this result into (2.10), yields

$$\nabla^2 E + \nabla\left(\frac{1}{n^2}\nabla n^2 \cdot E\right) - \varepsilon_0 \mu_0 n^2 \frac{\partial^2 E}{\partial^2 t} = 0 . \tag{2.13}$$

Similar steps can be applied to the magnetic equations to obtain

$$\nabla^2 H + \frac{1}{n^2}\nabla n^2 \times (\nabla \times H) - \varepsilon_0 \mu_0 n^2 \frac{\partial^2 H}{\partial^2 t} = 0 . \tag{2.14}$$

Within either the core or cladding region of the step-index fiber, the medium is homogenous and there is no spatial variation in the refraction,

$$\nabla n = 0 . \tag{2.15}$$

This eliminates the ∇n term from equations (2.13) and (2.14) yielding,

$$\nabla^2 E - \varepsilon_0 \mu_0 n^2 \frac{\partial^2 E}{\partial^2 t} = 0 \tag{2.16}$$

$$\nabla^2 H - \varepsilon_0 \mu_0 n^2 \frac{\partial^2 H}{\partial^2 t} = 0 . \tag{2.17}$$

Equations (2.16) and (2.17) are now uncoupled and thus the electric and magnetic equations can be solved separately.

The solutions to equations (2.16) and (2.17) can be assumed planar waves of the form

$$E = E(r,\phi)e^{i(\omega t - \beta z)} \tag{2.18}$$

$$H = H(r,\phi)e^{i(\omega t - \beta z)} \tag{2.19}$$

where ω is the angular frequency and β is the phase shift per unit distance.

Substituting (2.18) into (2.16) and rearranging yields the scalar wave equation for the electric field,

$$\frac{\partial^2 E}{\partial r^2} + \frac{1}{r}\frac{\partial E}{\partial r} + \frac{1}{r^2}\frac{\partial E^2}{\partial \phi^2} + \left[k_0^2 n^2(r) - \beta^2\right]E = 0 . \tag{2.20}$$

where the free space wave number is defined as

$$k_0 = \frac{\omega}{c}. \tag{2.21}$$

A similar equation can be derived for the *H* field, but since these can be solved independently with the same mode solution we need only consider *E*. To continue, a separation of variables is performed since *n* is only a function of *r*, not ϕ, for the step-index fiber,

$$E(r,\phi) = E_r(r)E_\phi(\phi)\,. \tag{2.22}$$

Equation (2.20) then becomes,

$$\frac{r^2}{E_r}\left(\frac{d^2E_r}{dr^2} + \frac{1}{r}\frac{dE_r}{dr}\right) + r^2\left[n^2(r)k_0^2 - \beta^2\right] = -\frac{1}{E_\phi}\frac{d^2E_\phi}{d\phi^2} = +l^2 \tag{2.23}$$

where in equation (2.23) the RHS is a function of *r* and the LHS is a function of ϕ. Both sides must thus be equal to a constant, here defined as l^2. Solving the RHS yields,

$$E_\phi(\phi) = \sin\left(l\left[\phi + \phi_0\right]\right) \tag{2.24}$$

Where ϕ_0 is an arbitrary constant. We therefore take $\phi_0 = 0$ for simplicity. Similarly, we can write $H_\phi(\phi) = \cos(l\phi)$ for the magnetic field solution to guarantee orthogonality between the fields. Rewriting the LHS yields,

$$r^2\frac{d^2E_r}{dr^2} + r\frac{dE_r}{dr} + \left(r^2\left[n^2(r)k_0^2 - \beta^2\right] - l^2\right)E_r = 0 \quad l = 0,1,2,.. \tag{2.25}$$

Now we solve equation (2.25) in core of the fiber,

$$r^2\frac{d^2E_r}{dr^2} + r\frac{dE_r}{dr} + \left(U^2\frac{r^2}{a^2} - l^2\right)E_r = 0 \quad 0 < r < a \tag{2.26}$$

with,

$$U = a(k_0^2n_1^2 - \beta^2)^{1/2}\,. \tag{2.27}$$

The solution to equation (2.27) is in terms of the Bessel functions of the first kind J_l,

$$E_r(r) = A_0J_l(Ur/a) \tag{2.28}$$

where A_0 is an arbitrary constant.

Similarly we solve (2.25) in the cladding of the fiber:

$$r^2 \frac{d^2 E_r}{dr^2} + r \frac{dE_r}{dr} - \left(W^2 \frac{r^2}{a^2} + l^2 \right) E_r = 0 \quad r > a \tag{2.29}$$

with,

$$W = a(\beta^2 - k_0^2 n_2^2)^{1/2}. \tag{2.30}$$

The solution to equation (2.30) is in terms of the modified Bessel functions of the second kind K_l,

$$E_r(r) = B_0 K_l(Wr/a) \tag{2.31}$$

where B_0 is an arbitrary constant.

To apply the conditions at the core-cladding boundary ($r=a$) we apply the "weakly guided assumption" (Gloge, 1971). This simplification assumes that the electric field is continuous at the boundary and is valid if there is not a significant change in index of refraction on either side, i.e.

$$\frac{(n_1 - n_2)}{n_1} << 1 \quad \Rightarrow \quad n_1 \approx n_2 \tag{2.32}$$

First we apply the continuity condition,

$$E_{r(core)} = E_{r(clad)} \tag{2.33}$$

to equations (2.28) and (2.31) which yields

$$B_0 = A_0 \frac{J_l(U)}{K_l(W)} \tag{2.34}$$

Second we apply the continuity condition,

$$\frac{d(E_{r(core)})}{dr} = \frac{d(E_{r(clad)})}{dr} \tag{2.35}$$

and recurrence relations for the Bessel functions to obtain the following relationship for the propagation constants β

$$U \frac{J_{l+1}(U)}{J_l(U)} = W \frac{K_{l+1}(W)}{K_l(W)}. \tag{2.36}$$

From this relationship distinct guided modes may be calculated for each value l. These modes are linearly polarized and are denoted LP_{lm}. The β values are calculated giving the

propagation constants for each guided mode using equation (2.36). An effective index of refraction for each propagating mode LP_{lm} may then be calculated using the following relationship,

$$n_{eff} = \frac{\beta}{k_0} \tag{2.37}$$

where n_{eff} is the index of refraction of a homogeneous material through which the lightwave would propagate with the same constant β. For TIR propagation n_{eff} is known to be between the index of the core and the cladding.

$$n_2 < n_{eff} < n_1 . \tag{2.38}$$

Combining equations (2.28) , (2.31) and (2.18), we find the amplitude of the electric field throughout the cross-section. The power distribution of this mode is proportional to the square of the amplitude and can be written as

$$P_{lm} = \begin{array}{ll} P_0 J_l^2(Ur/a)\cos^2(l\phi) & r \le a \\ P_0 \left[J_l(Ur/a) / K_l(wr/a) \right]^2 K_l^2(Wr/a)\cos^2(l\phi) & r \ge a \end{array} \tag{2.39}$$

where P_0 is the maximum power in the cross-section.

The fundamental mode is the LP_{01} mode and is the one whose power is the most confined within the core. This definition will apply to other fiber types later, even though the guiding mechanisms are different. To generalize these relationships between different step-index optical fibers they may be expressed in terms of a normalized propagation constant,

$$b = \frac{\frac{\beta^2}{k_0^2} - n_2^2}{n_1^2 - n_2^2} \tag{2.40}$$

where,

$$0 < b < 1 \tag{2.41}$$

for guided modes and a normalized frequency given by,

$$V = k_0 a \sqrt{n_1^2 - n_2^2} \tag{2.42}$$

Using the generalized propagation and frequency values the following plot may be generated for any step-index fiber. For any value of β, one or more modes may be found in the range of $0 < b < 1$. The most confined, the fundamental mode, is the LP_{01} mode and is present for all values of V.

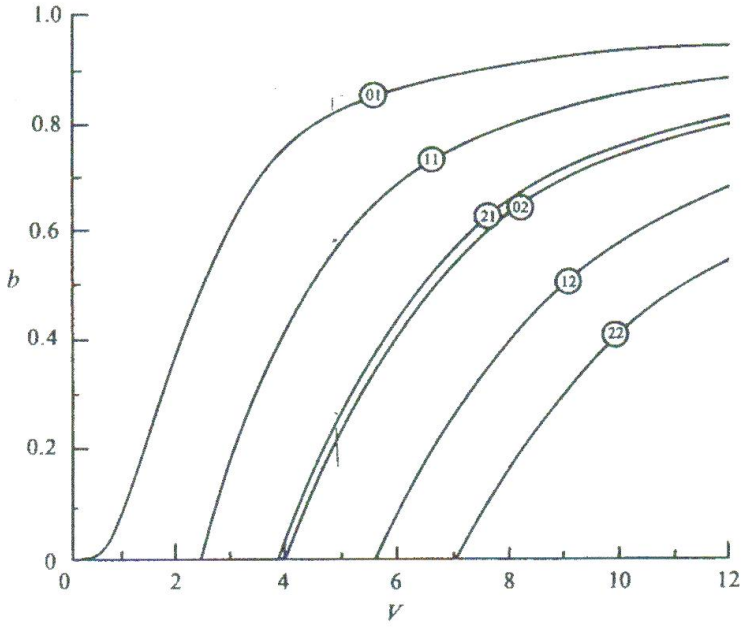

Figure 2-2: Normalized Wave Number by Normalized Propagation Constant for Guided Modes for TIR Fibers (Gloge, 1971)

The concepts of multiple propagating modes, unique propagation constants β, and different power distributions for each mode apply to fibers that rely on other means for lightwave propagation as well. For another class of fibers, Hole Assisted (HA) fibers, propagation constants can take on complex values, whereas the cladding is heterogeneous and will be defined by an effective cladding index. Photonic Band Gap fibers also have complex propagation constants but the analysis techniques are more involved since the concept of effective indices may not be applied for solutions.

2.2.2 Sensing Literature Review – TIR Fiber

Fiber optic strain sensors operating by measuring the change in properties of propagating lightwaves were primarily designed to measure the component of stain along the axis of the fiber. The sensitivity of these sensors to this strain component is an order of magnitude greater than any other component. With the advent of fiber optic Bragg gratings the ability to make local, stable axial strain measurements was greatly enhanced (Kersey et al., 1992). Bragg fiber based sensors also offer the advantage of absolute position information, previously not possible with conventional interferometric techniques. Applied transverse strains were originally considered to be a source of noise for axial sensors since it creates an "apparent" axial strain. Fibers designed to be polarization maintaining (PM) were used to minimize this effect for axial strain measurements. PM fibers (see Figure 2-3 for typical example) have two preferential, orthogonal axes in the cross-section which divide the fundamental mode into two orthogonal modes with slightly different propagation constants β_{slow} and β_{fast}. The fundamental idea is that both modes have the same sensitivity to axial strain, but slightly different sensitivity to transverse strain components.

Due to this slight difference in sensitivities, the measurement of transverse strain is more difficult than axial measurement and an early approach to measure transverse strains used a Bragg grating sensor in combination with traditional electrical strain gauges at prescribed angles (Kim et al., 1993). Using the data from these sensors the transverse strain could be calculated. Later efforts concentrated on characterizing the transverse strain effects on polarization maintaining fibers containing Bragg gratings (Lawrence et al., 1999). This approach had the advantage of using only one fiber sensor. The birefringence of the fiber splits the Bragg spectral response into two spectral peaks. The system response is measured by monitoring the spectrum around these spectral peaks. This approach can be used to measure transverse strain for many applications where such measurements were previously not available, but with significant drawbacks.

As with many other sensors, Bragg PM fibers are temperature sensitive as the thermal expansion and contraction of the sensor may change the Bragg grating period and the index

of refraction is temperature dependant as well. To overcome this limitation a reference fiber may be used to measure the temperature effect, but this introduces a second sensor into the system.

Another issue with the PM Bragg fiber approach is due to the nature of the design of PM fiber. The PM fiber is created by prestressing the fiber cladding to guarantee a predetermined amount of birefringence. To overcome the PM fiber geometry effect a calibration of the fiber must be performed and the fiber orientation must be known during loading for best results are concerns.

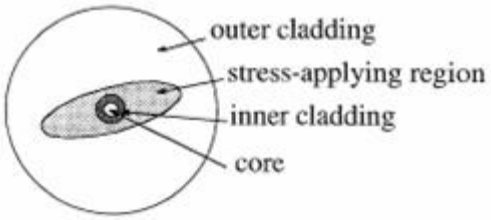

Figure 2-3: PM Fiber Typical Cross-Section (Lawrence, et al., 1999)

Furthermore, to retrieve axis specific strain information the sensor must be monitored at two wavelengths, and for best results a spectral scan around both spectral peaks should be done. This increases the complexity of the test equipment and slows the speed of the measurement. Finally, as mentioned earlier, the fact than an optical fiber which is not very sensitive to transverse strain is being used to measure this component adds considerable noise to the measurements. Each of these concerns can be reduced or eliminated through the use o microstructured fibers, as will be discussed in the following sections.

2.3 Hole Assisted Fibers

Another class of fibers that rely on TIR are Hole Assisted (HA) fibers. Fibers of this type still rely on the fundamental relationship of the core index being higher than the cladding index. However, HA fibers have a series of periodic holes in the cladding that run parallel to the core.

A typical fiber of this type from Blaze Photonics is shown in Figure 2-4. The holes introduce air or another media into the cladding that has the effect of changing the index of refraction relationship between the core and cladding. For telecommunication applications, air is typically proposed as the cladding effective index is below that of silica and the mode confinement is stronger.

The relative index of the core and the effective cladding index is thus outside the limits defined for use of the weakly guided assumption. While HA fibers are more difficult to manufacture than conventional TIR optical fibers the hole arrangement around the core need not be perfectly symmetric since the guiding mechanism is still through total internal reflection. Therefore the manufacturing difficulty may not be as high as expected.

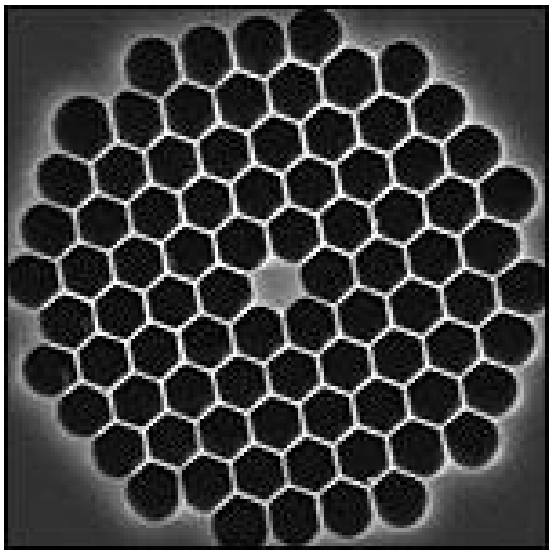

Figure 2-4: Thor Labs NL-1.5-670-02

2.3.1 Properties of Guided Modes

Similar modeling and solution techniques used for conventional TIR fibers may be used for HA fibers. The analytical solutions obtained for TIR fibers may be used after the cladding is homogenized based on an effective index that includes the holes and cladding material index.

Methods to perform this homogenization and therefore solve for guided modes will be discussed later in section 2.5.

The propagation constant β for HA fibers have both real and imaginary components meaning that the modes are "leaky." The real part of β represents the phase shift per unit displacement for the guided mode as in the TIR analysis. $|\mathrm{Im}(\beta)|$ is a measure of the power radiated due to confinement loss as the mode propagates.

The Imaginary part of β is relatively small, and in popular analysis it is accepted to ignore Im(β) and search for the Re(β) in a method similar to TIR fibers using an effective index of refraction from the composite of the holes and cladding, n_{clad} (Koshiba and Saitoh, 2004). This real part of the index is still governed by the bounds that exist for TIR fibers $n_{clad} < \mathrm{Re}(n_{eff}) < n_{core}$ and similar parameters of dispersion, and mode field diameter transfer from the TIR fibers.

Finally the concept of a guided mode is no longer mathematically rigorous for HA fibers as all modes are inherently lossy. We still apply the same principals for TIR fibers since these have been demonstrated to match experimentally measured results (Zolla, et al., 2005).

A key paper by Kuhlmey et al. demonstrated that the numerically calculated values of Re(β) and Im(β) correspond to their expected physical values (Kuhlmey, et al., 2002a). Previous authors had claimed that HA fibers were "endlessly singlemode." However, the Kuhlmey paper demonstrated that a cutoff wavelength exists for the *LP01* mode above which the mode is not sufficiently confined to propagate. As the wavelength is decreased the mode becomes more and more confined (β increases). In particular, the magnitude of Im(β) corresponds inversely to the mode confinement. An important conclusion to draw is that the existence and labeling of a mode should be based on confinement rather than strictly the values of β. This distinction will become even more important later on for photonic bandgap fibers.

2.3.2 Sensing Literature Review – HA Fibers

The application to transverse strain sensing is similar to that for the previous TIR fibers. The primary benefit is a result of lowering the modulus of the cladding material, allowing larger deformations and changes to the index of the cladding material at a given load, therefore increasing the sensitivity to transverse strain. The fundamental challenges associated with characterizing intensity changes of guided modes due to strain are similar to conventional TIR fibers.

HA fibers are also more strongly guided and therefore more robust for insertion into structures for sensing with low intensity losses. Most intriguing are the open cavities in the structure of the fiber. By flooding the holes in the cladding with fluids a range of new sensing applications are possible. Fluids may be used that change index of refraction within the holes. For HA fibers a fraction of the fundamental modal power propagates in the cladding holes and through whatever fluid resides in them (Monroe et al., 1999). For example, the fluid may be a gas with unknown pollutants. By analyzing the spectral output of the fiber the pollutants may thus be characterized.

HA fibers have additional advantages over conventional fibers in that they demonstrate a greatly reduced temperature sensitivity and can be made highly birefringant through a number of methods. (Nasilowski, et al. 2003). Fibers of this design with core asymmetry have been shown to have sensitivity to strain without the temperature sensitivity of conventional TIR fibers making them good candidates for multiparameter sensors. (Nasilowski, et al., 2005, Monroe et al., 2001).

2.4 Photonic Band Gap Fibers

PBG fibers propagate light using an entirely different mechanism than TIR. PBG fibers confine light to the core using a transverse Bragg reflection. Their structure is uniquely different that the previous two fiber in that the core has a lower index of refraction than the cladding and the core may be open with light propagating in air (Birks, et al., 1995, Cregan, et al., 1999). Similar to a longitudinal Bragg grating where the periodic changes to index of

refraction change axially and when the wavelength matches this pitch it is reflected as seen in Figure 2-5. A PBG fiber relies on this phenomenon in the transverse direction as seen in Figure 2-6.

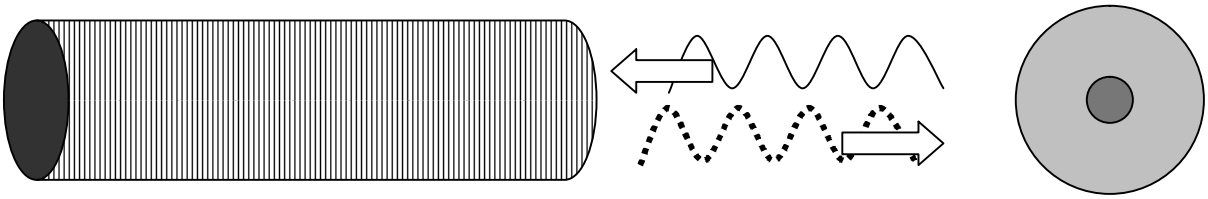

Figure 2-5: Axial Bragg Grating

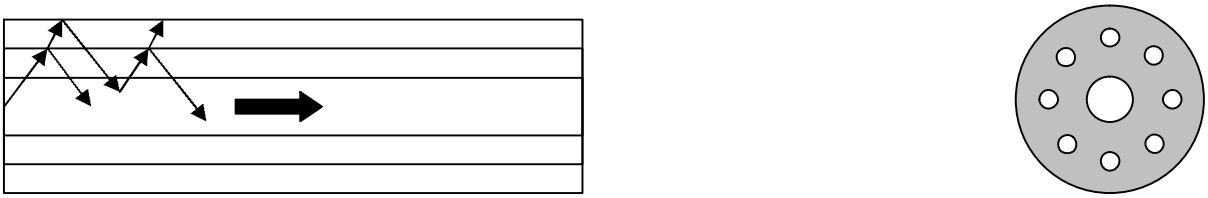

Figure 2-6: Transverse Bragg PBG Fiber

The concept of the "Bragg Fiber" was first introduced in 1978 (Yeh and Yariv, 1978). Until relatively recently the challenges of manufacturing a fiber of this design were too difficult to overcome. Two decades later, with improvement in fabrication techniques, fibers have started to be manufactured and their properties began to be studied (Knight et al., 1996). Since this time the properties of PBG fibers have been optimized primarily for telecommunications applications and only a few designs are commercially available. One of these fibers from Blaze Photonics is shown in Figure 2-7. In 2005 a polymer PBG fiber was introduced demonstrating that photonic bandgap transmission can be obtained in other materials (Argyros et al., 2005).

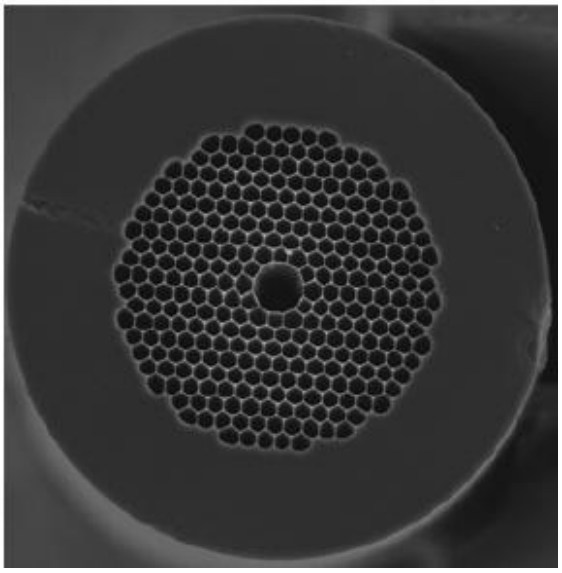

Figure 2-7: Crystal Fibre A/S - HC-1550-02

2.4.1 Analytical Solution

The "weakly guided" assumption allowing the previous solution of Maxwell's equations presented in section 2.2.1 does not hold and thus scalar solutions to propagation do not exist for PBG fibers. Full vectorial solutions must be thus obtained. Equation (2.13) may be written in the following form,

$$\vec{\nabla}\times\vec{\nabla}\times\vec{E}-\left(\frac{\omega_n}{c}\right)\varepsilon\vec{E}=0 \tag{2.43}$$

and a simlar equation for the magnetic field may be written,

$$\vec{\nabla}\times\left(\frac{1}{\varepsilon}\vec{\nabla}+\vec{H}\right)-\left(\frac{\omega_n}{c}\right)^2\vec{H}=0 \tag{2.44}$$

.

Analytical solutions are not readily obtained to these equations. One simplifying assumption where the fiber is assumed to be a perfectly 3D periodic media may be used. For this case equation (2.44) reduces to a eigenvalue problem where $\omega_n(\vec{k})$ are the eigenvalues, $\vec{E}=e^{i\vec{k}\cdot\vec{r}}\vec{E}_{n,\vec{k}}$, $\vec{r}$ is the position vector, and $\vec{E}_{n,\vec{k}}$ must satisfy,

$$\left(\vec{\nabla}+i\vec{k}\right)\times\left[\left(\vec{\nabla}+i\vec{k}\right)\times\vec{E}\right]-\left(\frac{\omega_n}{c}\right)^2\varepsilon\vec{E}=0 \tag{2.45}$$

.

These solutions are called Bloch modes. $\vec{k}$ are called the Bloch wave vectors and represent the directions and propagation constants at which lightwaves may propagate. In general $\vec{k}$ includes both real and imaginary components. The real portion corresponds to the guided energy and the imaginary portion corresponds to the evanescent energy which exponentially decays from the boundaries of the fiber. For the previous step-index fiber solution, $\left|\vec{k}\right|$ reduces to β_z.

$\omega_n\left(\vec{k}\right)$ is a continuous function of $\vec{k}$ indicating that there are a range of wavelengths that propagate at a given $\vec{k}$. PBG fibers transmit light over a range of ω_n which do not yield solutions for $\vec{k}$ in the plane of the cross-section. These ω_n values are thus confined to propagate in the axial direction. This results in a core that no longer has a higher index then the cladding. In fact, the core may be only air. For air core fibers the following bounds apply,

$$\mathrm{Re}(\beta)<1<n_2k_0 \tag{2.46}$$

Finally, unlike for the case of HA fibers the magnitude of $\left|\mathrm{Im}(\beta)\right|$ may be significant.

Since even solving for Bloch modes is computationally intensive a number of numerical, alternative modeling techniques have been used to solve for the modes of propagation. The most popular are the Multipole Method and the Finite Element Method. These methods will be discussed in more detail later in the chapter.

2.4.2 Sensing Literature Review – PBG Fiber

Manufacturing techniques for PBG fibers are only now being perfected to the point to make fibers of this design practical. The sensing applications studied to date are all focused on "evanescent" sensing which involves flooding the holes with a fluid under study and

measuring the change in index of refraction of the fluid (Monroe et al., 1999). In the PBG case if the center hole is flooded it technically isn't necessarily evanescent since the light is primarily propagating in the medium under study, but the same principles apply.

PBG fibers offer all the advantages of the previous HA fibers including low temperature sensitivity, inherently stronger guidance allowing more robust deployment and strong PM properties. Under study in this dissertation is a potential advantage that PBG fibers have over HA fibers in that they may exhibit birefringence without the necessary multiple core design. PBG fibers also offer the advantage of guidance through air, dramatically lowering material losses that have restricted materials such as PMMA from being used in fiber designs for long length deployments.

2.5 Modeling Techniques

Many techniques have been proposed to solve for the guidance properties of TIR, HA and PBG fibers (Bjarklev, et al., 2003). The two primary well proven techniques are outlined in this section, the Multipole Method and the Finite Element Method. The Multipole method is more analytical in nature and attractive due to its ability to heavily use symmetry and solve for the complex propagation constants that exist within HA and PBG fibers. Recently the FEM method has also become very popular with the decreased cost of computing power and various modifications that allow for solutions to the complex propagation constants as well. Given proper implementation the methods have been shown to be in very good agreement (Uranus and Hoekstra, 2004).

2.5.1 Multipole Method

The Multipole method is widely used and well suited to symmetric cross-sections for the prediction of propagation constants and leakage loss prediction and has been verified against experimental results (Kuhlmey, et al., 2002b). This method cannot be expanded to non-symmetric cross sections or arbitrary cladding configurations however. The fundamental

formulation of the Multipole method assumes that all inclusions are cylindrical. Fourier expansions of Bessel functions are then formed around each inclusion and the center defect. In other words, the propagation problem is divided into a series of smaller propagation problems of each inclusion and boundary conditions imposed between them. The cylindrical nature of the inclusions are fundamental to both the formation of the basis functions and the boundary conditions (Zolla, et al., 2005). Manufacturing techniques of these fibers yield cross-sections that have inclusions that are more hexagonal in nature, but the cylindrical inclusion model assumption has been shown to give acceptable results as compared to experimentally measured values. However, when the deformation of the fiber results in deformations of the inclusions, the method's reliability would depend on the formation of new basis function expansions and boundary conditions around each deformed inclusion's geometry. While in theory it would be possible to reformulate the functions with enough information about the deformation, the level of complication would make the method's use unrealistic for a study of this kind. Additionally, the computational efficiency of the Multipole method comes from the fact that the inclusions are periodically arranged, therefore one does not need to solve all the inclusion problems, but rather just look for periodic solutions to the general problem. If the applied loading created deformations that were different between the inclusions, the computational requirements would increase by orders of magnitude.

2.5.2 Finite Element Method (FEM)

Similar to Bloch's theorem, the Finite Element Method (FEM) also solves equation (2.43) by solving an eigenvalue problem, however, it does not rely on the periodicity conditions of Bloch's theorem. The FEM has been well tested for electromagnetic wave problems and may compute a complex propagation constant with the proper boundary conditions, but the formulation of those boundary conditions may be complex. The major advantage of the FEM in this research is its ability to work with complex, deformed geometries in solving for propagation constants.

The goal of this research is to study the changes in confinement versus wavelength for PBG fibers under various strains. The FEM method is the optimal solution method as it can solve

for guided modes with few limitations on the fiber geometry. Additionally, the mechanical deformations of the optical fiber due to the applied loading can be calculated using the same method. However, the implementation of the FEM for the prediction of propagating modes in PBG fibers does require some interpretation of the results and new definitions of a "guided" mode, that are not present in standard electromagnetic wave FEM problems. These issues will be discussed in the following chapters as the formulation and results are presented. The details of the FEM method are given in the following chapter and therefore not presented here. The advantages and disadvantages of each method are summarized in Table 2-1.

Table 2-1: Summary of methods of PBG fiber characterization

Method	Advantages	Disadvantages
Multipole Method	• Suited for symmetric geometries • Leakage loss prediction • Less computational effort required for a given model	• Cannot analyze arbitrary cladding configurations due to basis function complexity
Finite Element Method	• Reliable (well tested) method • Accurate modal descriptions	• Complicated definition of boundary conditions to predict complex propagation constant • More computational effort for a given model

CHAPTER III

Electromagnetic FEM Modeling

3.1 FEM Fundamentals

The FEM method begins by taking the electric or magnetic wave equation (Jin, 2002),

$$\nabla \times \left(\frac{1}{\mu_r} \nabla \times E \right) - k_0^2 \varepsilon_r E = 0 \quad \text{in } \Omega \tag{3.1}$$

A functional is formed,

$$F(H) = \frac{1}{2} \iint_{\Omega} \left[\frac{1}{\mu_r} (\nabla \times E) \cdot (\nabla \times E)^* - k_0^2 \varepsilon_r E \cdot E^* \right] d\Omega \tag{3.2}$$

where the asterisk denotes complex conjugate. This equation can be discretized as follows,

$$[A] \begin{Bmatrix} E_x \\ E_y \\ -jE_z \end{Bmatrix} = k_0^2 [B] \begin{Bmatrix} E_x \\ E_y \\ -jE_z \end{Bmatrix} \tag{3.3}$$

This form of the wave equation can then be used to solve Maxwell's equations for the propagation constant which is related to the eigenvalue.

The FEM method has little restriction on the geometry, symmetry, defects, or index of refraction. Boundary conditions available are scattering, impedance and an absorbing boundary condition, which involves placing a ring of material that absorbs around the outer boundary of the fiber, called perfectly matched layers (PML). The choice of boundary conditions used in this study is discussed later in 3.3.1. The Imaginary portion of β is not computed without additional anisotropic PML boundary conditions (Saitoh and Koshiba, 2003). β is required to compute the confinement loss in the formulation presented by Saitoh

and Koshiba, but a different approach to relative confinement loss is developed for this research. Also, the modes of propagation calculated by this method are mathematically correct, but may not be valid modes for core propagation. A method of mode selection must be devised to sort the confined modes from the radiating modes.

3.2 FEM Verification - Index Guided Fibers

The first step in applying the FEM model in this study was to verify its predictions against a well understood benchmark case. The conventional silica step index fiber was chosen. Most fibers of this type manufactured support only the fundamental mode, but for analysis one supporting multiple modes was used. Modes of propagation were calculated using the scalar wave equations described in Chapter III and compared to solutions from the FEM model.

The test fiber was a benchmark case supplied with the software used for the FEM implementation in this work, Comsol Multiphysics 3.3a. The fiber has a core index of n_1=1.4457, a cladding index of n_2=1.4378. The core diameter of the fiber is 16μm and the fiber was studied at a wavelength of 1550nm.

Using mode search routines to solve the LHS and RHS of equation (2.36) a plot searching for the LP_{0X} modes was generated. A typical output is shown in Figure 2-1; obtained values for first four modes are listed in Table 3-1.

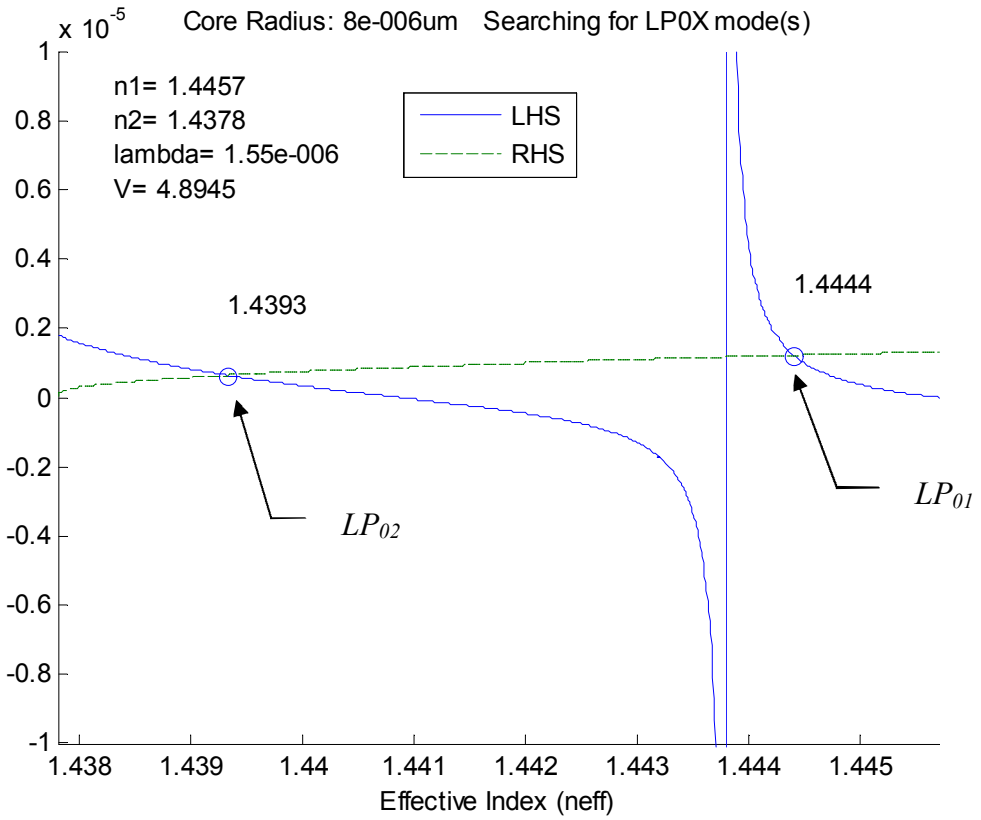

Figure 3-1: TIR Fiber Mode Searching using Scalar Wave Equations.

A similar search was done for the LP_{1X} and LP_{2X} modes.

The same fiber was then modeled using the FEM method. The modes were searched starting at $n_{eff}=n_1$ and ordered according to the n_{eff} values as explained in chapter 2. Multiple modes of propagation were found. Figure 3-2 illustrates the electric and magnetic components of the solution to the LP_{01} mode.

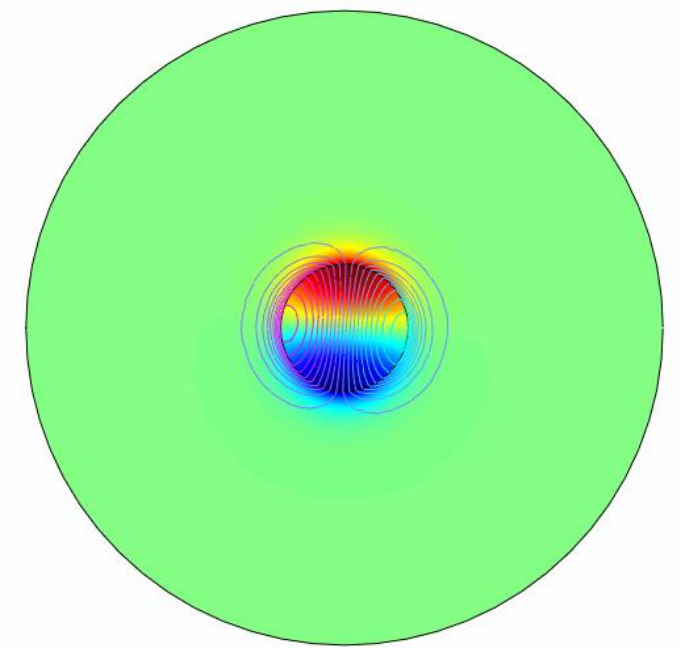

Figure 3-2: TIR Fiber Electric (Contour Lines) and Magnetic Fields (Surface Color) – LP_{01} Mode.

When comparing the solutions to the scalar wave equation and the FEM method excellent agreement was found for the four supported modes, as listed in Table 3-1.

Table 3-1: TIR Mode Solutions, Scalar Wave and FEM for 4 Supported Modes

Mode	Effective Mode Index (n_{eff})	
	Numerical Solution of Scalar Wave Equation	FEM
LP01	1.4444	1.4444
LP11	1.4425	1.4425
LP02	1.4393	1.4393
LP21	1.4400	1.4400

It is important to mention that the FEM method found other, non-propagating modes. It was important to define a technique to classify valid propagating modes from "leaky" modes.

To quantify the confinement in the core the integral of the Poynting vector is evaluated over the core region. The Poynting vector *S* is the cross product of the Electric and Magnetic fields and represents the energy flux in the propagating direction (Ghatak and Thyagarajan, 1998),

$$S = E \times H \ . \tag{3.4}$$

By integrating the flux within the core region and dividing by the overall energy flux a measure of confinement may be calculated,

$$C = \frac{P_{core}}{P_{core} + P_{clad}} = \frac{\int\limits_{\Omega_{core}} |S_z| dA}{\int\limits_{\Omega_{core}+\Omega_{clad}} |S_z| dA} \ . \tag{3.5}$$

Modes above a set level of *C* are considered guided while all others are considered "leaky" and radiated. Visual representation of $|S_z|$ over the mode represented in Figure 3-2 is shown in Figure 3-3.

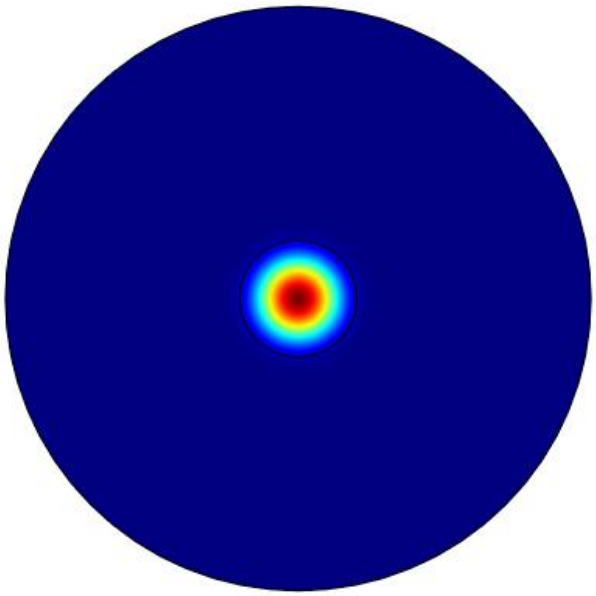

Figure 3-3: TIR Fiber Confined Mode Poynting Power - Z Direction

To confirm that the power produced for each mode matched existing solutions for the step index fiber a parametric study was performed. The power for each mode as function of wavelength (and therefore V number) were analyzed and the results plotted in Figure 3-4.

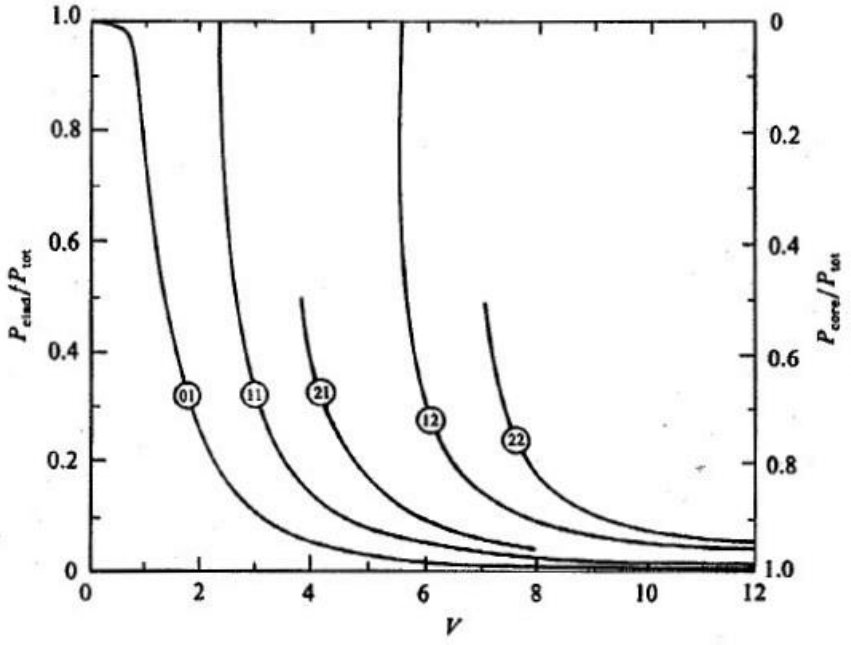

Figure 3-4: TIR Fiber Mode Power (Ghatak and Thyagarajan, 1998)

For each LP_{lm} mode the confinement was analytically calculated using the following relations (Ghatak 8.60),

$$P_{core} = C\pi a^2 \left[1 - \frac{J_{l-1}(U) J_{l+1}(U)}{J_l^2(U)} \right] \tag{3.6}$$

$$P_{clad} = C\pi a^2 \left[\frac{K_{l-1}(W) K_{l+1}(W)}{K_l^2(W)} - 1 \right]. \tag{3.7}$$

To facilitate the solution a empirical formula for calculating the normalized propagation constant was used (Ghatak, 8.42),

$$b(V) = \left(A - \frac{B}{V} \right)^2 \quad 1.5 \le V \le 2.5 \tag{3.8}$$

where A=1.142 and B=0.996.

The confinement of the fundamental mode, the LP_{01}, was then calculated using FEM and compared. The results matched well as shown in the following figure.

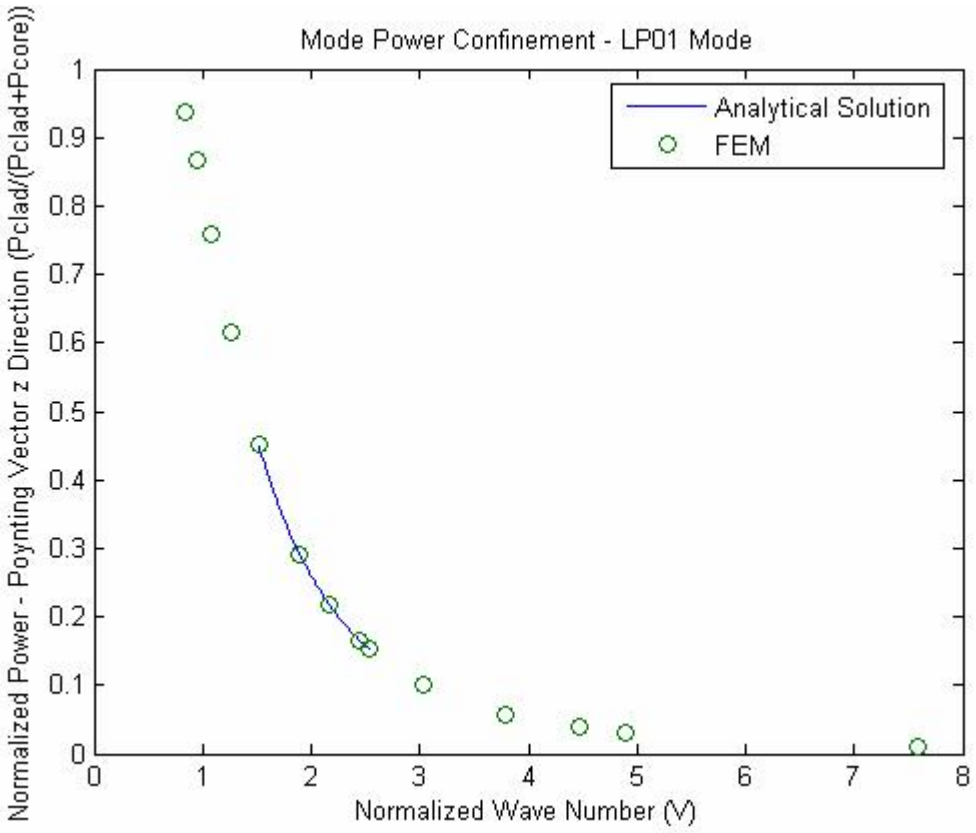

Figure 3-5: TIR Fiber Poynting Power Verification – LP_{01} Mode

Using the approximation for b over the narrow range of V matched well. The overall trend of power also matched the published results, as V increases the overall confinement increases.

The FEM model was verified to both find the modes and also to measure their confinement against known solutions for fibers using traditional TIR propagation. It was now important

to study these same conditions for PBG fibers where the propagation mechanism is a Bragg reflection.

3.3 FEM Verification – Photonic Band Gap Fibers

For PBG fibers no analytical solution exists similar to that for the TIR step index fiber. For verification the comparison must be to other accepted methods of solution. The Multipole method has been widely established to be accurate against experimental results (Kuhlmey, et al., 2002b). Using the published results of a given fiber geometry the same FEM verification was undertaken.

The fiber studied was a two ring, triangular lattice with a pitch (Λ) of 5.7816μm, a center hole diameter (D_{core}) of 13.1μm, and cladding hole diameter (d) of 4.026μm (White, et al., 2001). The FEM model consisted of 16080 Lagrange quadratic triangular elements. An impedance boundary condition was used for the reasons discussed earlier in this chapter. The refractive index of the cladding material as published is 1.39 at λ=3428nm; these parameters were also used for this comparison.

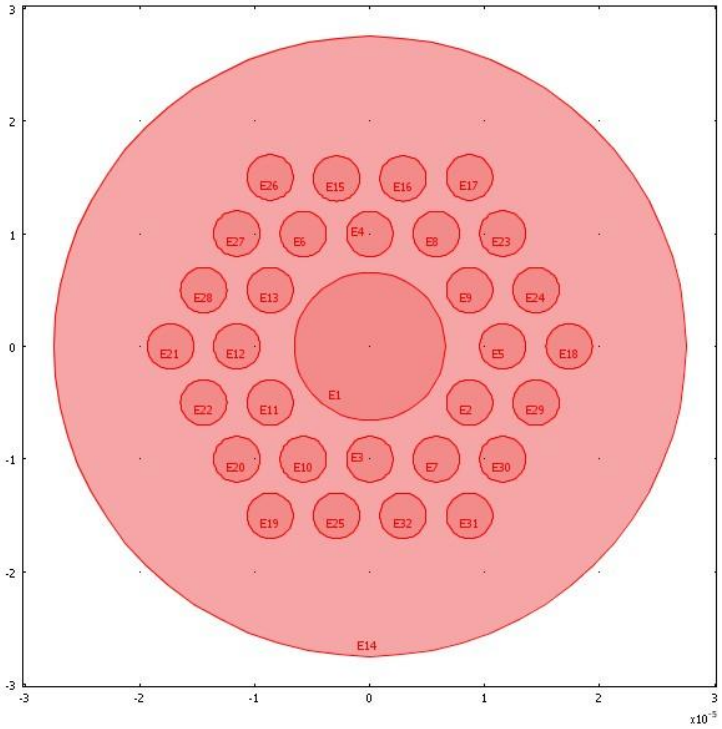

Figure 3-6: White PBG Fiber Cross-Section.

The published solution for this fiber showed a solution at an effective mode index (n_{eff}) at $0.9808734 + i\ 0.4724251 \times 10^{-3}$ at 3428nm. The FEM model implementedin Comsol Multiphysics 3.3a was thus run using seed mode values at 0.98 based on published solutions and found a confined mode at n_{eff}=0.98094.

The Poynting power, $|S_z|$, calculated using the Multipole method from the White fiber is shown in Figure 3-7.

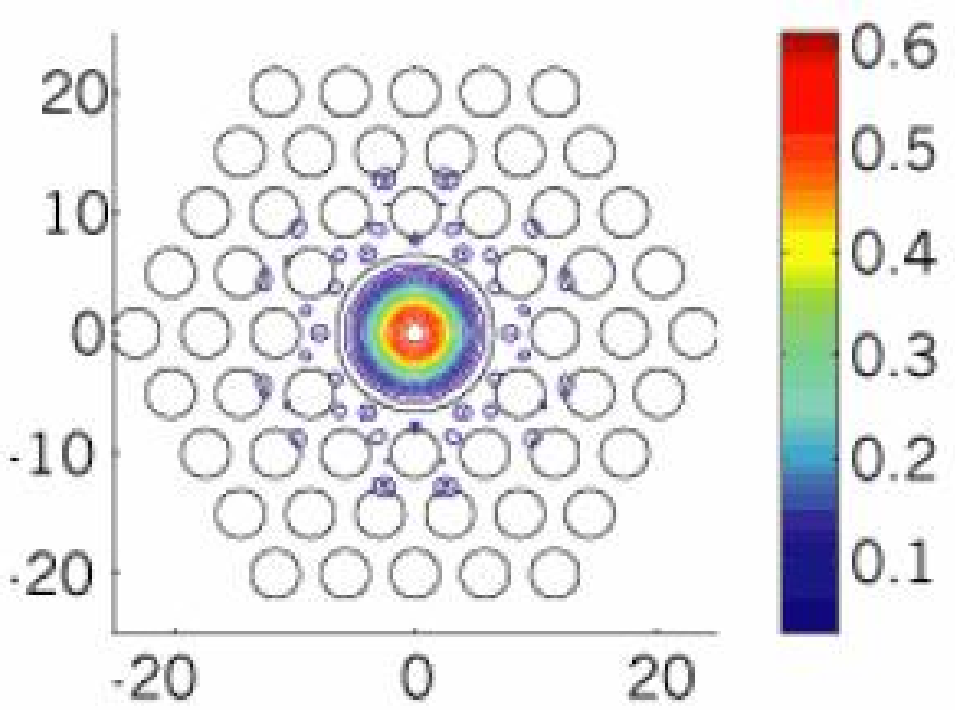

Figure 3-7: PBG Fiber Poynting Power (White et al., 2001).

The same computation was done using the FEM method. Its Poynting power is shown in Figure 3-8. Visually comparing the two plots it is clear that the fundamental mode is present and well confined to the core of the fiber.

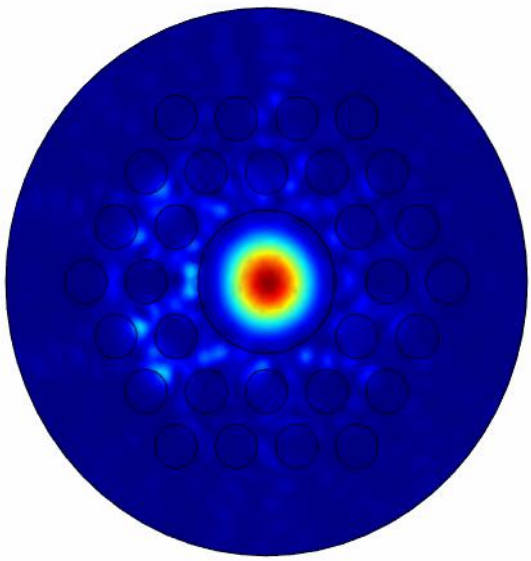

Figure 3-8: FEM modeled BPG fiber from White et al (2001).

In the case of the FEM solution other modes were calculated as were in the step index TIR study. Again it was important to classify if the mode was confined. A graphical representation of the 6 modes found for this example are shown in Figure 3-9 in the range of n_{eff}= 0.975 to 0.985.

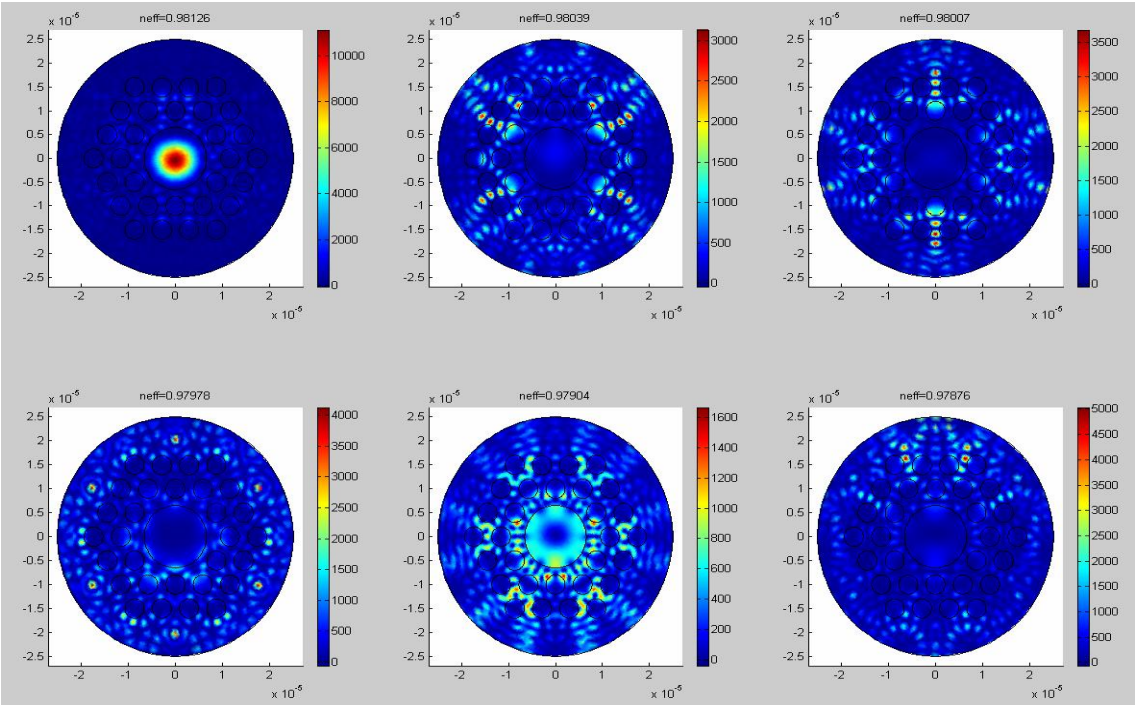

Figure 3-9: Calculated modes for fiber from White et al (2001), Fundamental and cladding modes.

Calculating *C* from equation (3.5) the fundamental mode showed greater than 60% confinement while all others are nearly zero. This can be clearly seen from Figure 3-9, confined modes looks very similar to the LP_{01} mode of a step index fiber. Since mode ordering is not available as in TIR mode finding methods, the core confinement will be used to classify guided mode solutions from the FEM output. The other modes, either mathematically spurious modes which do not exist in reality or valid cladding modes that do not propagate over any appreciable fiber length, were disregarded.

3.3.1 FEM Electromagnetic Boundary Conditions

The particular boundary conditions used for the Electro-Magnetic FEM are a critical step in the solution. Studies using the extremes of Perfectly Matched Layers inducing a electromagnetic absorbing layer physically on the model to the other end of the spectrum, using transparent boundary conditions have all been successfully implemented. (Berenger, 1994)

For the formulation used for this study with Comsol Multiphysics 3.3a, an "Impedance" boundary condition was found to be optimal. It is recognized that this is very specific to this implementation of the FEM code. Using the PML boundary condition a bandgap was calculated that did not show agreement with the published results of the published fiber, specifically at the wavelength immediate around 1550nm (Hansen et al., 2004). The comparison of the bandgap for an undeformed fiber calculated with the PML and Impedance boundary condition are shown in Figure 3-10.

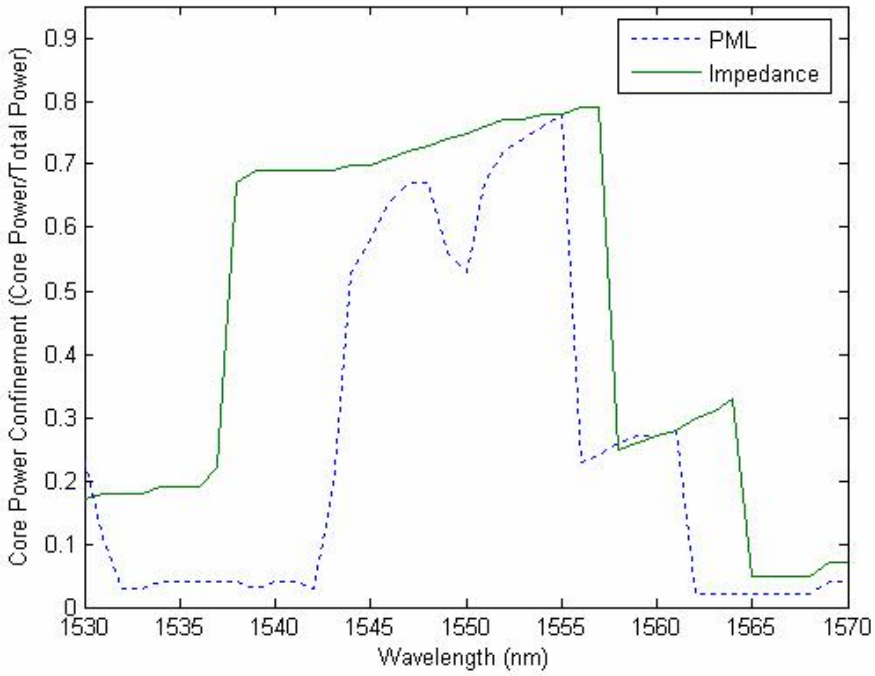

Figure 3-10: Comparison in bandgap calculated for PML and Impedance Boundary Conditions.

3.4 Response of Optical Fibers to Mechanical Loading

There are further phenomena applicable to materials used for optical guidance that are apply to all three classes of fibers. These properties are detailed in the following sections.

3.4.1 Strain-optic Effect

As loading is applied to an optical fiber, the propagation constant changes due to two effects: (1) the geometry of the cross section deforms and (2) the refractive index of optical material changes due to the strain-optic effect. In particular the study of transverse loads applied to the fiber must incorporate the resulting material optical orthotropy. In this section we describe how the strain-optic effect changes material indices of refraction locally within the waveguide materials. In the following chapter we will describe how this change is incorporated into the propagation of lightwave modes through the waveguide.

The materials constructing the optical fiber under study in this dissertation are all assumed to be initially optically isotropic. Consider an infinitesimal element of an initially isotropic material with an index of refraction n_0. The planar wave of equation (2.18) can be divided into two linearly polarized components for the material.

$$E_p = E(r,\phi)\,\mathrm{Re}\left[e^{i(\omega t-\beta_p z)}\right] = E(r,\phi)\,\mathrm{Re}\left[e^{i(\frac{2\pi}{\lambda}n_p z)}\right] \tag{3.9}$$

$$E_q = E(r,\phi)\,\mathrm{Re}\left[e^{i(\omega t-\beta_q z)}\right] = E(r,\phi)\,\mathrm{Re}\left[e^{i(\frac{2\pi}{\lambda}n_q z)}\right] \tag{3.10}$$

where n_p and n_q are the indices of refraction for the planar waves polarized about the principle optical axes in the p-q plane. These are aligned with the principle strain directions in the x-y plane (Nye, 1985). These indices of refraction can be calculated from the material dielectric tensor, B.

$$\frac{1}{n_{p,q}} = \frac{(B_2+B_3)\pm\sqrt{(B_2-B_3)+4B_4^2}}{2}. \tag{3.11}$$

For the initially isotropic material,

$$B_2 = B_3 = \left(\frac{1}{n_0}\right)^2 \tag{3.12}$$

and B_4=0. Therefore, as expected,

$$n_p = n_q = n_0 . \tag{3.13}$$

Once strain is applied to the material the dielectric tensor is modified according to,

$$\Delta B_i = p_{ij}\varepsilon_j \tag{3.14}$$

where the summation convention is applied with $\varepsilon_1 = \varepsilon_x$, $\varepsilon_2 = \varepsilon_y$, $\varepsilon_3 = \varepsilon_z$, $\varepsilon_4 = \varepsilon_{xy}$, $\varepsilon_5 = \varepsilon_{yz}$ and $\varepsilon_6 = \varepsilon_{xz}$. Equation (3.14) is known as the linear strain-optic effect. For a material that is mechanically and optically isotropic the strain-optic tensor may be written in terms of Pockel's constants in the following form.

$$p = \begin{bmatrix} p_{11} & p_{12} & p_{12} & 0 & 0 & 0 \\ p_{12} & p_{11} & p_{12} & 0 & 0 & 0 \\ p_{12} & p_{12} & p_{11} & 0 & 0 & 0 \\ 0 & 0 & 0 & \frac{p_{11}-p_{12}}{2} & 0 & 0 \\ 0 & 0 & 0 & 0 & \frac{p_{11}-p_{12}}{2} & 0 \\ 0 & 0 & 0 & 0 & 0 & \frac{p_{11}-p_{12}}{2} \end{bmatrix} \tag{3.15}$$

The mechanical, optical, and Pockel's constant for silica and the polymethylmethacrylate (PMMA) have been measured and are summarized in Table 3-2. These values will be used in all later simulations.

Table 3-2: Summary of Mechanical and Optical Material Properties of fused silica and PMMA

Property	Silica (Crystran LTD, 2007)	PMMA (Silva-Lopez et al., 2005)
Young's Modulus (GPa)	7.31	3.3
Density (g/cm^3)	2.203	1.2
Poisson's Ratio (ν)	0.16	0.34
p_{11}	0.17	0.3
p_{12}	0.36	0.297

Substituting equation (3.15) into (3.14) into (3.11) we find the principle index of refraction solutions for the strained, optically orthotropic material.

$$n_p = \sqrt{\frac{1}{\frac{1}{(n_{silica}^o)^2} + p_{12}\varepsilon_z + \frac{(p_{11}+p_{12})}{2}(\varepsilon_x+\varepsilon_y) - \frac{(p_{11}-p_{12})}{2}\sqrt{(\varepsilon_x+\varepsilon_y)^2+\varepsilon_{xy}^2}}} \tag{3.16}$$

$$n_q = \sqrt{\frac{1}{\frac{1}{(n_{silica}^o)^2} + p_{12}\varepsilon_z + \frac{(p_{11}+p_{12})}{2}(\varepsilon_x+\varepsilon_y) + \frac{(p_{11}-p_{12})}{2}\sqrt{(\varepsilon_x+\varepsilon_y)^2+\varepsilon_{xy}^2}}} \tag{3.17}$$

For each element, the updated indices of refraction are calculated from the principal strains as give in equation (3.16) and (3.17). These indices are then rotated to the global *x* and *y* coordinate system through

$$n_x = \frac{n_p n_q}{\sqrt{(n_p\cos(\theta))^2 + (n_q\sin(\theta))^2}} \tag{3.18}$$

$$n_y = \frac{n_p n_q}{\sqrt{(n_p\sin(\theta))^2 + (n_q\cos(\theta))^2}} \tag{3.19}$$

Where θ is the angle required to rotate the p axis to the x axis (Prabhugoud & Peters,2006). Individual elements may be rotated off the principal optical axis which will introduce error into a solution. In the case of the PBG solutions to follow, this effect would present as a lower overall confinement. In the cases studied for this dissertation the error was not of a magnitude that affected the search for the fundamental mode, but if a relationship between optical transmission loss and confinement loss was desired this would require further study.

3.4.2 Material Dispersion

In addition to changes in β due to wavelength for a particular mode, the index of refraction of the local optical material itself varies with wavelength, called material dispersion. As this variation is not the same order as the change in β, we normally neglect this material dispersion. However, we need to include this effect for PBG fibers since the bandgap covers a large wavelength range and therefore the material dispersion can be important. Work by W. Sellmeier in 1871 resulted in an equation for the wavelength dependant dispersion that bears his name. The three term equation is commonly used is given in equation (3.20) (Flemming, 1984).

$$n^2 - 1 = \sum_{i=1}^{3} \frac{B_i \lambda^2}{\lambda^2 - C_i^2} \tag{3.20}$$

The Sellmeier coefficients B and C are experimentally determined for each material. For silica the following coefficients listed in Table 3-3 were used for this research. The coefficients for PMMA and PMMA doped with benzyl benzoate (PMMA-BEN) listed in Table 3-3 were used as the basis to formulate a theoretically doped PMMA based material.

Table 3-3: Sellmeier Coefficients, Silica, PMMA and PMMA-BEN

Sellmeier Coefficient	Silica (CVI Melles Griot, 2007)	PMMA (Ishigure, 1996)	PMMA-BEN (Ishigure, 1996)
B_1	0.6961663	0.4963	0.4855
B_2	0.4079426	0.6965	0.7555
B_3	0.8974794	0.3223	0.4425
C_1	0.00467914826	0.00515524	0.0010878
C_2	0.0135120631	0.01378276	0.0013156
C_3	97.9340025	85.322169	2434.4

For the geometry of the PBG fiber studied in this dissertation the PMMA index of refraction for the fiber geometry under study was not ideal and produced low confinement. To optimize the waveguide for PMMA the fiber geometry could be redesigned or the index of refraction could be shifted using dopants as is commonly performed.

An index of refraction at 1550nm of 1.492 was found to give results suitable for study and this index may be achieved with dopants such as benzyl benzoate (Ishigure, 1996). The amount of dopant would vary the change in index over the wavelength range. Figure 3-11 plots the index of refraction for the pure PMMA and the PMMA-BEN using the coefficients of Table 3-3 for the UV to near infrared spectrum. As can be seen in Figure 3-11, the index can be approximated as a linear function in the wavelength range of 1530nm to 1570nm. For the PMMA fiber considered in this dissertation, the PMMA and PMMA-BEN curves were thus approximated as linear functions in this wavelength range and then extrapolated to produce at value of 1.492 at 1550nm. The new linear function given in equation (3.21) with A= -0.0029 *and* B= 1.496495 was used therefore to account for material dispersion for the PMMA cases.

$$n = A\lambda + B \tag{3.21}$$

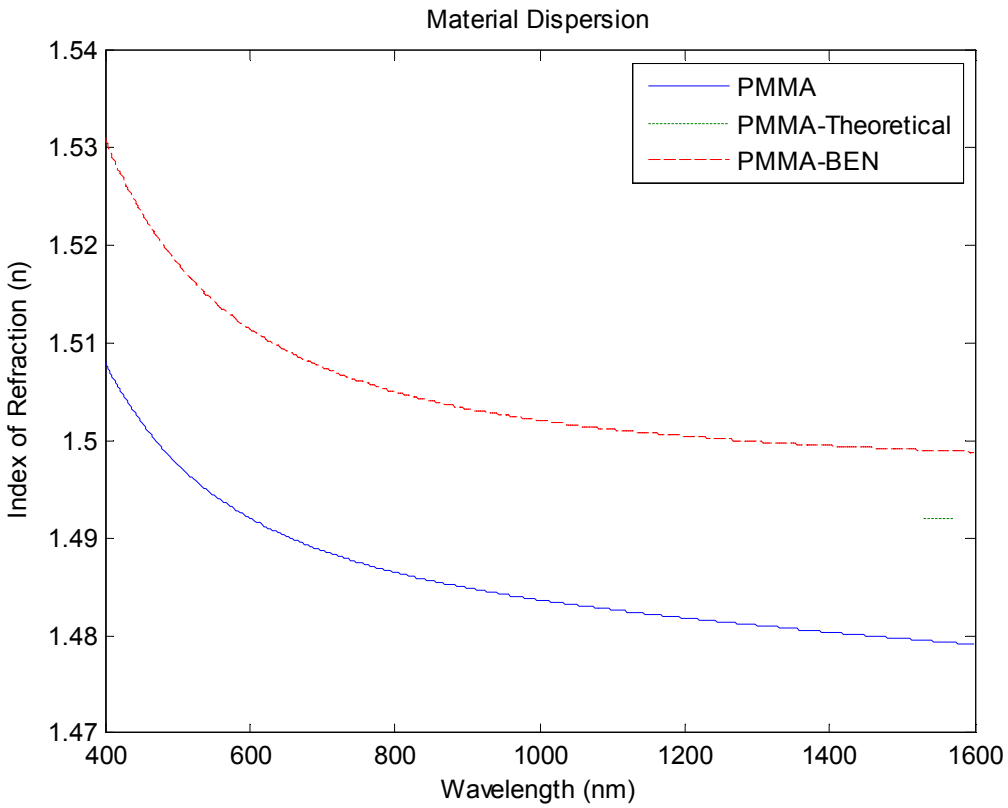

Figure 3-11: Material Dispersion for PMMA and doped PMMA.

CHAPTER IV

Fiber Analysis

To study the change in bandgap characteristics as a function of applied transverse strain, one option would be to design a fiber from first principals and optimize its response to transverse strain. The parameters that dictate PBG fiber performance are the center hole diameter (D), cladding hole diameter (d), distance between the cladding holes, commonly called pitch (Λ) and the number of rings of cladding holes (N_r). The relationships between D, d, and Λ have been determined for PBG guidance in air (Cregan, et al., 1999; Broeng, et al., 2000). More than for the other fiber types, the design space for D, d and Λ to develop a strong confinement (i.e. > 75%) over a significant bandwidth is extremely limited. Through initial parameter studies, it was found that varying any of these parameters erased the strong bandgap before a significant change in the sensitivity to transverse strain occurred. Additionally, designing an entirely new PBG fiber would not allow for an independent verification of the FEM results. As few such PBG fibers are available that have been experimentally characterized, the application of the FEM method to this new PBG fiber would require validation. Therefore, as the goal of this dissertation is to provide a proof of concept of the PBG fiber for transverse strain sensing capabilities, it was decided to use an established fiber design. For this fiber design the mechanical and opto-mechanical properties were varied to match existing fiber materials. The trends learned from this proof of concept could then be extended to future or other FBG fibers.

This fiber design of Hansen et al. (2004) for optimal transmission at 1550nm has been previously analyzed experimentally. Other fiber designs considered, including the White et al. (2001) fiber analyzed to verify the FEM model in chapter 3, and commercially available fibers from Crystal Fibre A/S. Of these fibers, the Hansen fiber had the most detailed index values for verification and relatively easy geometry to implement into a FEM model. Therefore this fiber was used for both the study of a silica and PMMA based fiber. In the case of the PMMA fiber the design was not optimal because of the index of refraction difference between silica and PMMA. The fiber could have been redesigned using the

guidelines of Cregen et al. (1999) and Broeng et al. (2000) for optimal transmission, however more information could be gained from the analysis if the fiber geometry is consistent with that of the silica case. While still not optimal, a shift in index of refraction allowed the same fiber geometry to be used for analysis (see section 3.4.2.).

The Hansen fiber studied was a four ring (N_r =4), triangular lattice with a pitch (Λ) of 2.5μm, a center hole diameter (D_{core}) of 10μm, and cladding hole diameter (d) of 1.4μm. This particular fiber matches the model of Hansen et al. (2004). For computational efficiency the number of rings of cladding holes was limited to four and a quadrant of the fiber was modeled as seen in Figure 4-1. The solution was accomplished with 6856 triangular Lagrange quadratic elements. Reducing the number of cladding holes underestimates the confinement slightly. As the sensing parameters will be based on minimum confinement criteria later on, this will be a conservative estimate.

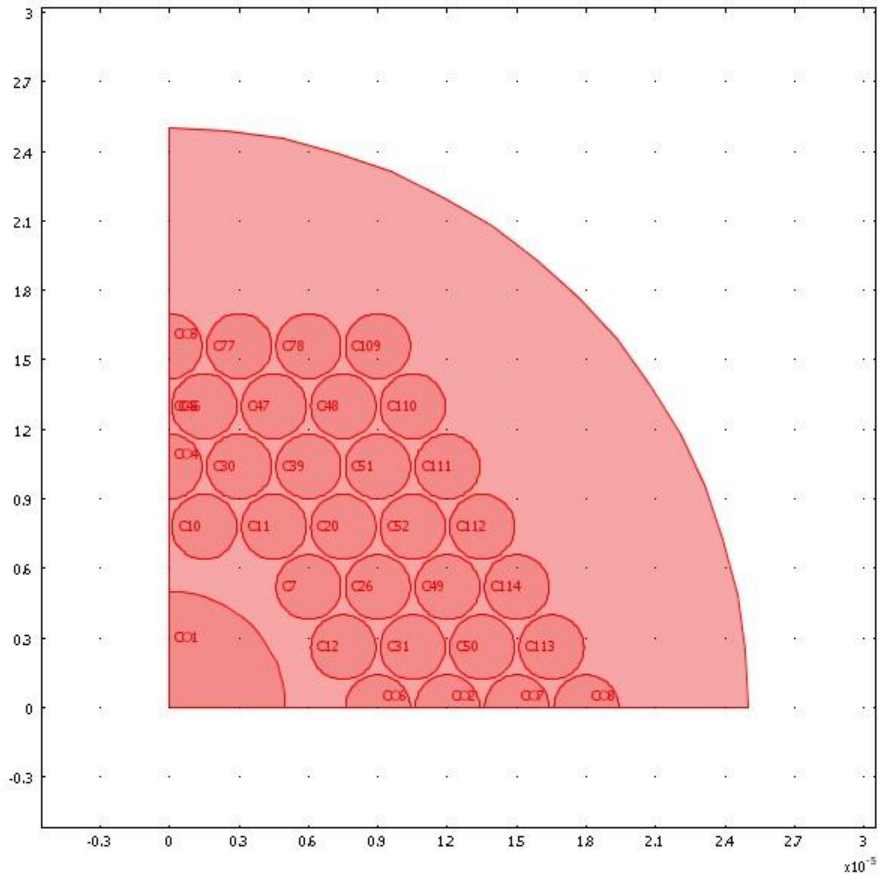

Figure 4-1: Hansen Fiber using 1/4 Symmetry.

To facilitate the solution Comsol Multiphysics version 3.3a was uses as a basis for the mechanical deformation and electromagnetic solution. While the software is capable of analyzing each loading and particular wavelength individually, it was necessary to examine solutions over a lightwave spectrum at each loading condition. To accomplish this Comsol was interfaced with Matlab. This allowed custom code to be written to loop through a range of loads and calculate the bandgap for each loading condition. A flowchart of the solution algorithm is shown in Figure 4-2.

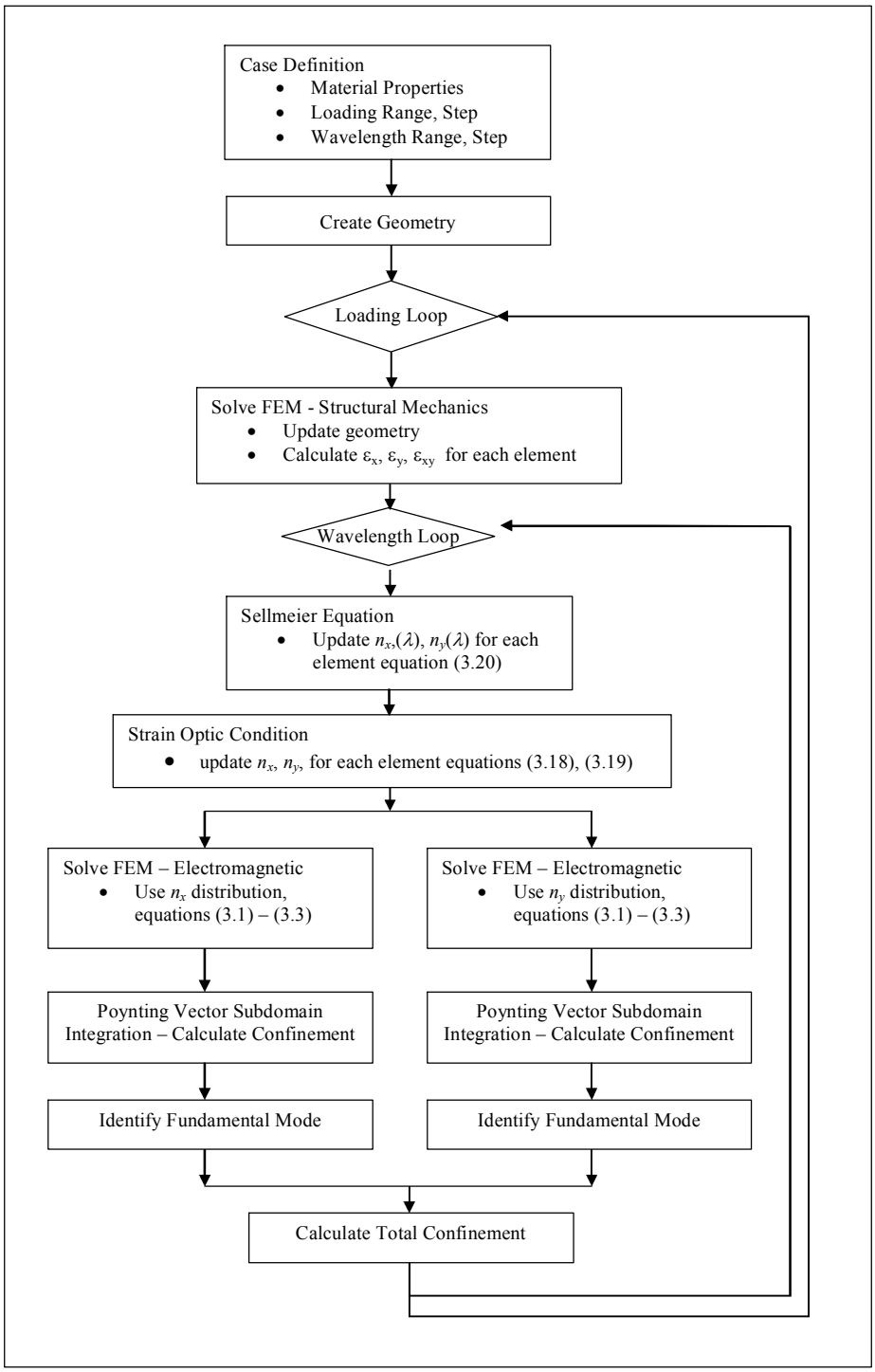

Figure 4-2: Flowchart of FEM Solution – Structural Mechanics and Electromagnetic.

4.1. Silica PBG Fiber

The first fiber studied was constructed of silica with material properties given in Table 3-2 and Table 3-3. The fiber was initially studied to locate the fundamental mode effective index

for the undeformed fiber. This was thus calculated to be n_{eff}=0.993294. The mode energy distribution was well confined with C=0.78. The energy distribution can be seen in Figure 4-3. The propagating wavelength was then varied over a spectral range to evaluate the bandwidth and center wavelength for the fundamental mode. This was accomplished by a Matlab script interfaced with Comsol Multiphysics to cycle through the solutions while varying the free space wavelength and searching for confined modes. For each simulation, the fundamental mode was identified by the confinement condition outlined in chapter 3. The fiber shown in Figure 3-2 is not birefringent, therefore only one value of n_{eff} was found for each wavelength. The calculated core power confinement at each wavelength is plotted in Figure 4-4. One can observe that the mode bandwidth is 21nm (based on the two circled data points) centered around λ =1547.5. The obtained confinement was high, ranging from approximately 68% to 79% in the bandwidth.

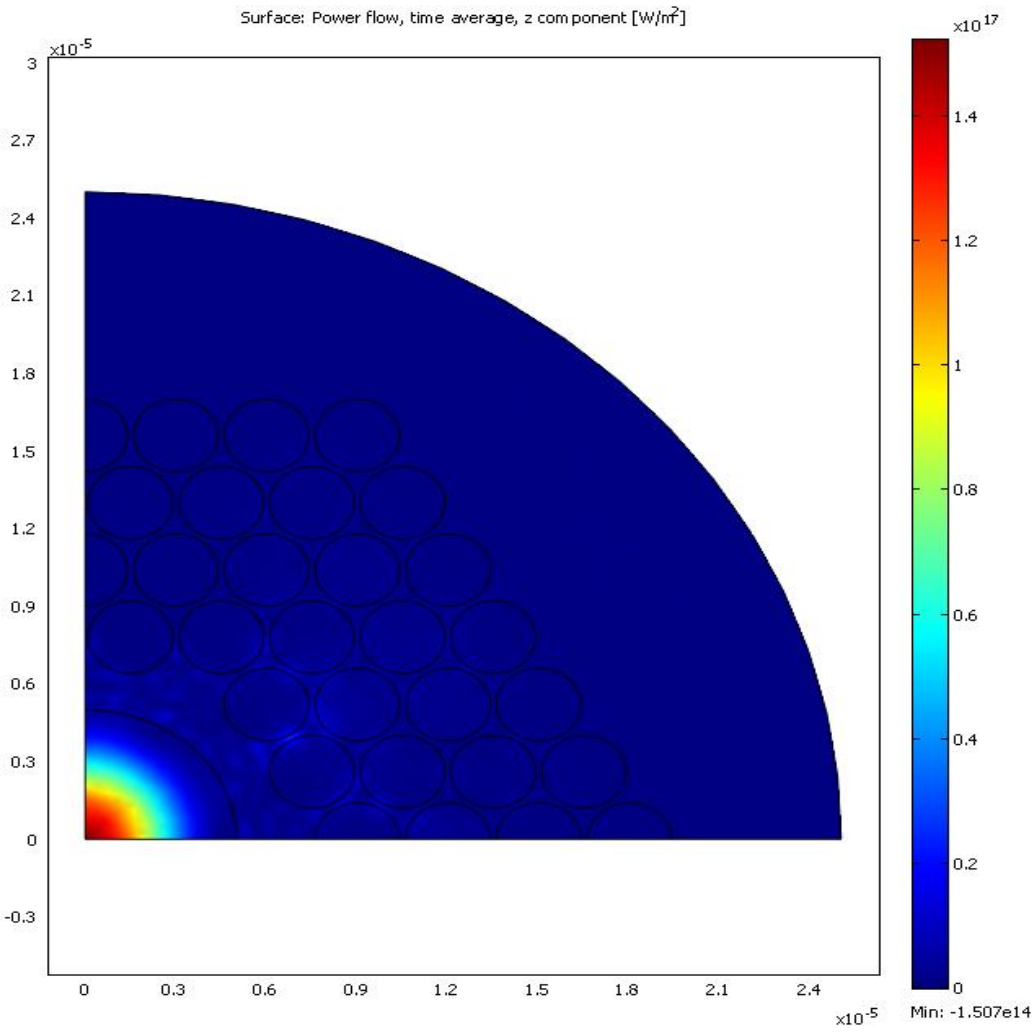

Figure 4-3: Fundamental Mode Confinement of Hansen Fiber.

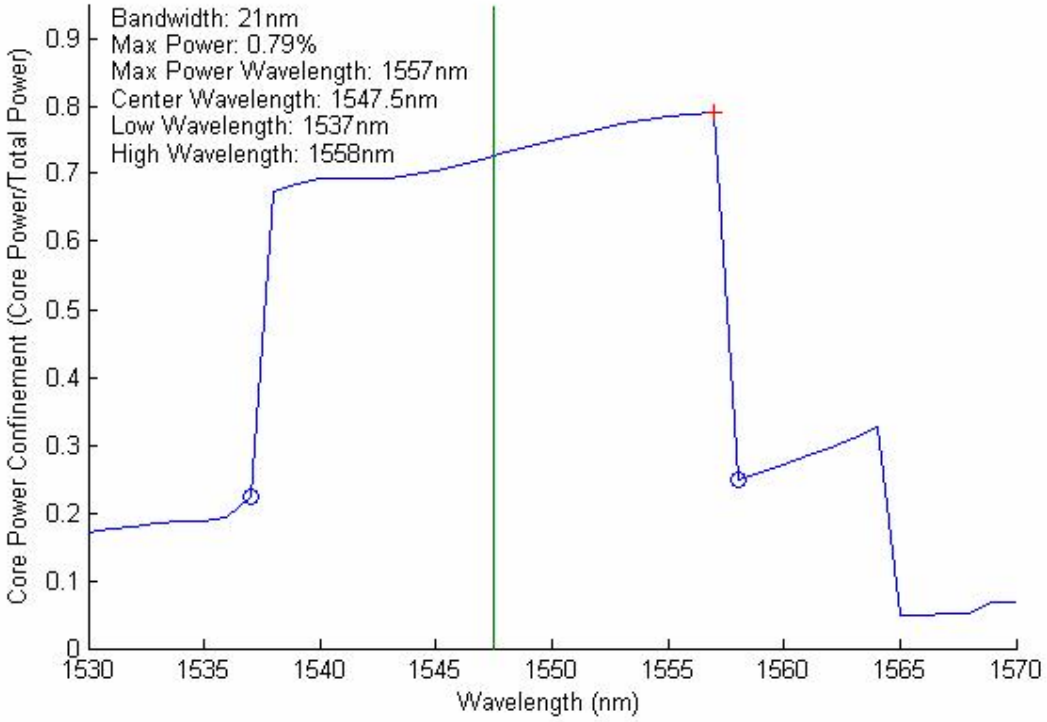

Figure 4-4: Spectral Scan of Silica Hansen Fiber, 1530nm-1570nm.

4.1.1. Mechanical Deformation

The fiber was studied for two loading cases. The first will be referred to as a crush load and was applied in the *y* direction. The second loading condition was an uniform pressure load applied perpendicular to the outer boundary of the optical fiber. In both cases load was applied until a maximum of approximately a 6% strain was obtained on the outer boundary of the fiber cross-section. This deformation is approximately the failure limit for pure silica, however in reality, the processed fiber would fail before this limit.

For the crush loading case the fiber cross-section was loaded as shown in Figure 4-5. The applied load was increased in increments of 1e8 Pa. Maximum deformation obtained for each load value is listed in Table 4-1. The maximum deformations occurred at the top center of the optical fiber, as denoted in Figure 4-5 by the dashed circle. This strain value calculated at this same point is also listed in Table 4-1. The deformation of the optical fiber for each loading case is shown in Figure 4-6. These figures are drawn to scale, therefore one can see that the holes have been extremely distorted by the final loading case. The effect of this distribution will appear in the confinement calculations later on.

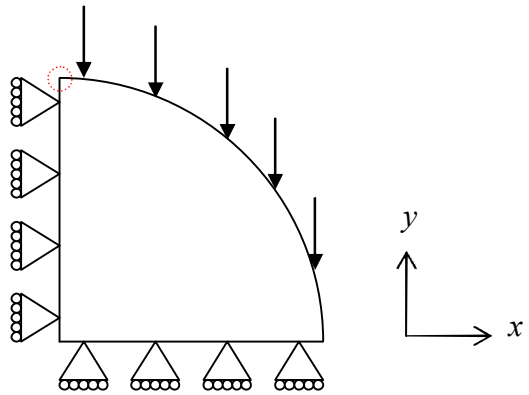

Figure 4-5: Fiber Crush Mechanical Loading Diagram.

Table 4-1: Loads, Deformations and Strains for Silica Crush Loading Cases

Load (Pa)	Deformation (m) (u_y)	Strain (ε_y)
1.00E+08	4.25E-07	1.7%
2.00E+08	8.50E-07	3.4%
3.00E+08	1.28E-06	5.1%
4.00E+08	1.70E-06	6.8%

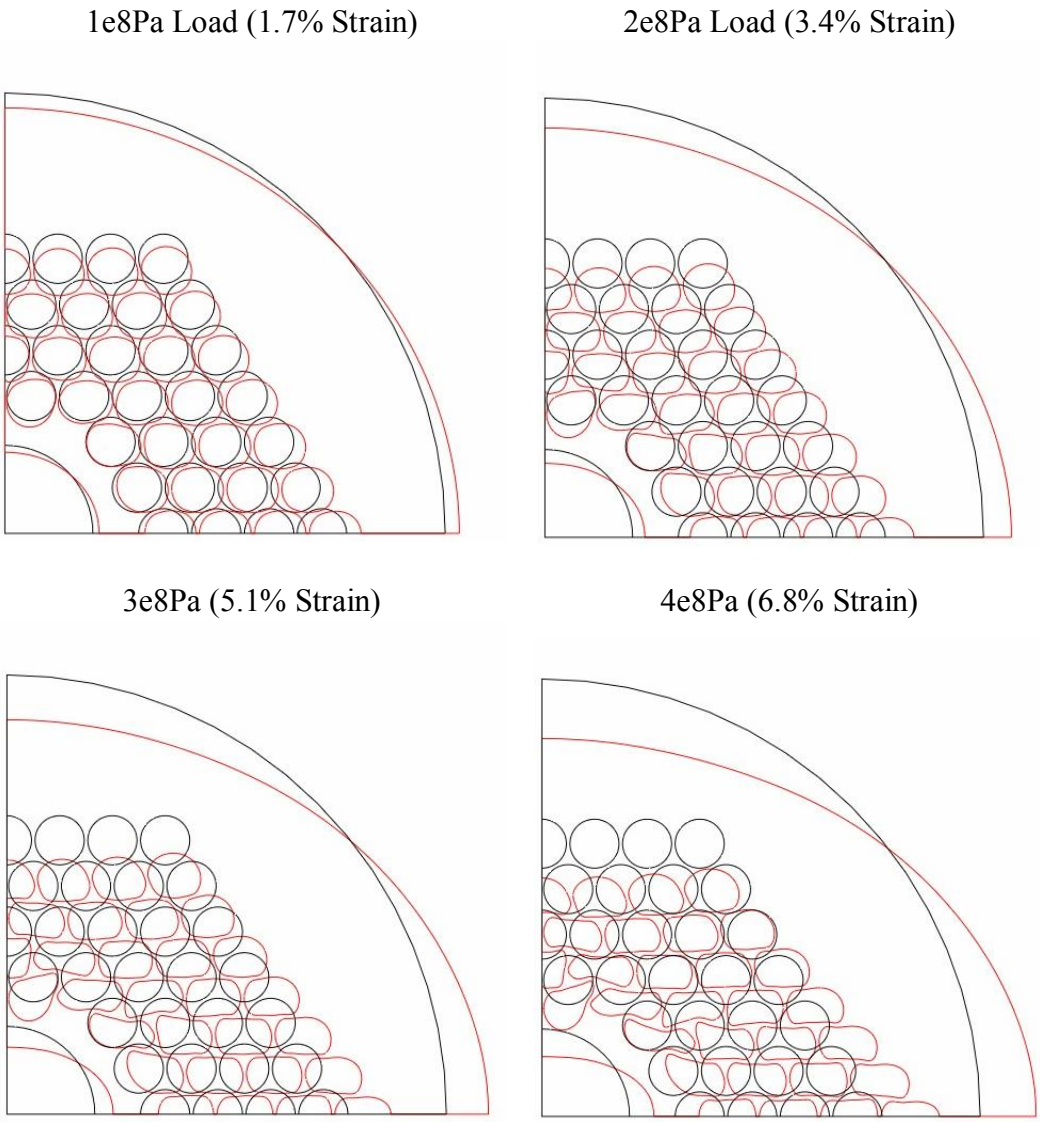

Figure 4-6: Deformations of Silica Fiber Crush Loading, Fiber Boundary Strains 0%, 1.7%, 3.4%, 5.1%, and 6.8%.

The strain was monitored at the outer boundary of the fiber since this would be where the optical fiber sensor is bonded to the external host material. However the internal hole boundaries in the geometry may have higher strain values than the outer boundary of the fiber. Therefore, the deformation may surpass the elastic limit of silica for the higher loading cases. As will be seen in later sections a material with an higher elastic and ultimate strain limits may be used. Guided mode solutions of geometries with these higher deformation

cases are useful as a separate study to look for confinement trends, independent of specific mechanical limits of a material.

Next the fiber was loaded with a uniform pressure load as shown in Figure 4-7. For this loading case, the load was increased in increments of 5e8 Pa. The deformation and strain values obtained at the top center of the model, denoted in Figure 4-7 by the dashed circle, are listed in Table 4-2. The deformation of the optical fiber for the various load cases is shown in Figure 4-8 once again to scale.

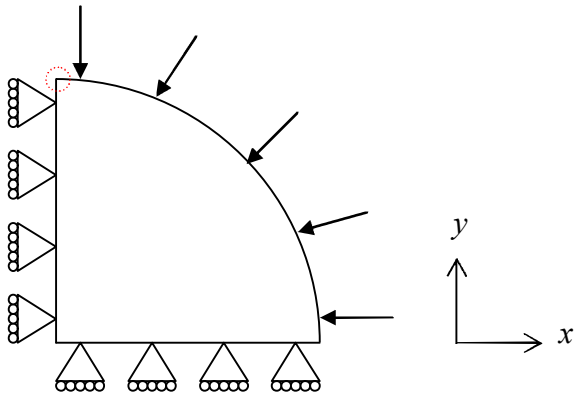

Figure 4-7: Fiber Uniform Pressure Mechanical Loading Diagram.

Table 4-2: Silica Fiber Pressure Loads, Deformations and Strains

Load (Pa)	Deformation (m) (u_y)	Strain (ε_y)
5.00E+08	4.00E-07	1.6%
1.00E+09	8.00E-07	3.2%
1.50E+09	1.20E-06	4.8%
2.00E+09	1.60E-06	6.4%

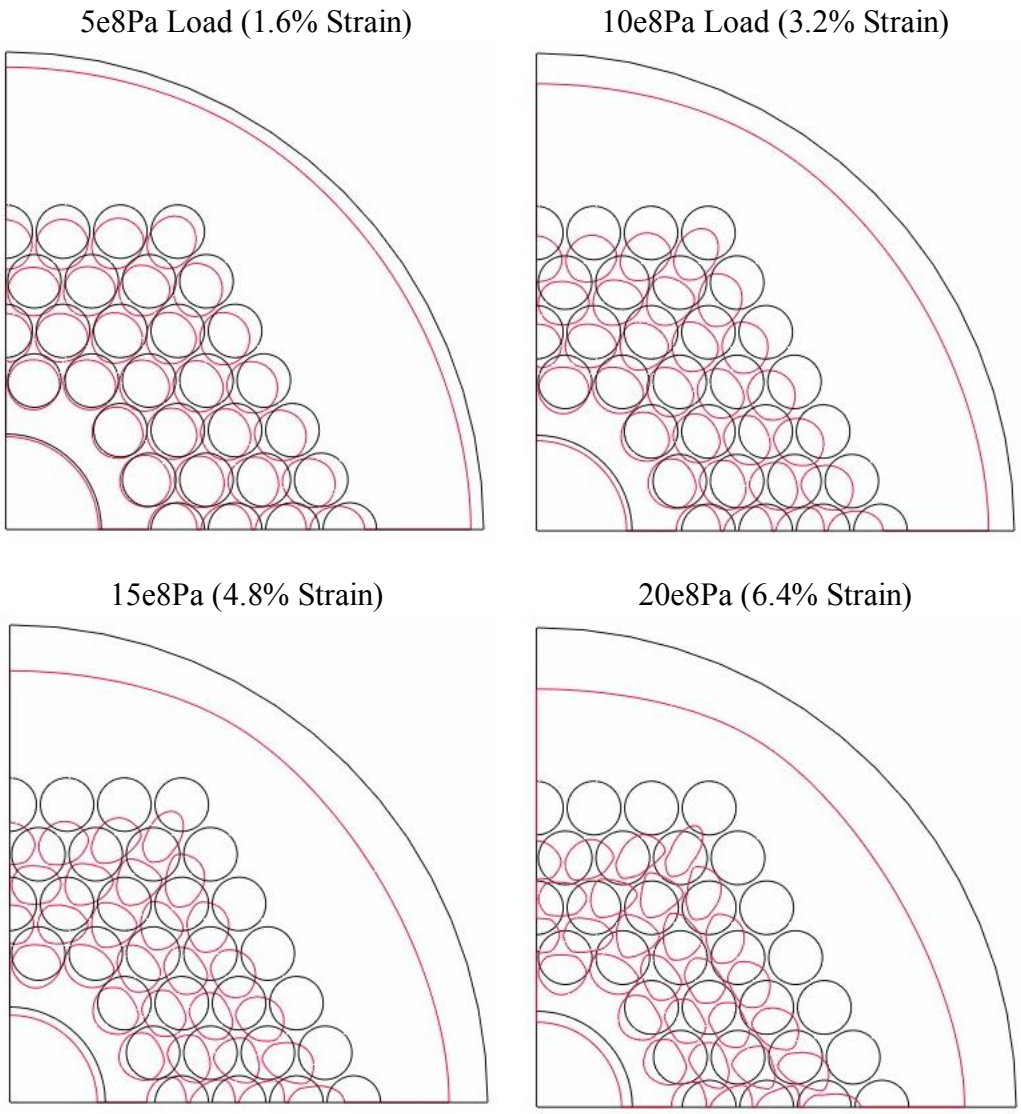

Figure 4-8: Pressure Loading Silica Fiber Deformations, , Fiber Boundary Strains 0%, 1.6%, 3.2%, 4.8%, and 6.4%.

As with the previous loading case, the holes are extremely distorted for the final loading case. Similar to the crush loading case the strain at a specific hole within the geometry may be higher than the elastic limit of silica, however general trends can still be observed. For this reason the analysis of guided mode solutions is valuable at these higher strain values. Finally, it is important to observe that although the pressure loading does not vary around the optical fiber, the fiber geometry itself is not rotationally symmetric, therefore the resulting deformation is also not rotationally symmetric.

4.1.2. Results – Crush Loading

Using the crush loading condition detailed in section 4.1.1 each deformed geometry and modified index of refraction distribution was analyzed for guided modes using a wavelength step of 1 nm, from 1530nm to 1570nm. A total of twelve solutions were found at each wavelength step. Using the guidelines detailed in section 3.3 for confinement based selection of valid guided modes, the fundamental mode was identified from the solution set for each wavelength and tracked across the spectrum around the bandgap.

At each load level, the bandgap was calculated in four separate manners. To begin, the change in bandgap at each deformation stage is fundamentally formed by the geometric pattern of the holes that form the cladding structure. Therefore, to isolate the effects on the bandgap due to geometry a solution was computed without the strain-optic effect (still including material dispersion) (Figure 4-9). For standard step-index fibers, the role of change in geometry is negligible as compared to the strain-optic effect for transverse loading and is therefore typically not included in fiber optic sensor modeling. Therefore, the purpose of calculating the geometrical effect separately is to demonstrate that the same assumption cannot be applied for PBG fibers. The second two cases looked at the index of refraction in the x and y axes independently incorporating the strain-optic effect in addition to material dispersion (Figure 4-10 and Figure 4-11). These were obtained using the calculated n_x and n_y indices of refraction, since these are the resulting principle axes for the fiber after deformation. Experimentally these confinements may be obtained by monitoring the two polarization states independently if desired.

Finally, a fourth case where the bandgap is computed from the combined effect of the x and y polarization states (Figure 4-12). This output would represent what a single intensity measurement of the optical fiber output would record over the spectrum. This solution is computed from the previous n_x and n_y solutions by adding the power distributions where it is assumed that the optical input power was split evenly between the optical axes.

Considering only the geometric deformations, one observes that the increasing load results in a slight increase in bandgap bandwidth for the optical fiber. The more noticeable change is

that the maximum confinement shifts from the upper wavelength edge of the bandgap to the lower edge. This demonstrates the importance of looking at the entire bandgap spectrum to make generalizations, rather than at a single wavelength value. The average confinement does not decrease significantly until an applied load of 4e8 Pa at which point the upper wavelengths begin to lose confinement. This was also the load value for which large deformations had occurred to the holes as seen in Figure 4-6. Similar trends are seen for the cases including the strain-optic effect seen in Figure 4-10 and Figure 4-12, except where the bandgap shape begins to reverse for the highest load of Figure 4-11 These plots are not identical due to the birefringence in the optical fiber after loading. As a final note, the geometrical changes contribute to the majority of the change in confinement and therefore are not negligible for PBG fibers.

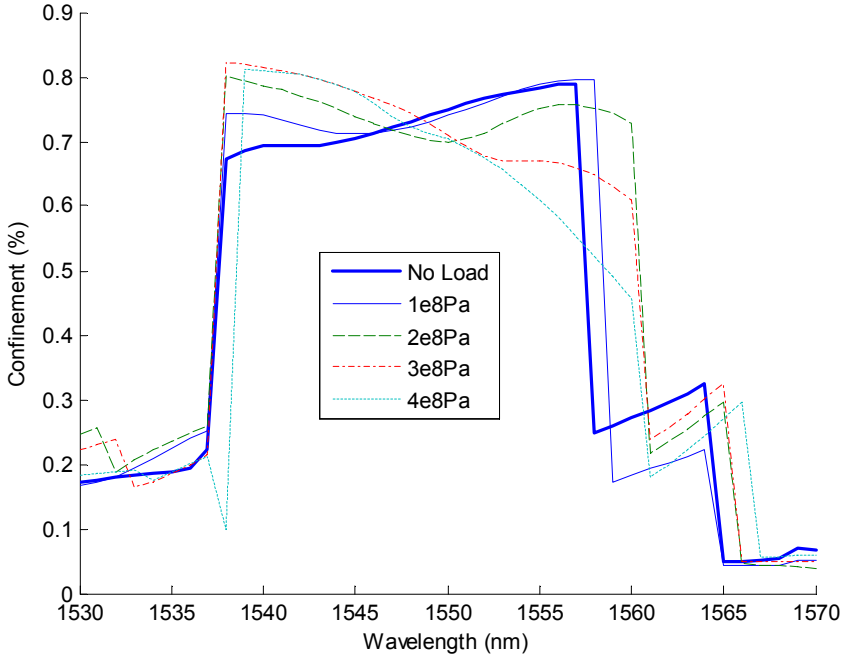

Figure 4-9: Silica Crush Load Spectral Confinement due to Geometric Deformation, Fiber Boundary Strains 0%, 1.7%, 3.4%, 5.1%, and 6.8%.

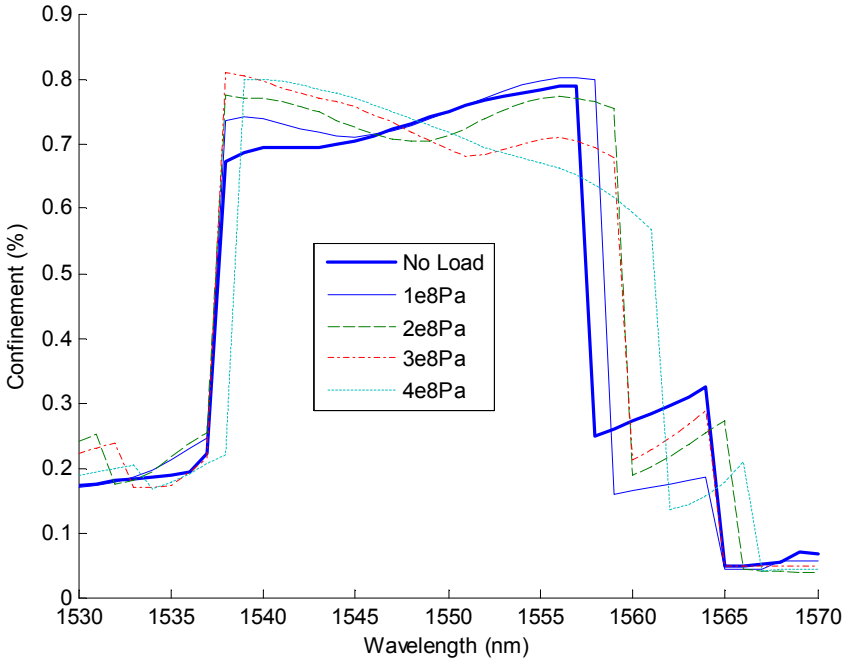

Figure 4-10: Silica Crush Load Spectral Confinement n_x Strain-optic Effect, Fiber Boundary Strains 0%, 1.7%, 3.4%, 5.1%, and 6.8%.

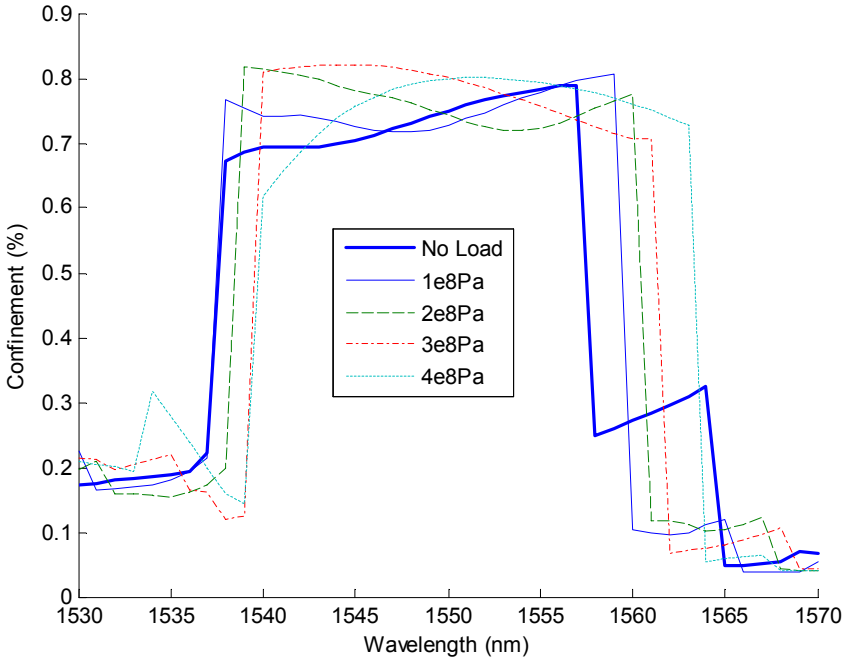

Figure 4-11: Silica Crush Load Spectral Confinement n_y Strain-optic Effect, Fiber Boundary Strains 0%, 1.7%, 3.4%, 5.1%, and 6.8%.

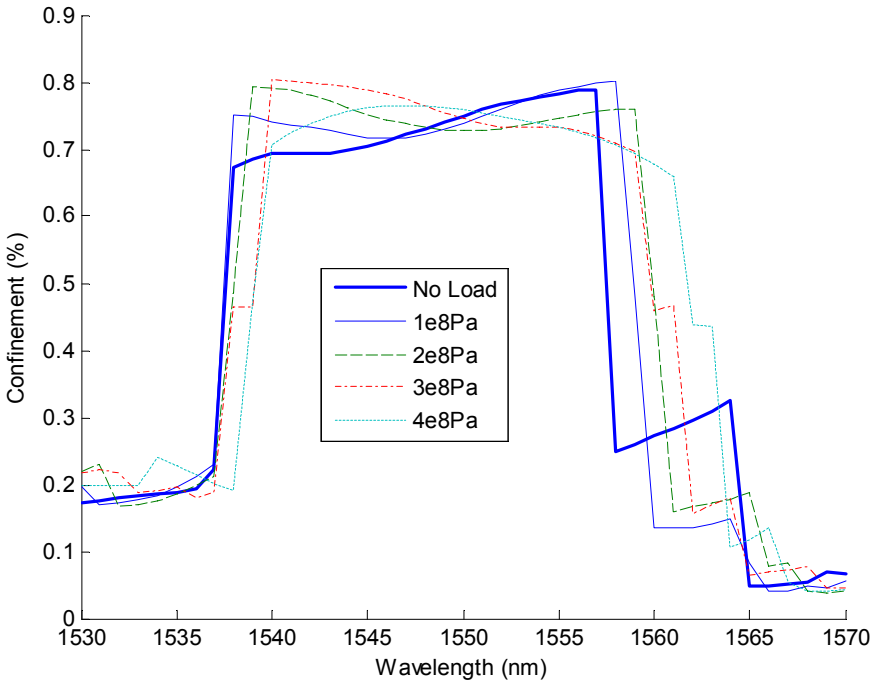

Figure 4-12: Silica Crush Load Spectral Confinement Combined Strain-optic Effect, Fiber Boundary Strains 0%, 1.7%, 3.4%, 5.1%, and 6.8%.

Figure 4-13 examines the highest loading case and plots the bandgap change for the *x* and *y* directions to highlight the birefringence. This property is particularly avoided in most applications for optical fiber, but in sensing this may give information about the state of loading. By monitoring the intensity of each polarization state at a particular wavelength the information about the strain on each axis may be obtained.

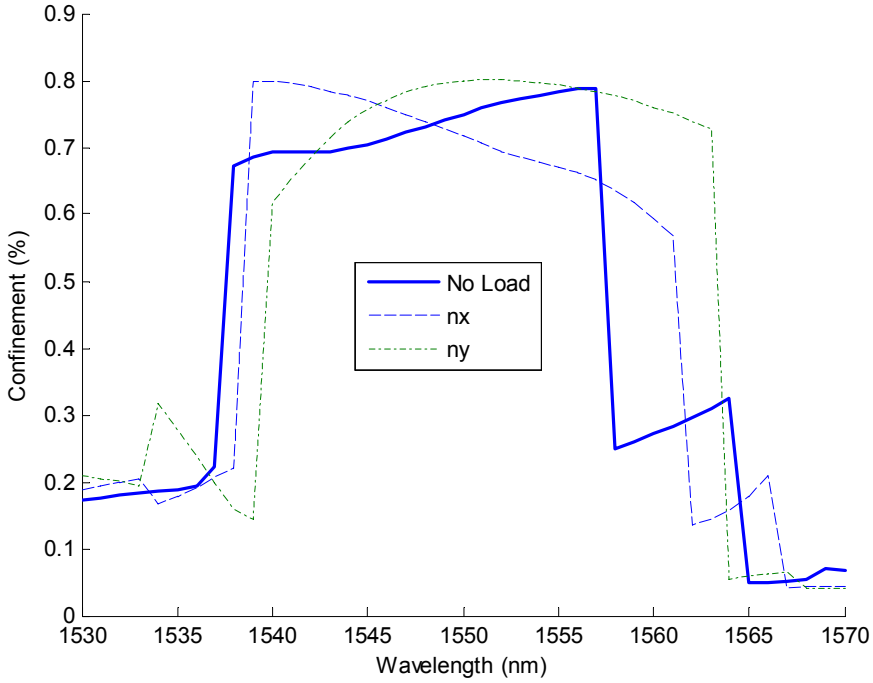

Figure 4-13: 4e8Pa Crush Load, 6.8% Strain, Silica Fiber with n_x and n_y Indices of Refraction.

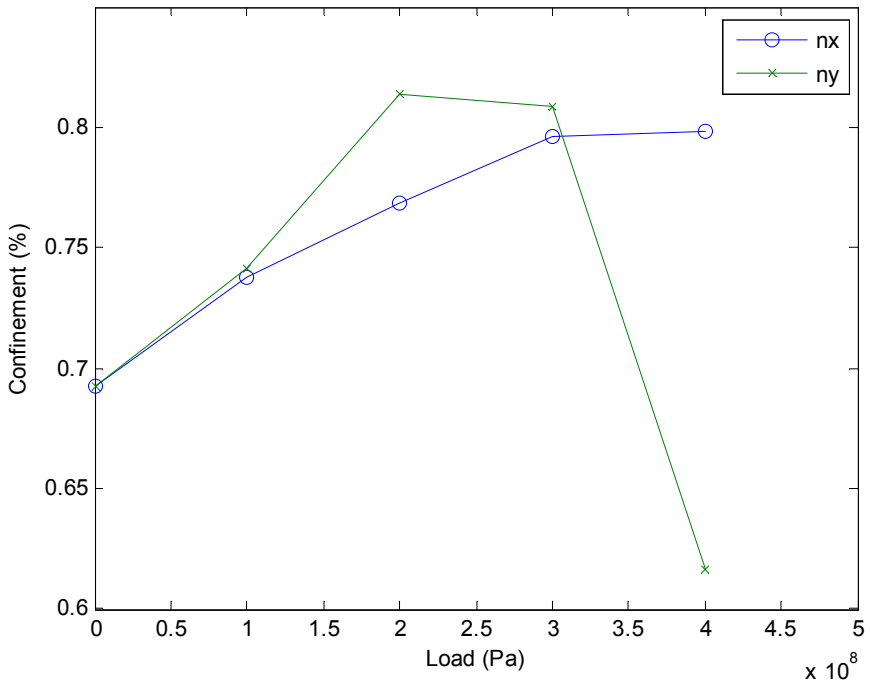

Figure 4-14: Silica Fiber 1540nm Index of Refraction Change with Crush Load, Boundary Strains 0%, 1.7%, 3.4%, 5.1%, and 6.8%.

4.1.3. Results – Pressure Loading

Using the uniform pressure loading condition detailed in section 4.1.1 and modified index of refraction distribution the fiber was analyzed for guided modes. The steps, as in the crush case, were 1nm from 1530nm to 1570nm. A total of twelve modes were found at each wavelength in each of four cases. The bandgap was determined solely due to geometry (still including material dispersion), on each principal axis using the index of refraction, n_x and n_y, and finally the bandgap was calculated for the combined confinement from both axes. The details of mode selection and confinement calculations are detailed in section 4.1.2.

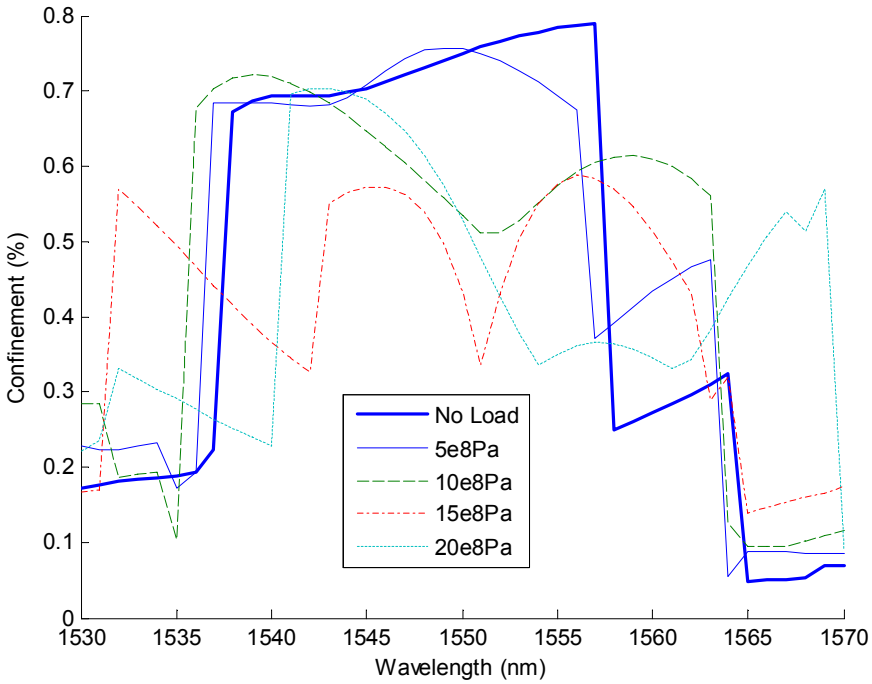

Figure 4-15: Silica Pressure Load Spectral Confinement due to Geometric Deformation, Fiber Boundary Strains 0%, 1.6%, 3.2%, 4.8%, and 6.4%.

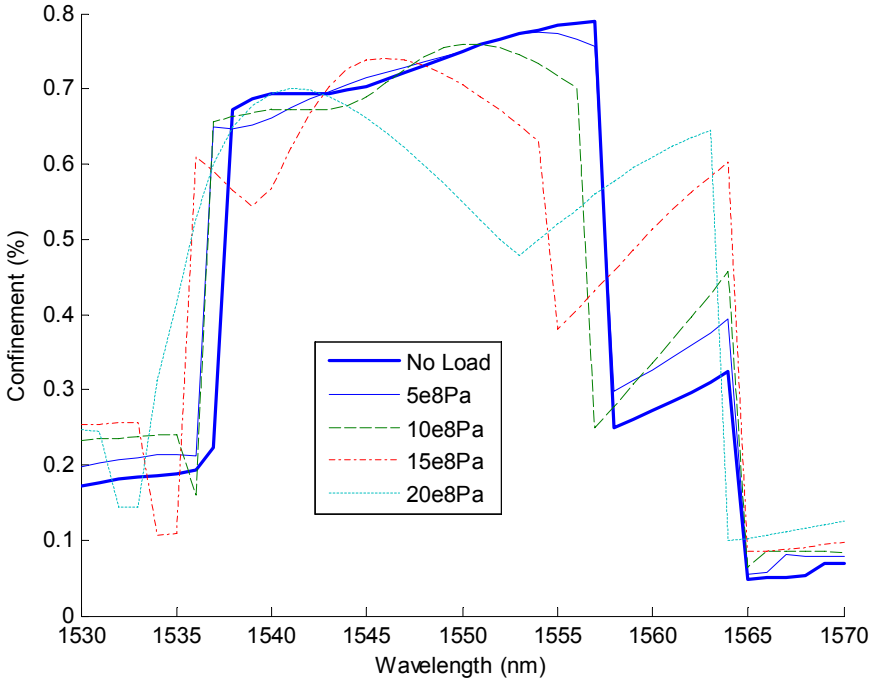

Figure 4-16: Silica Pressure Load Spectral Confinement n_x Strain-optic Effect, Fiber Boundary Strains 0%, 1.6%, 3.2%, 4.8%, and 6.4%.

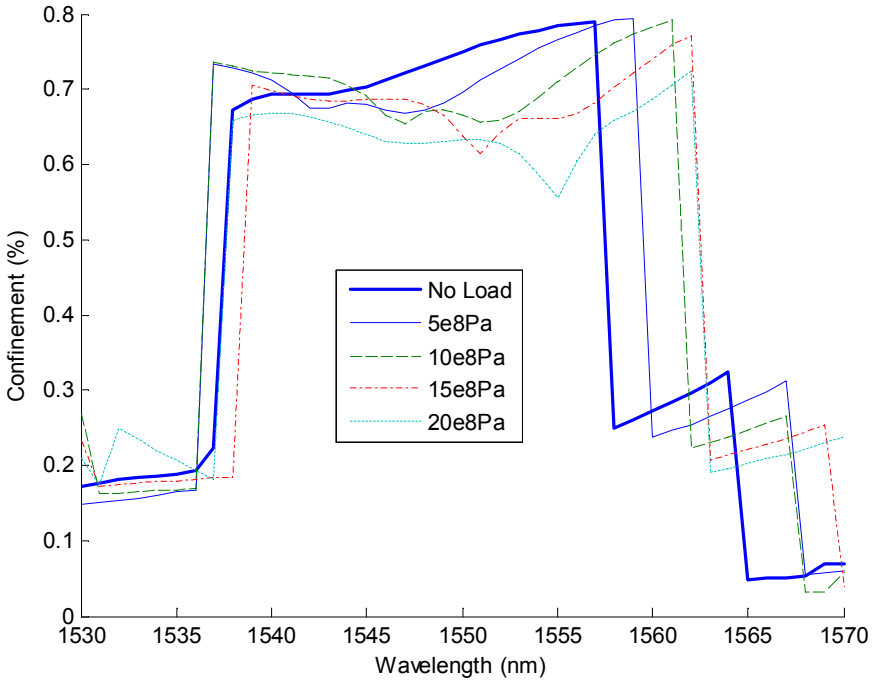

Figure 4-17: Silica Pressure Load Spectral Confinement n_y Strain-optic Effect, Fiber Boundary Strains 0%, 1.6%, 3.2%, 4.8%, and 6.4%.

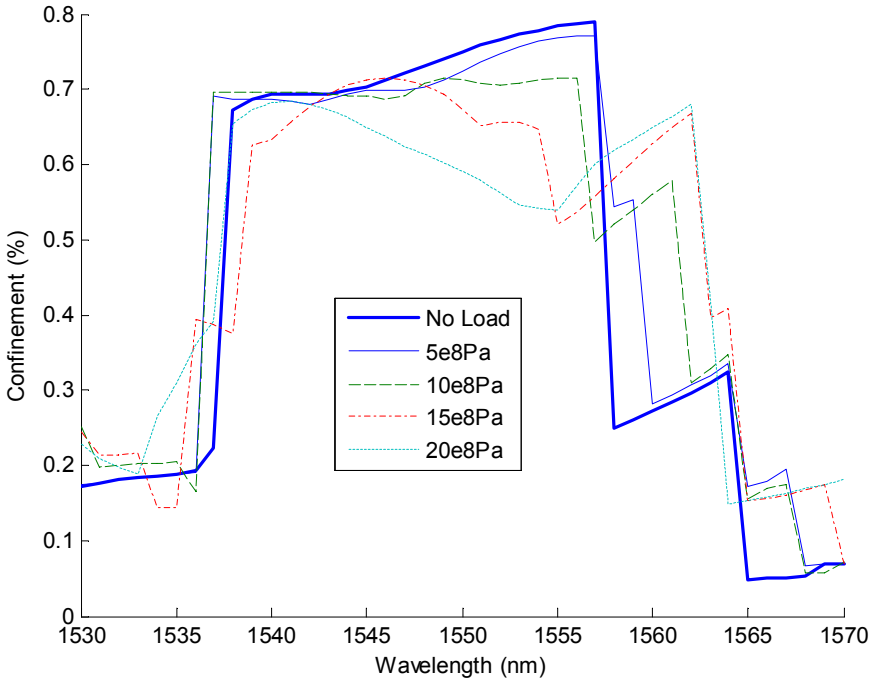

Figure 4-18: Silica Pressure Load Spectral Confinement Combined Strain-optic Effect, Fiber Boundary Strains 0%, 1.6%, 3.2%, 4.8%, and 6.4%.

Figure 4-15 suggests that only using the geometric deformation for modeling the effects of loading is not accurate. The trends in this plot do not correspond with the following plots taking into account the strain-optic effect. This differs from the output from the silica cases where the geometric effect was similar to the cases with the strain-optic effect. Intuition predicts that the results from the *x* and *y* axis polarization studies represented in Figure 4-16 and Figure 4-17 would be identical for this loading condition. For this particular fiber design however the fiber geometry is not rotationally symmetric. This causes the results to differ on each axis.

The index of refraction on each axis is generated from the *x*, *y*, and shear strains as given by equations (3.16) and (3.17). Figure 4-19 illustrates the difference between the strain on the *x* and *y* axis.

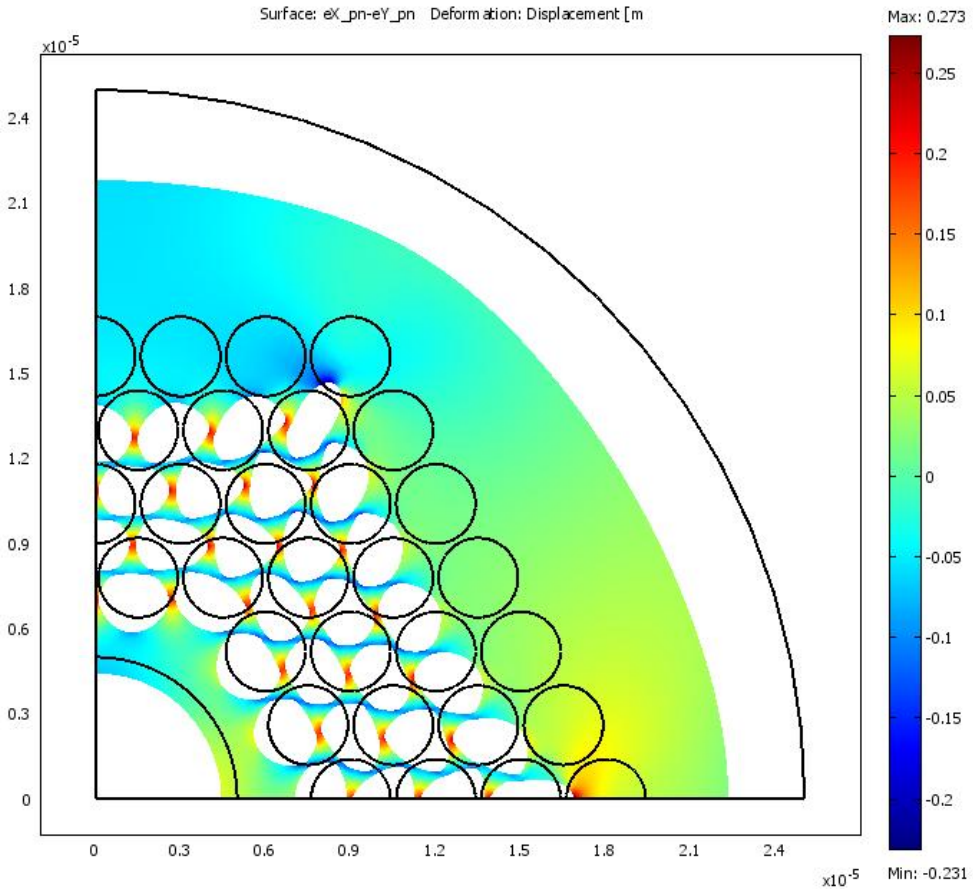

Figure 4-19: Silica Fiber 20e8 Pa Pressure Loading - ε_x- ε_y.

The results for the highest loading case 20e8 Pa is shown in Figure 4-20. It is clear that the results from examining the *x* and *y* polarizations are not identical.

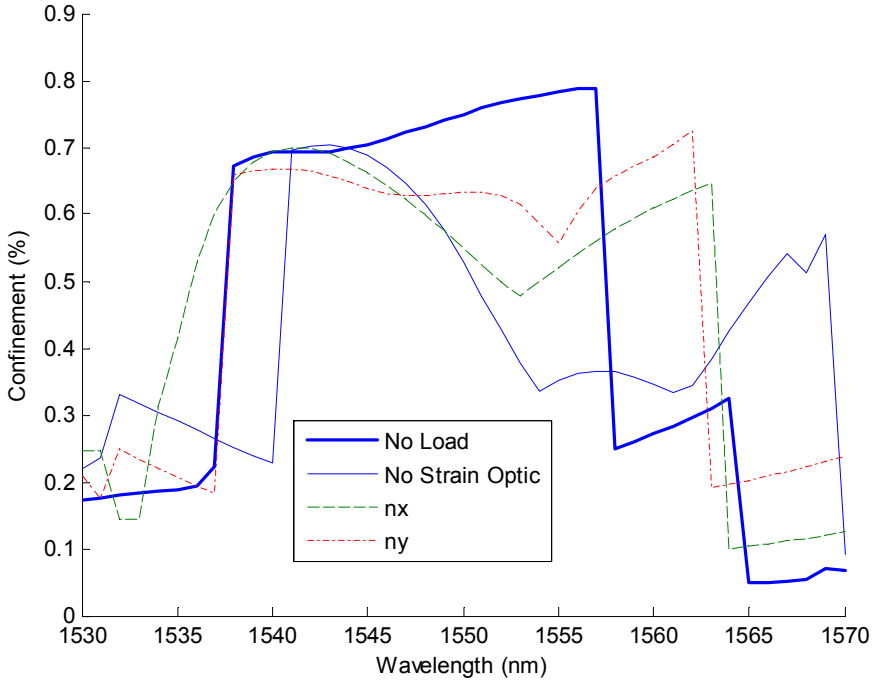

Figure 4-20: 20e8Pa Pressure Load Silica – No Strain Optic, n_x and n_y Indices of Refraction.

Figure 4-21 examines the change in confinement with loading at 1552nm. This wavelength was chosen due to the best resolution across loading ranges for both polarizations. This information combined with the results from the silica crush loading case demonstrates that with proper calibration a sensor may be used to determine load axis information.

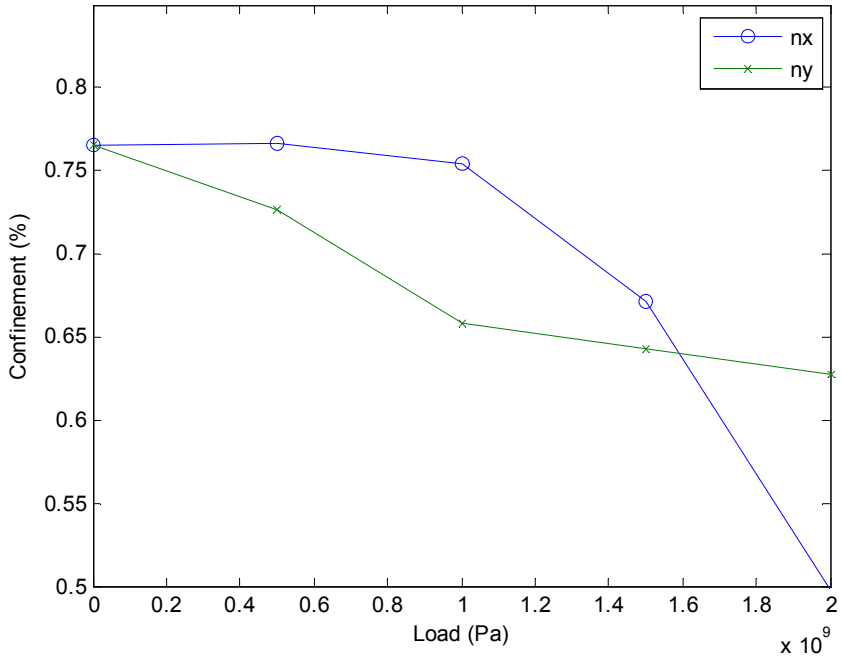

Figure 4-21: Silica Fiber 1540nm Index of Refraction Change with Pressure Load, Fiber Boundary Strains 0%, 1.6%, 3.2%, 4.8%, and 6.4%.

4.2. Polymer PBG Fiber

The loads required to generate measurable strain in the silica fiber may be higher than desired for some applications. With this in mind the Hansen fiber design was also studied for the polymer PMMA with a lower modulus of elasticity an index of refraction of 1.492. The spectral response for the undeformed fiber was computed and as seen from this plot this fiber design may not be optimal for this index of refraction, but for this study the band gap is sufficient to study the trends discovered studying the silica fiber.

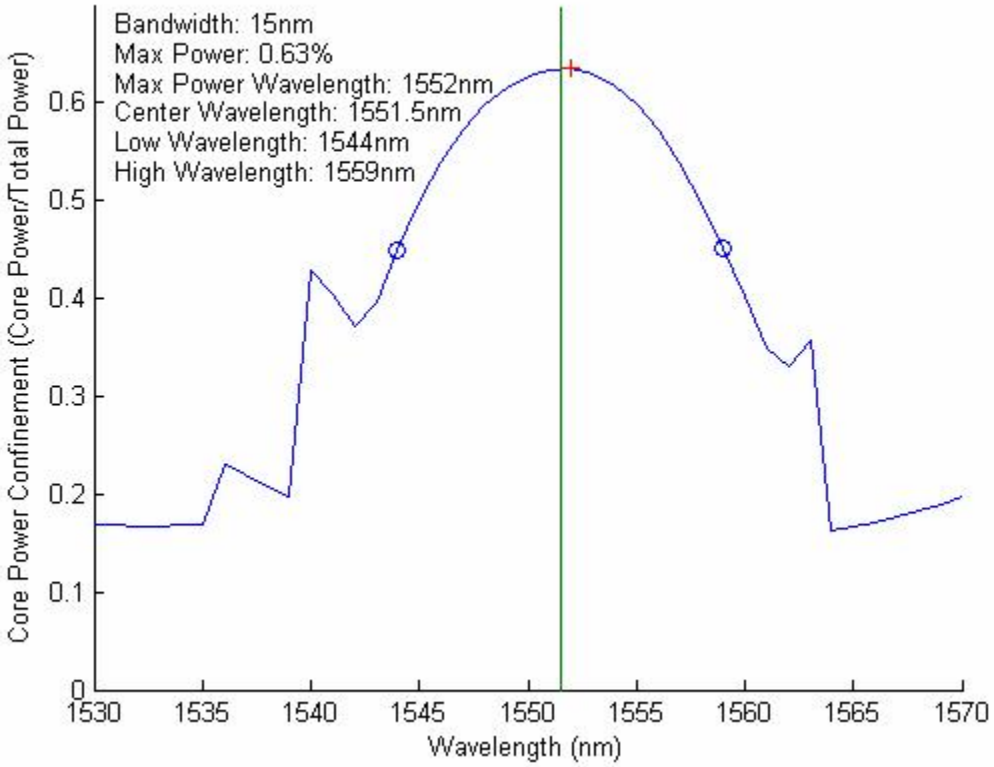

Figure 4-22: No Load Spectral Response of PMMA-Theoretical Hansen Fiber, 1530nm – 1570nm.

4.2.1. Mechanical Deformation

Strains up to 5.8% were studied for the PMMA fibers under crush load. The loads were adjusted to account for the lower material modulus to achieve these results. The overall maximum strains in the crush and the pressure cases for PMMA is slightly lower than for the silica cases, but this was purely an artifact of the loading steps used. As mentioned earlier the ultimate strain of PMMA is much higher than that of silica and may be deformed much further. For comparison all strain values were kept approximately 6%. The details of the mechanical loading were described in section 4.1.1. Table 4-3 lists the deformations and strains for the crush loading starting with a loading 1e07 Pa in steps of 2e8 Pa. For the uniform pressure loading of the PMMA fibers a strain up to 5.9% was studied. The loading ranged from 2e7 Pa in steps of 2e7 Pa. Table 4-4 lists the deformations and strains for the uniform pressure loading condition.

Table 4-3: PMMA-Theoretical Crush Loads, Deformations and Strains

Load (Pa)	Deformation (m) (u_y)	Strain (ε_y)
1.00E+07	9.09E-07	3.6%
1.20E+07	1.09E-06	4.4%
1.40E+07	1.27E-06	5.1%
1.60E+07	1.45E-06	5.8%

Table 4-4: PMMA-Theoretical Pressure Loads, Deformations and Strains

Load (Pa)	Deformation (m) (u_y)	Strain (ε_y)
2.00E+07	2.97E-07	1.2%
4.00E+07	5.94E-07	2.4%
6.00E+07	8.90E-07	3.6%
8.00E+07	1.19E-06	4.7%
1.00E+08	1.48E-06	5.9%

4.2.2. Results – Crush Loading

Using the crush loading condition detailed in section 4.2.1 each deformed geometry and modified index of refraction distribution was analyzed using the parameters and techniques detailed in section 4.1.2 for geometric deformation alone, using n_x and n_y, and finally the combined index of refraction.

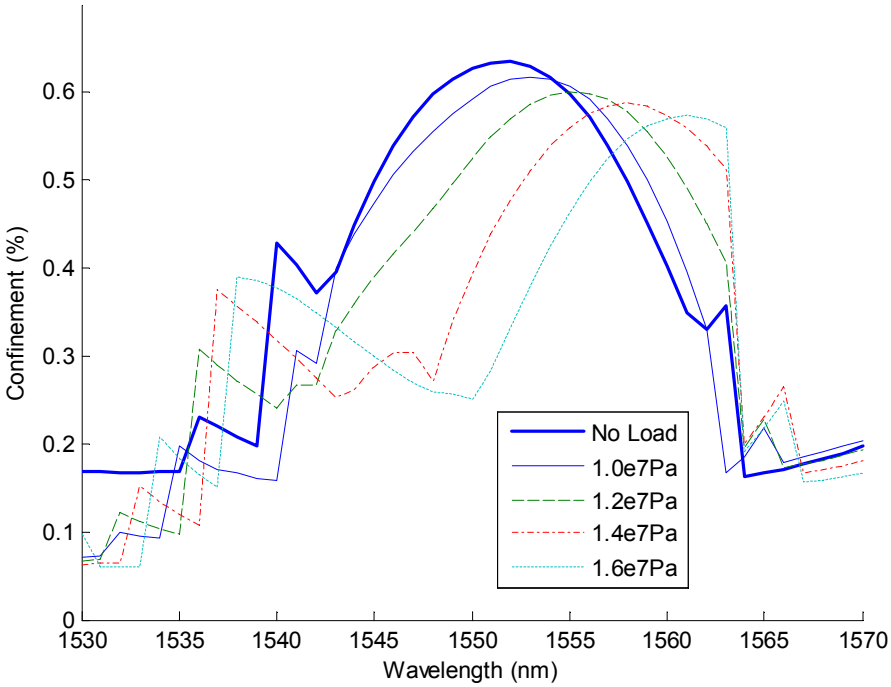

Figure 4-23: PMMA-Theoretical Crush Load Spectral Confinement due to Geometric Deformation, Fiber Boundary Strains 0%, 3.6%, 4.4%, 5.1%, and 5.8%.

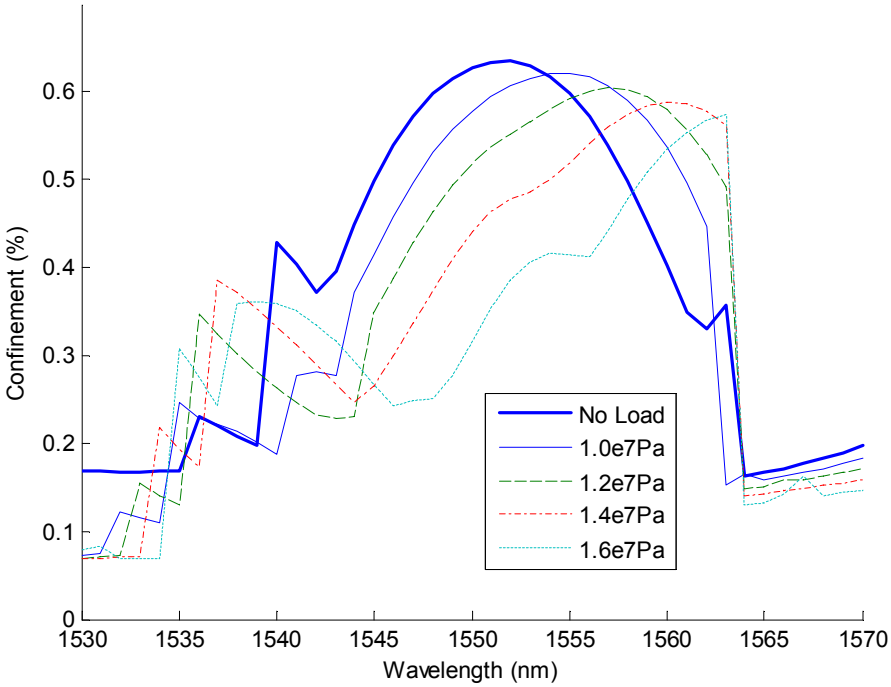

Figure 4-24: PMMA-Theoretical Crush Load Spectral Confinement n_x Strain-optic Effect, Fiber Boundary Strains 0%, 3.6%, 4.4%, 5.1%, and 5.8%.

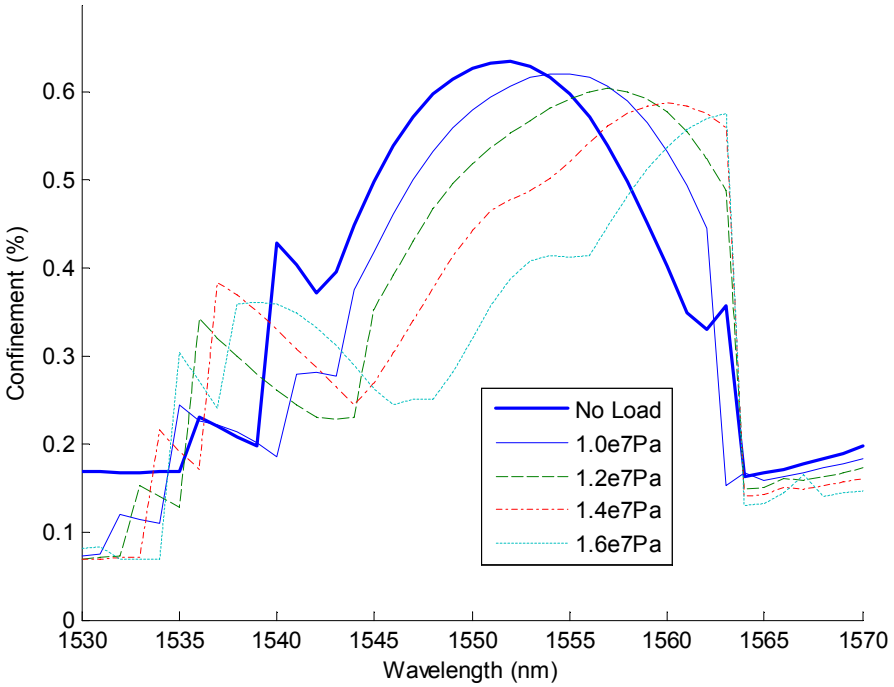

Figure 4-25: PMMA-Theoretical Crush Load Spectral Confinement n_y Strain-optic Effect, Fiber Boundary Strains 0%, 3.6%, 4.4%, 5.1%, and 5.8%.

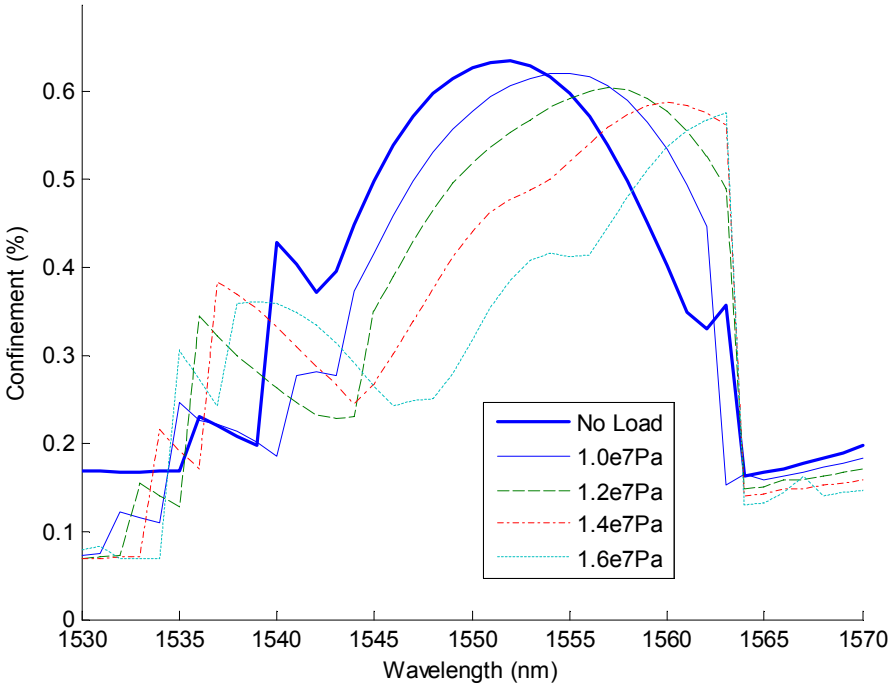

Figure 4-26: PMMA-Theoretical Crush Load Spectral Confinement Combined Strain-optic Effect, Fiber Boundary Strains 0%, 3.6%, 4.4%, 5.1%, and 5.8%.

The output of this case demonstrates the effect of the Pockel's constants on the analysis. Displayed in Figure 4-24 and Figure 4-25 are indistinguishable bandgap characteristics. This was due to the p_{11} and p_{12} of PMMA being very similar, 0.3 and 0.297 respectively. In looking at the highest level of loading, 1.6e7 Pa for the difference between n_x and n_y, it can be seen from Figure 4-27 that the birefringence is very small even at the larges load level as expected from equations (3.16) and (3.17). The PMMA-Theoretical material under the 5.8% strain loading condition resulted in a maximum birefringence of 8.2e-4. By comparison the silica crush case under a 6.8% strain loading condition resulted in a birefringence two order of magnitudes higher at 6.6e-2. The very low birefringence in the case of PMMA-Theoretical makes birefringence information difficult to obtain.

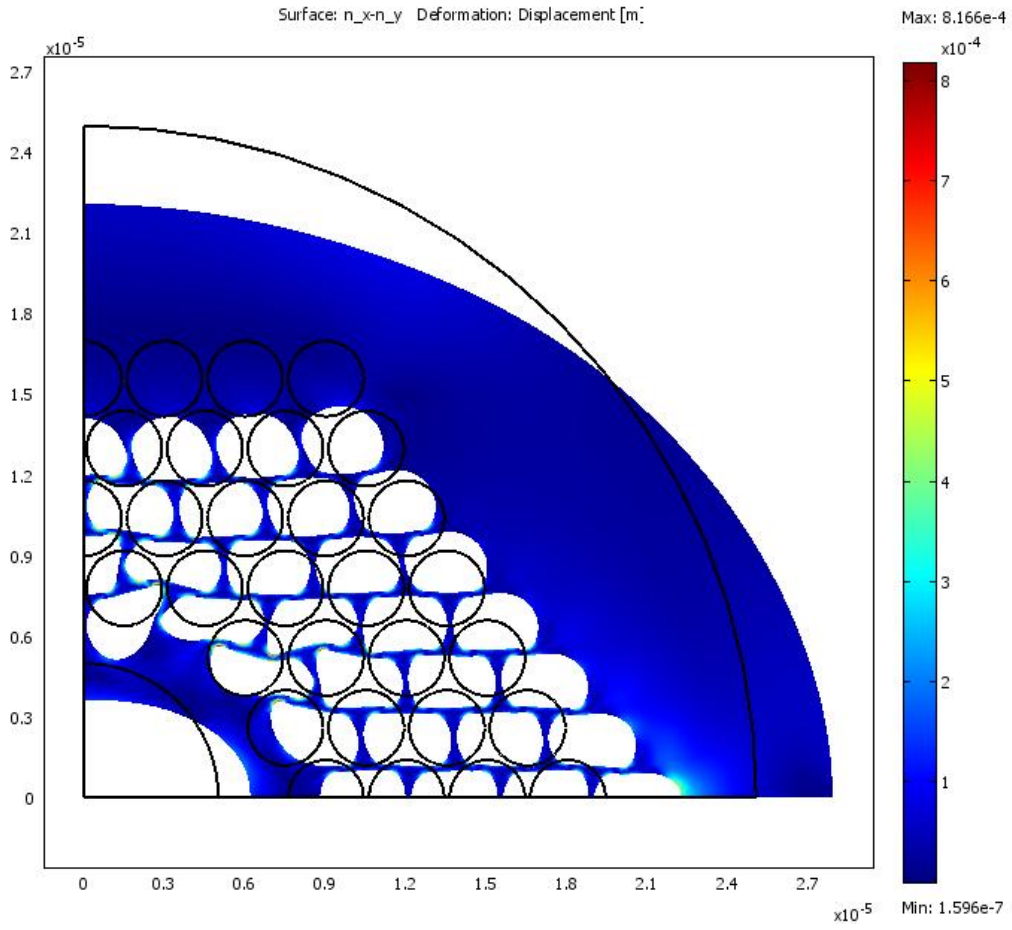

Figure 4-27: Birefringence at 1.6e7 Pa Loading, 1550nm.

A pure intensity measurement which would result from the combined strain-optic effect may give meaningful results. Figure 4-28 illustrates the change in confinement over the load range studied at 1550nm and shows promising results. If the Pockel's constants were adjusted through doping of the material then individual loading information from n_x and n_y may be obtained as well.

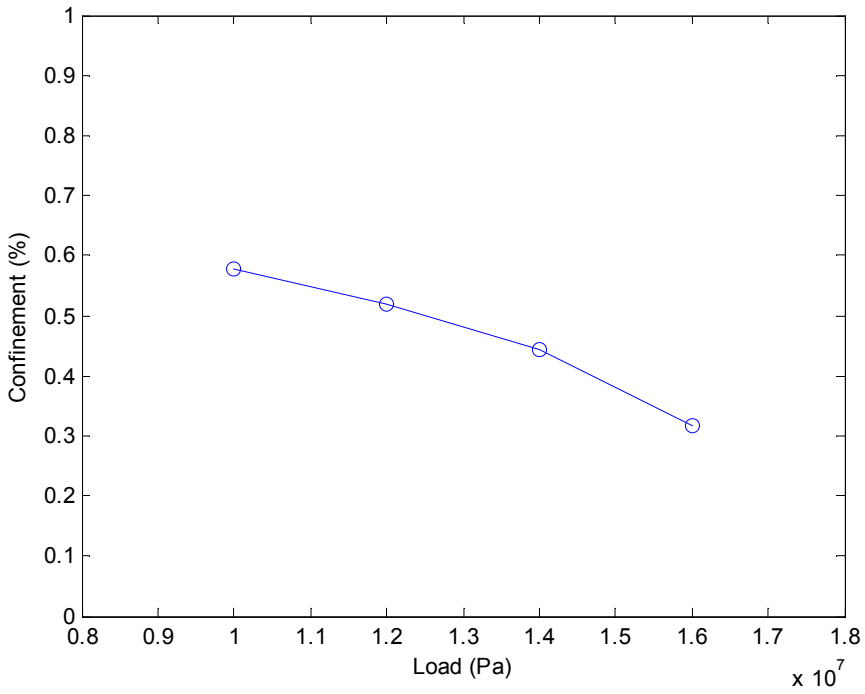

Figure 4-28: PMMA-Theoretical Crush Confinement Versus Loading, 1550nm, Fiber Boundary Strains 0%, 3.6%, 4.4%, 5.1%, and 5.8%

4.2.3. Results – Pressure Loading

Using the crush loading condition detailed in section 4.2.1 each deformed geometry and modified index of refraction distribution was analyzed using the parameters and techniques detailed in section 4.1.3 for geometric deformation alone, using n_x and n_y, and finally the combined confinement resulting from both axes.

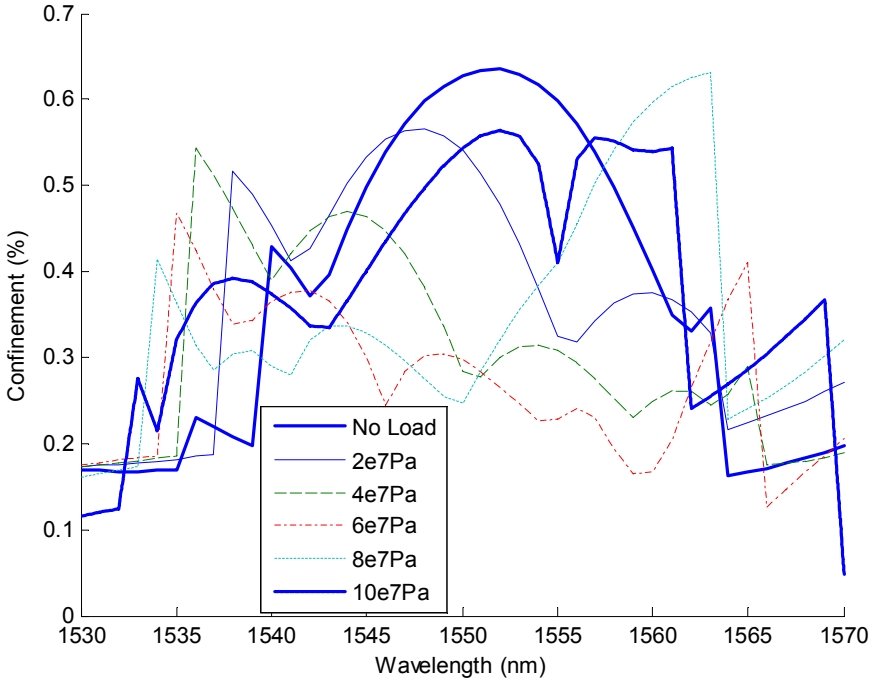

Figure 4-29: PMMA-Theoretical Pressure Load Spectral Confinement due to Geometric Deformation, Fiber Boundary Strains 0%, 1.2%, 2.4%, 3.6%, 4.7%, and 5.9%.

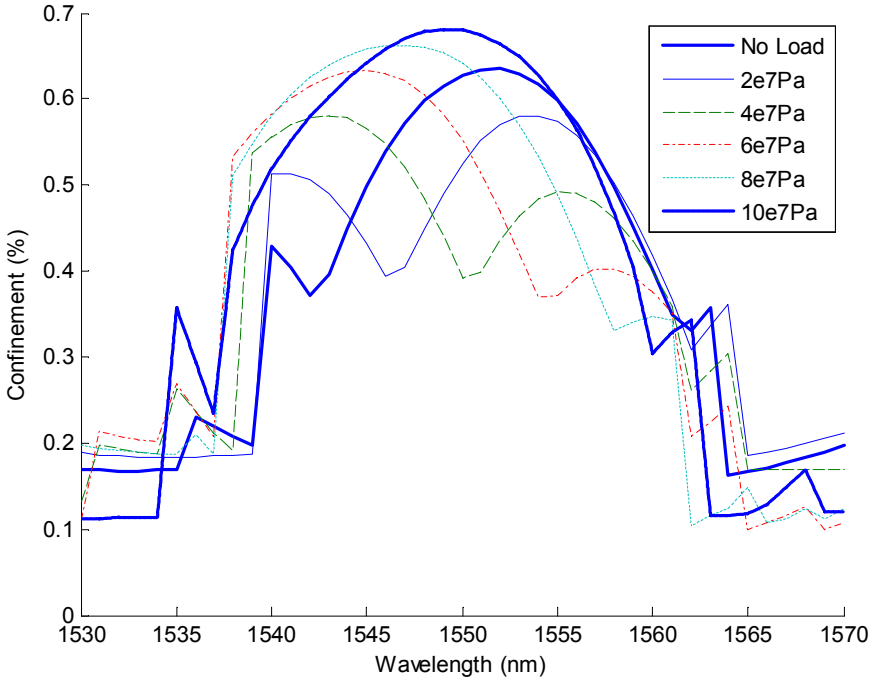

Figure 4-30: PMMA-Theoretical Pressure Load Spectral Confinement n_x Strain-optic Effect, Fiber Boundary Strains 0%, 1.2%, 2.4%, 3.6%, 4.7%, and 5.9%.

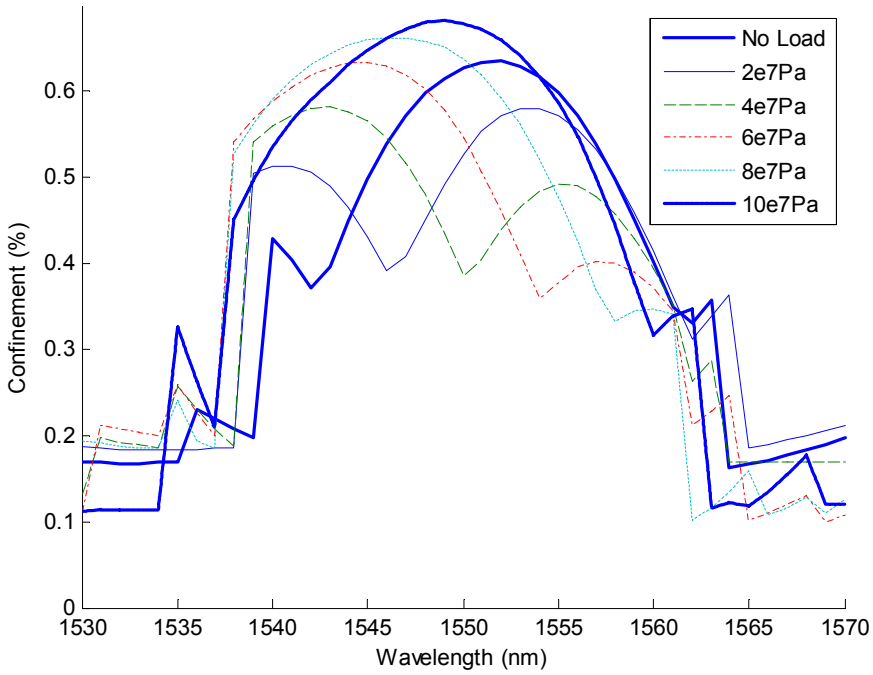

Figure 4-31: PMMA-Theoretical Pressure Load Spectral Confinement n_y Strain-optic Effect, Fiber Boundary Strains 0%, 1.2%, 2.4%, 3.6%, 4.7%, and 5.9%.

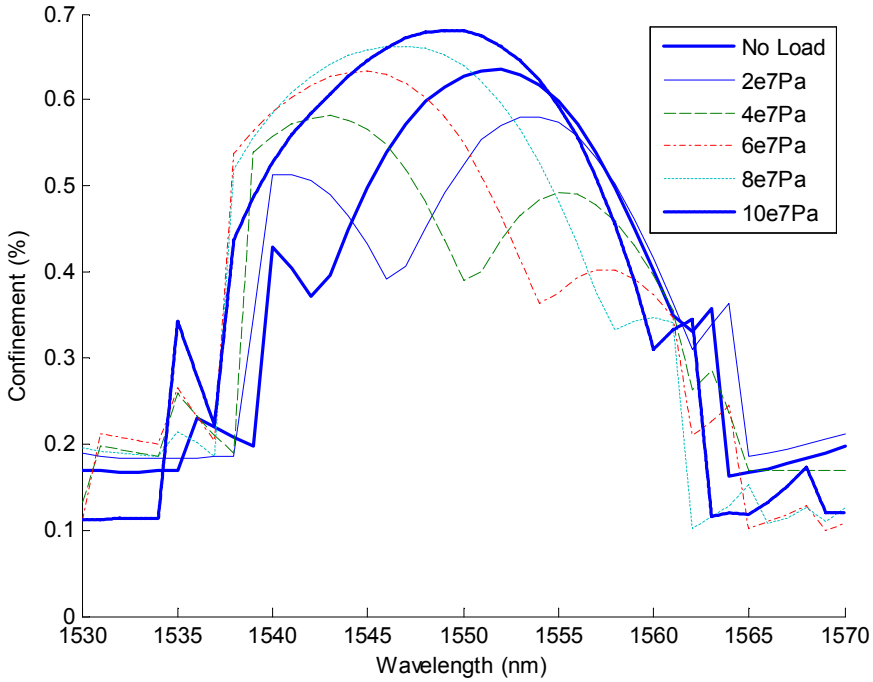

Figure 4-32: PMMA-Theoretical Pressure Load Spectral Confinement Combined Strain-optic Effect, Fiber Boundary Strains 0%, 1.2%, 2.4%, 3.6%, 4.7%, and 5.9%.

The earlier cases each demonstrated the importance of the strain-optic effect, but this case presents in greater detail the importance of this effect relative to the geometry change. The difference in response given in Figure 4-29 is in stark contrast to that in Figure 4-30, Figure 4-31, and Figure 4-32. Similar to the result from the PMMA crush case taking into account geometric deformation only (Figure 4-15) this demonstrates the importance of the Pockel's constants. Figure 4-29 and Figure 4-31 also reinforce the need for differing Pockel's constants to attain axis specific information.

A new finding came from the behavior of the bandgap through the load range after the 4e7 Pa loading condition. The confinement lowered as expected to this point, but for higher loadings the bandgap regained confinement and appeared to have shifted. To investigate, the individual Poynting power was examined at all modes for 1550nm at the 6e7 Pa loading condition.

What was discovered was that the combination of the geometry change and index of refraction change caused the power to shift to two guided modes. Shown in Figure 4-33 and Figure 4-34 is the Poynting power for two modes. With lower loads than 6e7 Pa there had only been one mode present. The confinement of what was the originally the fundamental mode had dropped to 10% and is represented in Figure 4-33, while the new mode formed represented in Figure 4-34 had a confinement of 68%.

This presents a new challenge in that the method of mode selection had relied on the fact that only one guided mode was present. If however two or more guided modes were present then the measured intensity would be the sum of all guided modes in an actual fiber from source to detector. It is the case in traditional TIR optical fiber that modes with a large portion of their power in the cladding tend to disperse after a short length of fiber, sometimes only a few meters, leaving only the fundamental mode. The guidance mechanism is the Bragg reflection for PBG fibers and not TIR and it is unknown if modes such as represented in Figure 4-33 would disperse or stay confined.

In either case, both modes arriving and summing or a single fundamental mode arriving would each present new challenges both in modeling and in actual detector construction. It is recommended that the design parameters and loading range set such to avoid this condition.

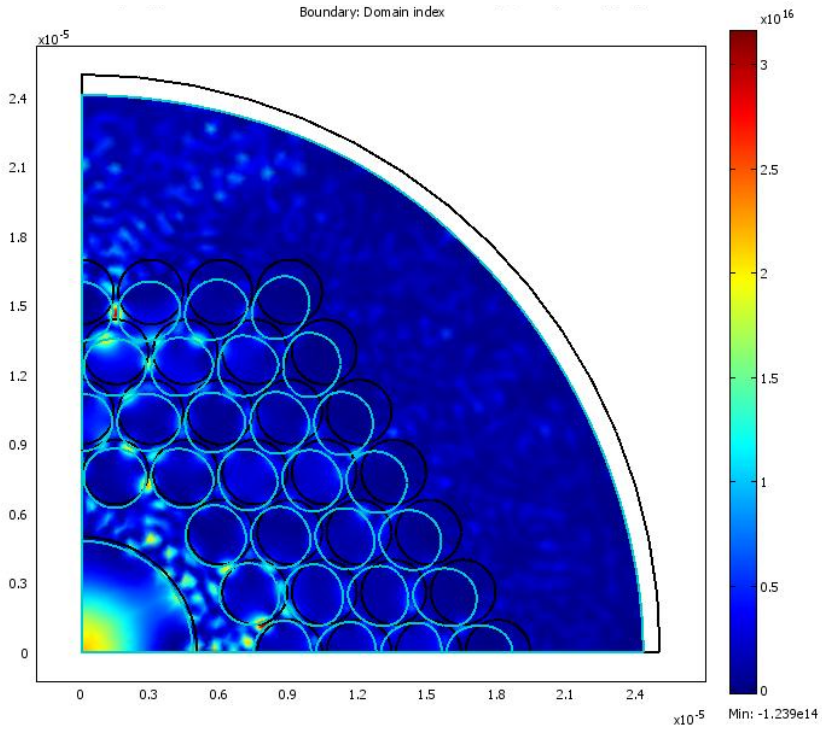

Figure 4-33: Poynting Power of PMMA-Theoretical at 6e7Pa Pressure Loading (n_x mode 0.993225 at 1550nm).

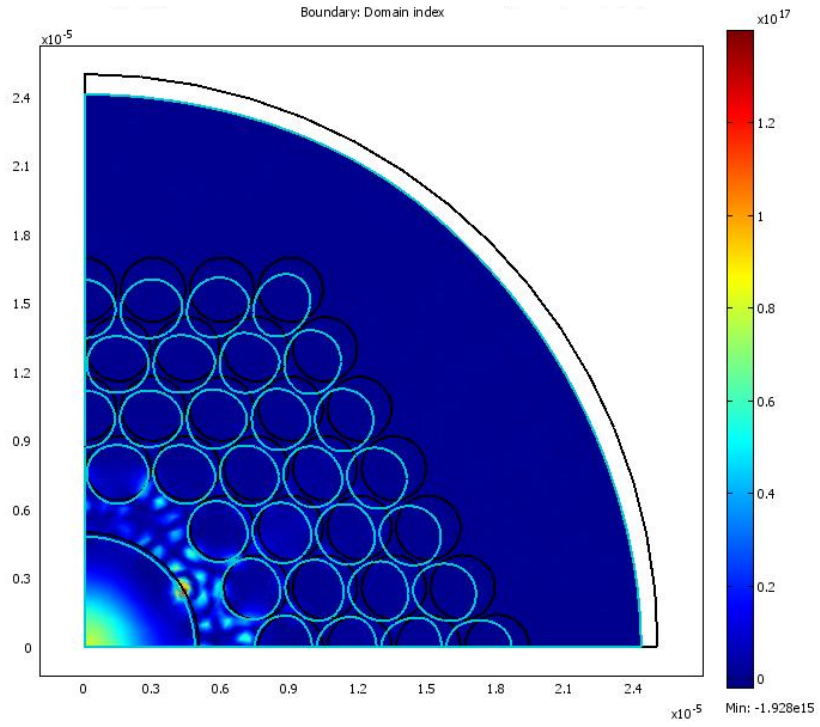

Figure 4-34: Poynting Power of PMMA-Theoretical at 6e7Pa Pressure Loading (n_x mode 0.991934 at 1550nm).

4.3. Summary

The study of both crush loads and uniform pressure loads on materials with different mechanical and optical characteristics were studied using loads that approached 6%. Each case yielded new insight into important guidelines that should be considered in the design of a sensor for transverse load sensing.

The study of the silica fiber in crush loading showed that useful information may be obtained from the confinement of each polarization state of light in the fiber. At higher strain values however the bandgap degraded and would require complex calibration to determine loading. This will require the optimization of optical properties of the fiber for the strain range sensed.

The silica uniform pressure case showed the impact of the absence of rotational symmetry of the fiber. Under uniform pressure load the response of the sensor was not equal through each

axis This may be used to an advantage if the proper calibrations were performed, but this must be taken into account.

The PMMA-Theoretical crush loading case demonstrated the importance of the Pockel's constants and the strain-optic effect in determining a guided mode solution. The extent of the importance of the strain-optic effect relative to geometric deformation was not known at the onset of this research. It was discovered that the strain-optic effect plays a large role in determining the sensor response and it is recommended that the normal and shear Pockel's constants should differ by approximately 50% or more as was the case with silica to obtain axis specific loading information. This appeared to be of a higher order effect than the cladding hole geometry deformation alone.

Finally the PMMA-Theoretical uniform pressure load case confirmed the importance of the strain-optic effect and Pockel's constants, but introduced a possible hindrance to sensor response. If the loading conditions and optical properties of the sensor are not carefully chosen then multiple guided modes may be present. This causes difficulty in modeling and in implementation of the sensor.

CHAPTER V

Conclusions and Recommendations for Future Work

In summary, sensing technologies exist to measure transverse strain, but each has drawbacks that may be avoided with a new class of optical fiber. The focus of this research was to determine if the new class of optical fiber with guidance through the Bragg reflection resulting in a photonic bandgap effect exhibited desirable properties for transverse strain sensing. For the study of deformation and its impact on guidance the FEM method was chosen since established analytic methods were not suited to arbitrary geometry changes.

The FEM method was verified for a published fiber design against known solutions using established methods. The FEM method was then applied to both silica and a theoretically doped PMMA fiber in both a crush and uniform pressure loading conditions using loads that would approach 6% deformation on the boundary of the fiber.

The result of the each modeling case yielded insight into the design of PBG fibers both from a geometry and material standpoint. The silica fibers exhibited advantages from optical properties while the PMMA material's lower modulus and yield strains would allow for measuring lower loads through a larger strain regime.

Common to both designs was the realization that the geometry of the holes constructing the cladding play a role in the sensor response. This effect was shown through the strains that ultimately affected the index of refraction through the strain-optic effect than the effect from cladding hole geometry deformation.

Finally it was determined that in a circumstance where the optical, mechanical and loading conditions are in certain proportion a undesired effect of mode shifting can occur. While this phenomena caused difficulty in modeling it is unknown to what extent it would effect actual sensor implementation.

The current study was performed on a theoretical fiber that was suited for study with the FEM. The currently manufactured PBG fibers often have more rings, indicating higher confinement, and a cross section that more closely approaches rotationally symmetric. While these fibers have been designed specifically for telecommunications applications they may hold promise for transverse sensors. It would be of value to experimentally determine if the currently available fibers are candidates for current sensing applications.

In addition to investigating silica base PBG fibers, while not currently commercially available, a PBG PMMA air-core based fiber would also have value in that the transmission loss should be much lower than a solid core design. This would allow these fibers to be used in longer lengths in addition to their lower modulus and higher yield strains than those of silica based fiber. If birefringence information is desired it would require investigation into manufacturing the fibers with a relative Pockel's constant difference of 50% or greater. Designs with non-circular core structures have been shown to show birefringence and this may compensate for the lack of difference in the strain-optic characteristics as well (Saitoh and Koshiba, 2002). Modeling this type of fiber would be of value in that it may succeed in achieving a design of a sensor that has the very desirable characteristics of low optical loss, high strain tolerance, multi-axis sensitivity and may be interrogated with single wavelength measurements. In addition PMMA fibers may be manufactured using an extrusion process rather than a preform-drawing process as in silica fiber. This gives both more flexibility in fiber construction and may allow for lower cost, longer length sensing fiber.

REFERENCES

1. Argyros, A., van Eijkelenborg, M., Large, M., Bassett, I. "Hollow-core Microstructured Polymer Optical Fiber." *Optics Letters*. Vol. 31, No. 2 (January 2006)

2. Berenger, J., "A perfectly matched layer for the absorption of electromagnetic waves". *Journal of Computational Physics* Vol. 114 (1994) 185–200.

3. Birks, T., Robers, P., Russell, P., Atkin, D., Shepherd, T., "Full 2-D photonic bandgaps in silica/air structures." *Electronic Letters.* Vol. 31, No. 22 (October 1995) 1941-1943.

4. Bjarklev, A., Broeng, J., Bjarklev, A., Photonic Crystal Fibres. Kluwer Academic Publishers, Boston, MA. (2003)

5. Department of Electrical & Computer Engineering, Brigham Young University, Fiber Bragg Gratings Tutorial, http://www.ee.byu.edu/photonics/fbg.phtml, (2004)

6. Broeng, J., Barkou, S., Søndergaard, T., Bjarklev, A., "Analysis of air-guiding photonic bandgap fibers." *Optics Letters*. Vol. 25, No. 2 (2000) 96-98.

7. Chehura, E., Skordos, A., Ye, C., James, S., Partridge, I., Tatam, R., "Strain development in curing epoxy and glass fibre/epoxy composites monitored by fibre Bragg grating sensors in birefringent optical fibre." *Smart Materials and Structures*. Vol. 14, No. 2. (2005) 354-362.

8. Optics Group, 2007, CVI Melles Griot, Product Information, Rochester, New York

9. Cregan, R., Mangan, B., Knight, J., Birks, T., Russell, P., Roberts, P., Allan, D., "Single-Mode Photonic Band Gap Guidance of Light in Air." *Science*. Vol. 285 (September 1999) 1537-1539.

10. Blaze Photonics/Crystal Fibre A/S, 2007, Product Information, Birkerød, Denmark

11. Fleming, W. "Dispersion in GeO2-SiO2 glasses." *Applied Optics*. Vol. 23, No. 24. (December 1984) 4486-4493.

12. Ghatak, A., Thyagarajan, K. Introduction to Fiber Optics. Cambridge University Press, New York, NY. (1998) 132-150.

13. Gloge, D. "Weakly Guided Fibers." *Applied Optics*. Vol. 10, No. 10 (October 1971) 2252-2258.

14. Grattan, K., Sun, T. "Fiber optic sensor technology: an overview." *Sensors and Actuators*. Vol. 82 (2000) 40-61.

15. Hansen, T., Broeng, J., Jakobsen, C., Vienne, G., Simonsen, H., Nielsen, M., Skovgaard, P., Folkenberg, J., Bjarklev, A., "Air-Guiding Photonic Bandgap Fibers: Spectral Properties, Macrobending Loss, and Practical Handling." *Journal of Lightwave Technology*. Vol. 22 No. 1 (January 2004)

16. Ishigure, T., Nihei, E., Koike, Y. "Optimum refractive-index profile of the graded-index polymer optical fiber, toward gigabit data links." *Applied Optics*. Vol. 35, No. 12 (April 1996) 2048-2053.

17. Jin, J., The Finite Element Method in Electromagnetics, John Wiley & Sons, New York (2002) 288-289.

18. Kersey, A., Berkoff, T., Morey, W., "High-Resolution Fibre-Grating Based Strain Sensor with Interferometric Wavelength-Shift Detection." Electronics Letters. Vol. 28, No. 3 (January 1992)

19. Kim, K., Kollar, L., Springer, G., "Model of Embedded Fiber Optic Fabry-Perot Temperature and Strain Sensors." *Journal of Composite Materials*. Vol. 27, No. 17 (1993) 1618-1662.

20. Koshiba, M., Saitoh, K. "Applicability of classical optical fiber theories to holey fibers." *Optics Letters*. Vol 29., No. 15 (August 2004) 1739-1741.

21. Knight, J., Birks, T., Russell, P., Atkin, D., "All-silica single-mode optical fiber with photonic crystal cladding." *Optics Letters*. Vol. 21, No. 19 (October, 1996) 1547-1550.

22. Kuhlmey, B., McPhedran, R., Martijn, C., "Modal cutoff in microstructured optical fibers." *Optics Letters*, Vol. 27, No. 19 (October 2002) 1684-1687.

23. Kuhlmey, B., White, T., Renversez, G., Maystre, D., Botten, L., Martijn, C., McPhedran, R., "Multipole method for microstructured optical fibers. II. Implementation and results." *Optical Society of America*. Vol. 19, No. 10 (October 2002) 2331-2340.

24. Lawrence, C., Nelson, D., Udd, E. "A Fiber Optic Sensor for Transverse Strain Measurement." *Experimental Mechanics*. Vol. 39, No. 3 (September 1999) 202-209.

25. Legge, T., Swart, P., van Zyl, G., Chtcherbakov, A., "A fibre Bragg grating stress cell for geotechnical engineering applications." *Measurement Science and Technology*. Vol. 17, No. 5 (2006) 1173-1179.

26. Lin, M., Chang, F., "The manufacture of composite structures with a built-in network of piezoceramics." *Composite Science and Technology*. Vol. 62, No. 7-8 (2002) 919-939.

27. Liggins, A., Hardie, W., Finlay , J., "The spatial and pressure resolution fuji pressure-sensitive film." *Experimental Mechanics*, Vol. 35, No. 2, (1995) 166-173.

28. Monroe, T., Richardson, D., Bennett, P., "Developing holey fibers for evanescent field devices." *Electronic Letters.* Vol. 35, No. 14 (July 1999) 1188-1189.

29. Nasilowski, T., Lesiak, P., Kotynshi, R., Antkowiak, M., Fernandez, A., Berghmans, F., Thienpont, H., "Birefringent photonic crystal fiber as a multi-parameter sensor." *Proceedings of the Symposium IEEE/LEOS Benelux Chapter.* (2003) 29-32.

30. Nye, J., Physical Properties of Crystals: Their Representation by Tensors and Matricies. Oxford Science Publications, Oxford UK. (1985) 235-258.

31. Okabe, Y., Yashiro, S., Kosaka, T., Takeda, N., "Detection of transverse cracks in CFRP composites using embedded fiber Bragg grating sensors." *Smart Materials and Structures* Vol. 8, No. 6. (2000) 832-838.

32. Prabhugoud, M., Peters, K., "Finite element model for embedded fiber Bragg grating sensor." *Smart Materials and Structures* Vol. 15 (2006) 550-562.

33. Saitoh, K., Koshiba, M., "Photonic Bandgap Fibers With High Birefringence," *IEEE Photonics Technology Letters*, Vol. 14, No. 9 (2002) .

34. Saitoh, K., Koshiba, M., "Confinement Losses in Air-Guiding Photonic Bandgap Fibers," *IEEE Photonics Technology Letters*, Vol. 15, No. 2 (2003).

35. Silva-Lopez, M., A. Fender, W.N. MacPherson, J.S. Barton, J.D.C. Jones, D. Zhao, D.J. Webb, L Zhang, I. Bennion. "Strain and Temperature Sensitivity of a Singlemode Polymer Optical Fibre." *Optics Letters*. Vol. 30, No. 23. (Dec 2005a) 3129-3131.

36. Tao, X., Tang, L., Du, W., Choy, C., "Internal strain measurement by fiber Bragg grating sensors in textile composites." *Composites Science and Technology.* Vol. 60, No. 5. (2000) 657-669.

37. Thor Labs, 2007, Product Information, Newton, New Jersey

38. Uranus, H., Hoekstra, H., "Modelling of microstructured waveguides using a finite-element-based vectorial mode solver with transparent boundary conditions." *Optics Express*. (June 2004) 2795-2809.

39. White, T., McPhedran, R., Botten, L., Smith, G., Martijn, C., "Calculations of air-guided modes In photonic crystal fibers using the multipole method." *Optics Express.* Vol. 9, No. 13 (2001) 721-732.

40. Yeh, P., Yariv, A., "Theory of Bragg fiber." *Journal of the Optical Society of America*. Vol. 68, No. 9. (September 1978).

41. Zolla, F., Renversez, G., Nicolet, A., Kuhlmey, B., Guenneau, S., Felbacq, D., Foundations of Photonic Crystal Fibres. Imperial College Press, London UK. (2005)

APPENDICIES

Appendix A

TIR Fiber Guided Mode Solution (Matlab Code)

```
% Patrick Van Vickle
% Program to solve for modes in step index fiber - Design parameters
% used are from Comsol reference fiber for verification.
% Code also calculates the theoretical confinement of the fundamental
% mode using equation 8.60 from Ghatak reference.

clear;
clc;

n1=1.4457;          % Index of Core
n2=1.4378;          % Index of Cladding
lambda=1550e-9;     % Free space wavelength
k=(2*pi)/lambda;    % Wave number
a=8E-6;             % Core radius
l=0;                % Mode number (set my looking at V number and p)

V=((2*pi*a)/lambda)*(n1^2-n2^2)^(1/2); % Normalized Frequency

sols_count=1;                       % Initialize counter
beta=n2*k:(n1-n2)*k/1000:n1*k;      % Set beta scan range and resolution


for q=1:size(beta,2)
    p=a*(n1^2*k^2-(beta(q))^2)^(1/2);
    gamma=a*((beta(q))^2-n2^2*k^2)^(1/2);
    lhs(q)=p*besselj(l+1,p)/besselj(l,p);
    rhs(q)=gamma*besselk(l+1,gamma)/besselk(l,gamma);
    sols(q)=lhs(q)-rhs(q);
    if(q>1)
        if((sign(real(sols(q-1))) ~=
sign(real(sols(q))))&(abs(sols(q)<.1)))
            sols_found(sols_count)=(beta(q));
            beta_number(sols_count)=q;
            sols_count=sols_count+1;
        end
    end
end


% Convert to Neff from Beta
for x=1:size(sols_found,2)
    neff(x)=lambda*sols_found(x)/(2*pi);
end


% Start all the plotting
format long;
hold on;

%Plot it all
```

```
for h=1:size(a,2)

%If plotting V is desired
%plot(beta,lhs(h,:),'-',beta,rhs(h,:),'--');

%If plotting neff is desired
plot(beta/k,lhs(h,:)/k,'-',beta/k,rhs(h,:)/k,'--');
axis ([n2 n1 -1E-5 1E-5]);

%If plotting by neff, change if plotting by V
xlabel('Effective Index (neff)');
legend('LHS', 'RHS');
title(['Core Radius: ',num2str(a(1,h)),…
'um   Searching for LP',num2str(l),'X mode(s)']);

%Plot the found solutions
for h=1:size(neff,2)
    plot(neff(h),rhs(1,beta_number(h))/k,'o');
    text(neff(h),rhs(1,beta_number(h))/k+0.2E-5,num2str(neff(h)));
end

%Display data on plot
text(n2+0.0005,0.9E-5,['n1= ',num2str(n1)]);
text(n2+0.0005,0.8E-5,['n2= ',num2str(n2)]);
text(n2+0.0005,0.7E-5,['lambda= ',num2str(lambda)]);
text(n2+0.0005,0.6E-5,['V= ',num2str(V)]);
end

sols_found'  %Output betas to Matlab
neff'        %Output neffs to Matlab
hold off;

%Calculate Power in Core (Ghatak Eq. 8.60)

for h=1:size(neff,2)

    U=a*(k^2*n1^2-sols_found(h)^2)^(1/2);
    W=a*(sols_found(h)^2-k^2*n2^2)^(1/2);

    Pcore=pi*a^2*(1-((besselj(l-1,U)*besselj(l+1,U))/(besselj(l,U))^2));
    Pclad=pi*a^2*(((besselk(l-1,W)*besselk(l+1,W))/(besselk(l,W))^2)-1);
    v(h)=Pclad/(Pcore+Pclad);
end
```

Appendix B

PBG Fiber Guided Mode Solution (Matlab/Comsol Code)

```
% COMSOL Multiphysics Model M-file
% Generated by COMSOL 3.3a (COMSOL 3.3.0.511, $Date: 2007/02/02 19:05:58
$)

flclear fem
fid = fopen('output_power_file.csv','wt');
fid2 = fopen('output_mode_file.csv','wt');

loading=0;
%load_span=[0e8:1e8:5e8];  %Silica
load_span=[0e7:2e7:10e7]; %PMMA
%load_span=[0];
for kk=1:size(load_span,2)

%Loading
loading=load_span(kk);
%Optical Scan Properties
eigs=12;
start_wave=1530e-9;
step_wave=1e-9;
stop_wave=1570e-9;


%Material Properties - Silica
mat_mod_set=73.1e9;
mat_nu_set=0.17;
mat_den_set=2203;
mat_index=1.44462;
mat_p11_set=0.17;
mat_p12_set=0.36;

%Material Properties - PMMA
%mat_mod_set=3.1e9;
%mat_nu_set=0.34;
%mat_den_set=1200;
%mat_index=1.492;
%mat_p11_set=0.3;
%mat_p12_set=0.297;


% COMSOL version
clear vrsn
vrsn.name = 'COMSOL 3.3';
vrsn.ext = 'a';
vrsn.major = 0;
vrsn.build = 511;
vrsn.rcs = '$Name:  $';
vrsn.date = '$Date: 2007/02/02 19:05:58 $';
fem.version = vrsn;
```

```
% Geometry Information Located Here
% Loaded from separate file, not included in looping code presented here


% Constants
fem.const = {'load',loading, ...
  'p11',mat_p11_set, ...
  'p12',mat_p12_set, ...
  'BB1','0.4963', ...
  'BB2','0.6965', ...
  'BB3','0.3223', ...
  'CC1','5.1552E-03', ...
  'CC2','1.3783E-02', ...
  'CC3','8.5322E+01'};

% Initialize mesh
fem.mesh=meshinit(fem, ...
                  'hauto',5);

% (Default values are not included)

% Application mode 1
clear appl
appl.mode.class = 'FlPlaneStrain';
appl.sdim = {'X','Y','Z'};
appl.gporder = 4;
appl.cporder = 2;
appl.assignsuffix = '_pn';
clear prop
prop.frame='ref';
clear weakconstr
weakconstr.value = 'off';
weakconstr.dim = {'lm2','lm3'};
prop.weakconstr = weakconstr;
appl.prop = prop;
clear bnd
bnd.Hy = {0,0,1,0};
bnd.Hx = {0,1,0,0};

%%%%%%%%%%%%%%%%%%%%%%%%%%%%%%%%%%%%%%%%%%%%%%%%
% Pressure Loading Equations
bnd.Fx = {0,0,0,'-load*cos(atan2(Y,X))'};
bnd.Fy = {0,0,0,'-load*sin(atan2(Y,X))'};
%%%%%%%%%%%%%%%%%%%%%%%%%%%%%%%%%%%%%%%%%%%%%%%%

%%%%%%%%%%%%%%%%%%%%%%%%%%%%%%%%%%%%%%%%%%%%%%%%
% Crush Loading Equations
%bnd.Fy = {0,0,0,'-load'};
%%%%%%%%%%%%%%%%%%%%%%%%%%%%%%%%%%%%%%%%%%%%%%%%

bnd.ind = [1,1,2,1,2,2,1,2,3,1,3,1,3,1,3,1,3,1,1,1,1,4,1,1,1,1,1,1,1,1,
...
  1,1,1,1,1,1,1,1,1,1,1,1,1,1,1,1,1,1,1,1,1,1,1,1,1,1,1,1,1,1,1,1,1,1,1,
...
  1,1,1,1,1,1,1,1,1,1,1,1,1,1,1,1,1,1,1,1,1,1,1,1,1,1,1,1,1,1,1,1,1,1,1,
...
```

```
  1,1,1,1,1,1,1,1,1,1,1,1,1,1,1,1,1,1,1,1,1,1,1,1,1,1,1];
appl.bnd = bnd;
clear equ
equ.nu = {0.33,0.34};
equ.E = {2.0e11,'3.1e9[Pa]'};
equ.rho = {7850,'1200[kg/m^3]'};
equ.usage = {0,1};
equ.ind = [1,2,1,1,1,1,1,1,1,1,1,1,1,1,1,1,1,1,1,1,1,1,1,1,1,1,1,1,1,1,
...
  1,1];
appl.equ = equ;
fem.appl{1} = appl;

% Application mode 2
clear appl
appl.mode.class = 'MovingMesh';
appl.sdim = {'Xm','Ym','Zm'};
appl.gporder = 4;
appl.cporder = 2;
appl.assignsuffix = '_ale';
clear prop
prop.allowremesh='on';
prop.origrefframe='ref';
clear weakconstr
weakconstr.value = 'off';
weakconstr.dim = {'lm4','lm5'};
prop.weakconstr = weakconstr;
appl.prop = prop;
clear bnd
bnd.defflag = {{0;0},{1;1},{1;0},{0;1}};
bnd.deform = {{0;0},{'u';'v'},{0;'v'},{'u';0}};
bnd.ind = [3,4,1,3,3,1,3,1,1,4,1,4,1,4,1,4,1,2,2,2,2,1,2,2,2,2,2,2,2,2,
...
  2,2,2,2,2,2,2,2,2,2,2,2,2,2,2,2,2,2,2,2,2,2,2,2,2,2,2,2,2,2,2,2,2,2,2,
...
  2,2,2,2,2,2,2,2,2,2,2,2,2,2,2,2,2,2,2,2,2,2,2,2,2,2,2,2,2,2,2,2,2,2,2,
...
  2,2,2,2,2,2,2,2,2,2,2,2,2,2,2,2,2,2,2,2,2,2,2,2,2,2,2];
appl.bnd = bnd;
clear equ
equ.physexpr = {{0;0},{'u';'v'}};
equ.type = {'free','phys'};
equ.ind = [1,2,1,1,1,1,1,1,1,1,1,1,1,1,1,1,1,1,1,1,1,1,1,1,1,1,1,1,1,1,
...
  1,1];
appl.equ = equ;
fem.appl{2} = appl;

% Application mode 3
clear appl
appl.mode.class = 'PerpendicularWaves';
appl.module = 'RF';
appl.gporder = 4;
appl.cporder = 2;
appl.assignsuffix = '_rfwv';
clear prop
prop.inputvar='lambda';
```

```
appl.prop = prop;
clear bnd
bnd.type = {'E0','H0','cont','IM'};
bnd.ind = [1,2,1,1,3,1,1,1,2,2,2,2,2,2,2,2,3,3,3,3,4,3,3,3,3,3,3,3,3,
...
  3,3,3,3,3,3,3,3,3,3,3,3,3,3,3,3,3,3,3,3,3,3,3,3,3,3,3,3,3,3,3,3,3,3,
...
  3,3,3,3,3,3,3,3,3,3,3,3,3,3,3,3,3,3,3,3,3,3,3,3,3,3,3,3,3,3,3,3,3,3,
...
  3,3,3,3,3,3,3,3,3,3,3,3,3,3,3,3,3,3,3,3,3,3,3,3,3,3,3,3,3,3,3,3,3,3];
appl.bnd = bnd;
clear equ
equ.ntensor = {1,{'n_x';'n_y';1}};
equ.sigma = {0,'1e-14[S/m]'};
equ.epsilonr = {1,2.09};
equ.n = {1,'n_stressed'};
equ.ind = [1,2,1,1,1,1,1,1,1,1,1,1,1,1,1,1,1,1,1,1,1,1,1,1,1,1,1,1,1,
...
  1,1];
appl.equ = equ;
appl.var = {'lambda0','1550e-9', ...
  'nu','1e9'};
fem.appl{3} = appl;
fem.sdim = {{'Xm','Ym'},{'X','Y'},{'x','y'}};
fem.frame = {'mesh','ref','ale'};
fem.border = 1;
clear units;
units.basesystem = 'SI';
fem.units = units;

% Subdomain settings
clear equ
equ.ind = [1,2,1,1,1,1,1,1,1,1,1,1,1,1,1,1,1,1,1,1,1,1,1,1,1,1,1,1,1,
...
  1,1];
equ.dim = {'u','v','x','y','Hx','Hy','hz'};

%%%%%%%%%%%%%%%%%%%%%%%%%%%%%%%%%%%%%%%%%%%%%%%%%%%%%%%%%%%%%%%%%%%%%%%
% Subdomain expressions
% Calculate nx, ny, and the nsilica (geometric effect alone)
%%%%%%%%%%%%%%%%%%%%%%%%%%%%%%%%%%%%%%%%%%%%%%%%%%%%%%%%%%%%%%%%%%%%%%%
equ.expr = {'n_stressed',{'','n_x'}, ...
  'n_x',{'','(1/((1/n_silica)^2+0.5*(p11+p12)*(eX_pn+eY_pn)-0.5*(p11-
p12)*((eX_pn+eY_pn)^2+eXY_pn^2)^0.5))^0.5'}, ...
  'n_y',{'','(1/((1/n_silica)^2+0.5*(p11+p12)*(eX_pn+eY_pn)+0.5*(p11-
p12)*((eX_pn+eY_pn)^2+eXY_pn^2)^0.5))^0.5'}, ...
    'n_silica',{'','(-0.0029*1000000*lambda0_rfwv)+1.496495'}};
fem.equ = equ;

% Library materials
clear lib
lib.mat{1}.name='Silica Glass';
lib.mat{1}.varname='mat1';
lib.mat{1}.variables.nu='0.17';
lib.mat{1}.variables.E='73.1e9[Pa]';
lib.mat{1}.variables.mur='1';
lib.mat{1}.variables.sigma='1e-14[S/m]';
```

```
lib.mat{1}.variables.epsilonr='2.09';
lib.mat{1}.variables.alpha='0.55e-6[1/K]';
lib.mat{1}.variables.C='703[J/(kg*K)]';
lib.mat{1}.variables.n='1.45';
lib.mat{1}.variables.rho='2203[kg/m^3]';
lib.mat{1}.variables.k='1.38[W/(m*K)]';
lib.mat{2}.name='Air, 1 atm';
lib.mat{2}.varname='mat2';
lib.mat{2}.variables.nu0='nu0(T[1/K])[m^2/s]';
lib.mat{2}.variables.eta='eta(T[1/K])[Pa*s]';
lib.mat{2}.variables.C='Cp(T[1/K])[J/(kg*K)]';
lib.mat{2}.variables.rho='rho(p[1/Pa],T[1/K])[kg/m^3]';
lib.mat{2}.variables.k='k(T[1/K])[W/(m*K)]';
lib.mat{2}.variables.cs='cs(T[1/K])[m/s]';
clear fcns
fcns{1}.type='inline';
fcns{1}.name='nu0(T)';
fcns{1}.expr='(-7.887E-12*T^2+4.427E-08*T+5.204E-06)/(1.013e5*28.8e-
3/8.314/T)';
fcns{1}.dexpr={'diff((-7.887E-12*T^2+4.427E-08*T+5.204E-
06)/(1.013e5*28.8e-3/8.314/T),T)'};
fcns{2}.type='inline';
fcns{2}.name='cs(T)';
fcns{2}.expr='sqrt(1.4*287*T)';
fcns{2}.dexpr={'diff(sqrt(1.4*287*T),T)'};
fcns{3}.type='inline';
fcns{3}.name='Cp(T)';
fcns{3}.expr='0.0769*T+1076.9';
fcns{3}.dexpr={'diff(0.0769*T+1076.9,T)'};
fcns{4}.type='inline';
fcns{4}.name='rho(p,T)';
fcns{4}.expr='p*28.8e-3/8.314/T';
fcns{4}.dexpr={'diff(p*28.8e-3/8.314/T,p)','diff(p*28.8e-3/8.314/T,T)'};
fcns{5}.type='inline';
fcns{5}.name='eta(T)';
fcns{5}.expr='-7.887E-12*T^2+4.427E-08*T+5.204E-06';
fcns{5}.dexpr={'diff(-7.887E-12*T^2+4.427E-08*T+5.204E-06,T)'};
fcns{6}.type='inline';
fcns{6}.name='k(T)';
fcns{6}.expr='10^(0.8616*log10(abs(T))-3.7142)';
fcns{6}.dexpr={'diff(10^(0.8616*log10(abs(T))-3.7142),T)'};
lib.mat{2}.functions = fcns;


fem.lib = lib;



% Multiphysics
fem=multiphysics(fem);

% Extend mesh
fem.xmesh=meshextend(fem);

% Solve problem
fem.sol=femstatic(fem, ...
                  'solcomp',{'v','u','y','x'}, ...
```

```
                'outcomp',{'v','u','Y','X','y','x'});

% Save current fem structure for restart purposes
fem0=fem;

% (Default values are not included)

lambda_freespace_span=[start_wave:step_wave:stop_wave];
for iii=1:size(lambda_freespace_span,2)
lambda_freespace_span(iii)
loading

% Application mode 1
clear appl
appl.mode.class = 'FlPlaneStrain';
appl.sdim = {'X','Y','Z'};
appl.gporder = 4;
appl.cporder = 2;
appl.assignsuffix = '_pn';
clear prop
prop.frame='ref';
clear weakconstr
weakconstr.value = 'off';
weakconstr.dim = {'lm2','lm3'};
prop.weakconstr = weakconstr;
appl.prop = prop;
clear bnd
bnd.Hy = {0,0,1,0};
bnd.Hx = {0,1,0,0};
bnd.Fx = {0,0,0,'-load*cos(atan2(Y,X))'};
bnd.Fy = {0,0,0,'-load*sin(atan2(Y,X))'};
bnd.ind = [1,1,2,1,2,2,1,2,3,1,3,1,3,1,3,1,3,1,1,1,1,4,1,1,1,1,1,1,1,1,
...
  1,1,1,1,1,1,1,1,1,1,1,1,1,1,1,1,1,1,1,1,1,1,1,1,1,1,1,1,1,1,1,1,1,1,1,
...
  1,1,1,1,1,1,1,1,1,1,1,1,1,1,1,1,1,1,1,1,1,1,1,1,1,1,1,1,1,1,1,1,1,1,1,
...
  1,1,1,1,1,1,1,1,1,1,1,1,1,1,1,1,1,1,1,1,1,1,1,1,1,1,1,1,1,1,1,1,1,1,1];
appl.bnd = bnd;
clear equ
equ.nu = {0.33,0.16};
equ.E = {2.0e11,'73.1e9[Pa]'};
equ.rho = {7850,'2203[kg/m^3]'};
equ.usage = {0,1};
equ.ind = [1,2,1,1,1,1,1,1,1,1,1,1,1,1,1,1,1,1,1,1,1,1,1,1,1,1,1,1,1,1,1,
...
  1,1];
appl.equ = equ;
fem.appl{1} = appl;

% Application mode 2
clear appl
appl.mode.class = 'MovingMesh';
appl.sdim = {'Xm','Ym','Zm'};
appl.gporder = 4;
appl.cporder = 2;
appl.assignsuffix = '_ale';
```

```
clear prop
prop.allowremesh='on';
prop.origrefframe='ref';
clear weakconstr
weakconstr.value = 'off';
weakconstr.dim = {'lm4','lm5'};
prop.weakconstr = weakconstr;
appl.prop = prop;
clear bnd
bnd.defflag = {{0;0},{1;1},{1;0},{0;1}};
bnd.deform = {{0;0},{'u';'v'},{0;'v'},{'u';0}};
bnd.ind = [3,4,1,3,3,1,3,1,1,4,1,4,1,4,1,4,1,2,2,2,2,1,2,2,2,2,2,2,2,2,
...
  2,2,2,2,2,2,2,2,2,2,2,2,2,2,2,2,2,2,2,2,2,2,2,2,2,2,2,2,2,2,2,2,2,2,2,
...
  2,2,2,2,2,2,2,2,2,2,2,2,2,2,2,2,2,2,2,2,2,2,2,2,2,2,2,2,2,2,2,2,2,2,2,
...
  2,2,2,2,2,2,2,2,2,2,2,2,2,2,2,2,2,2,2,2,2,2,2,2,2,2,2,2,2,2,2,2,2,2,2];
appl.bnd = bnd;
clear equ
equ.physexpr = {{0;0},{'u';'v'}};
equ.type = {'free','phys'};
equ.ind = [1,2,1,1,1,1,1,1,1,1,1,1,1,1,1,1,1,1,1,1,1,1,1,1,1,1,1,1,1,1,1,
...
  1,1];
appl.equ = equ;
fem.appl{2} = appl;

% Application mode 3
clear appl
appl.mode.class = 'PerpendicularWaves';
appl.module = 'RF';
appl.gporder = 4;
appl.cporder = 2;
appl.assignsuffix = '_rfwv';
clear prop
prop.inputvar='lambda';
appl.prop = prop;
clear bnd
bnd.type = {'E0','H0','cont','IM'};
bnd.ind = [1,2,1,1,3,1,1,1,2,2,2,2,2,2,2,2,3,3,3,3,4,3,3,3,3,3,3,3,3,
...
  3,3,3,3,3,3,3,3,3,3,3,3,3,3,3,3,3,3,3,3,3,3,3,3,3,3,3,3,3,3,3,3,3,3,3,
...
  3,3,3,3,3,3,3,3,3,3,3,3,3,3,3,3,3,3,3,3,3,3,3,3,3,3,3,3,3,3,3,3,3,3,3,
...
  3,3,3,3,3,3,3,3,3,3,3,3,3,3,3,3,3,3,3,3,3,3,3,3,3,3,3,3,3,3,3,3,3,3,3];
appl.bnd = bnd;
clear equ
equ.ntensor = {1,{'n_x';'n_y';1}};
equ.sigma = {0,'1e-14[S/m]'};
equ.epsilonr = {1,2.09};
equ.n = {1,'n_stressed'};
equ.ind = [1,2,1,1,1,1,1,1,1,1,1,1,1,1,1,1,1,1,1,1,1,1,1,1,1,1,1,1,1,1,1,
...
  1,1];
appl.equ = equ;
```

```
appl.var = {'lambda0',lambda_freespace_span(iii), ...
  'nu','1e9'};
fem.appl{3} = appl;
fem.sdim = {{'Xm','Ym'},{'X','Y'},{'x','y'}};
fem.frame = {'mesh','ref','ale'};
fem.border = 1;
clear units;
units.basesystem = 'SI';
fem.units = units;

% Subdomain settings
clear equ
equ.ind = [1,2,1,1,1,1,1,1,1,1,1,1,1,1,1,1,1,1,1,1,1,1,1,1,1,1,1,1,1,1,1,
...
  1,1];
equ.dim = {'u','v','x','y','Hx','Hy','hz'};

% Subdomain expressions
equ.expr = {'n_stressed',{'','n_x'}, ...
  'n_x',{'','(1/((1/n_silica)^2+0.5*(p11+p12)*(eX_pn+eY_pn)-0.5*(p11-
p12)*((eX_pn+eY_pn)^2+eXY_pn^2)^0.5))^0.5'}, ...
  'n_y',{'','(1/((1/n_silica)^2+0.5*(p11+p12)*(eX_pn+eY_pn)+0.5*(p11-
p12)*((eX_pn+eY_pn)^2+eXY_pn^2)^0.5))^0.5'}, ...
    'n_silica',{'','(-0.0029*1000000*lambda0_rfwv)+1.496495'}};
fem.equ = equ;

% Library materials
clear lib
lib.mat{1}.name='Silica Glass';
lib.mat{1}.varname='mat1';
lib.mat{1}.variables.nu='0.17';
lib.mat{1}.variables.E='73.1e9[Pa]';
lib.mat{1}.variables.mur='1';
lib.mat{1}.variables.sigma='1e-14[S/m]';
lib.mat{1}.variables.epsilonr='2.09';
lib.mat{1}.variables.alpha='0.55e-6[1/K]';
lib.mat{1}.variables.C='703[J/(kg*K)]';
lib.mat{1}.variables.n='1.45';
lib.mat{1}.variables.rho='2203[kg/m^3]';
lib.mat{1}.variables.k='1.38[W/(m*K)]';
lib.mat{2}.name='Air, 1 atm';
lib.mat{2}.varname='mat2';
lib.mat{2}.variables.nu0='nu0(T[1/K])[m^2/s]';
lib.mat{2}.variables.eta='eta(T[1/K])[Pa*s]';
lib.mat{2}.variables.C='Cp(T[1/K])[J/(kg*K)]';
lib.mat{2}.variables.rho='rho(p[1/Pa],T[1/K])[kg/m^3]';
lib.mat{2}.variables.k='k(T[1/K])[W/(m*K)]';
lib.mat{2}.variables.cs='cs(T[1/K])[m/s]';
clear fcns
fcns{1}.type='inline';
fcns{1}.name='cs(T)';
fcns{1}.expr='sqrt(1.4*287*T)';
fcns{1}.dexpr={'diff(sqrt(1.4*287*T),T)'};
fcns{2}.type='inline';
fcns{2}.name='nu0(T)';
fcns{2}.expr='(-7.887E-12*T^2+4.427E-08*T+5.204E-06)/(1.013e5*28.8e-
3/8.314/T)';
```

```
fcns{2}.dexpr={'diff((-7.887E-12*T^2+4.427E-08*T+5.204E-
06)/(1.013e5*28.8e-3/8.314/T),T)'};
fcns{3}.type='inline';
fcns{3}.name='Cp(T)';
fcns{3}.expr='0.0769*T+1076.9';
fcns{3}.dexpr={'diff(0.0769*T+1076.9,T)'};
fcns{4}.type='inline';
fcns{4}.name='rho(p,T)';
fcns{4}.expr='p*28.8e-3/8.314/T';
fcns{4}.dexpr={'diff(p*28.8e-3/8.314/T,p)','diff(p*28.8e-3/8.314/T,T)'};
fcns{5}.type='inline';
fcns{5}.name='eta(T)';
fcns{5}.expr='-7.887E-12*T^2+4.427E-08*T+5.204E-06';
fcns{5}.dexpr={'diff(-7.887E-12*T^2+4.427E-08*T+5.204E-06,T)'};
fcns{6}.type='inline';
fcns{6}.name='k(T)';
fcns{6}.expr='10^(0.8616*log10(abs(T))-3.7142)';
fcns{6}.dexpr={'diff(10^(0.8616*log10(abs(T))-3.7142),T)'};
lib.mat{2}.functions = fcns;


fem.lib = lib;

% Multiphysics
fem=multiphysics(fem);

% Extend mesh
fem.xmesh=meshextend(fem);

% Solve problem
fem.sol=femeig(fem, ...
               'init',fem0.sol, ...
               'solcomp',{'tHxHy20','tHxHy10','tHxHy21','hz'}, ...

'outcomp',{'tHxHy20','v','tHxHy10','u','tHxHy21','hz','Y','X','y','x'},
...
               'neigs',12, ...
               'shift',0-4.025292e6*i);


fprintf(fid,'%e,',lambda_freespace_span(iii));
  fprintf(fid2,'%e,',lambda_freespace_span(iii));
for jj=1:eigs

%%%%%%%%%%%%%%%%%%%%%%%%%%%%%%%%%%%%%%%%%%%%%%%%%%%%%%%%%%%%
%Calculate Confinement - Subdomain Integration of
% Poynting Vector
%%%%%%%%%%%%%%%%%%%%%%%%%%%%%%%%%%%%%%%%%%%%%%%%%%%%%%%%%%%%

% Integrate - Core
I1(iii,jj)=postint(fem,'Pozav_rfwv', ...
           'unit','W', ...
           'dl',[1], ...
           'solnum',jj);


% Integrate - Entire Geom
```

```
I2(iii,jj)=postint(fem,'Pozav_rfwv', ...
           'unit','W', ...

'dl',[1,2,3,4,5,6,7,8,9,10,11,12,13,14,15,16,17,18,19,20,21,22,23,24,25,26
,27,28,29,30,31,32], ...
           'solnum',jj);

I3(iii,jj)=I1(iii,jj)/I2(iii,jj);



%neff(iii,jj)=fem.sol.lambda(jj);

fprintf(fid,'%e ,',I3(iii,jj));


%%%%%%Output Eigenvalues %%%%%%%%
%imchar = 'i';
fprintf(fid2,'%f + %f%c
,',real(fem.sol.lambda(jj)),imag(fem.sol.lambda(jj)),'i');



end %integration loop
fprintf(fid,'\n');
fprintf(fid2,'\n');

end %wavelength loop
end %load loop

fclose(fid);
fclose(fid2);
```